Spring 1-1-2017

Design of Structures for Wind Vibration Energy Harvesting and Seismic Vibration Mitigation

Gregory C. Conroy
University of Colorado at Boulder, gregcc1012@gmail.com

University of Colorado
Boulder

Design of Structures for Wind Vibration Energy Harvesting and Seismic Vibration Mitigation

Gregory C. Conroy
B.S., The Ohio State University, 2014

A thesis submitted to the
Faculty of the Graduate School of the
University of Colorado in partial fulfillment
of the requirements for the degree of
Master of Science
Department of Civil, Environmental, and Architectural Engineering
2017

This thesis entitled:
Design of Structures for Wind Vibration Energy Harvesting and Seismic Vibration Mitigation
written by Gregory C. Conroy
has been approved for the Department of Civil, Environmental, and Architectural Engineering

_____
Assistant Professor Petros Sideris (Committee Chair)

_____
Professor Ross B. Corotis

_____
Professor Yunping Xi

Date:_____

The final copy of this thesis has been examined by the signatories, and we
find that both the content and the form meet acceptable presentation standards
of scholarly work in the above mentioned discipline

ABSTRACT

Conroy, Gregory C. (M.S., Civil Engineering, Department of Civil Environmental, and Architectural Engineering)

Design of Structures for Wind Vibration Energy Harvesting and Seismic Vibration Mitigation

Thesis Directed by Assistant Professor Petros Sideris

With the changing climate coupled with the limited supply of fossil fuels available for global energy use, much research has been done to develop innovative methods of producing clean and renewable energy. Wind forces can cause tall buildings to undergo significant vibrations that are a potential source of clean and renewable energy for buildings and the power grid. Tall buildings have utilized dampers as a means of mitigating these wind induced vibrations, however, this research proposes the use of dampers as, not only vibration mitigation devices for extreme loading (e.g. strong winds and earthquakes), but also as energy harvesters which convert this vibrational energy into electricity. Designing a building for both energy harvesting (EH) under service conditions (e.g. low or moderate wind loads) and vibration mitigation (VM) under extreme loads is a challenging undertaking due to the conflicting requirements in structural damping for EH and VM. Large damping is required for VM, whereas small or moderate damping is required for EH to ensure that the structure maintains low-amplitude vibrations for as long as possible. Furthermore, the EH potential of buildings using the proposed design solution has never been quantified. In reference to these challenges, the objectives of this research include: (i) development of a nonlinear model for the EH dampers, (ii) quantification of the energy potential of tall buildings subject to wind loading, and (iii) investigation of the seismic performance of tall buildings with damping levels suitable for energy harvesting. The work

described here is a preliminary, yet fundamental, study to assess the feasibility of using dampers to satisfy both objectives described above and will be used as the basis for future research efforts on the topic.

ACKNOWLEDGEMENTS

I would like to thank my advisor, Professor Petros Sideris for his guidance during this research. His background knowledge of structural dynamics was instrumental to studying this unique topic and his enthusiasm, positivity, and encouragement made for a memorable experience.

I also want to express my gratitude to Professor Ross Corotis and Professor Yunping Xi for participating on my M.S. thesis committee and taking the time to review my thesis.

TABLE OF CONTENTS

LIST OF TABLES

LIST OF FIGURES

1. INTRODUCTION

1.1. Motivation

With the changing climate coupled with the limited supply of fossil fuels available for global energy use, much research has been done to develop innovative methods for producing clean and renewable energy. One potential source of renewable energy that has begun to receive attention in recent years is vibrational energy. Zou and Tang (2013) presented several sources of vibration that provide potential harvestable energy. These sources include regenerative vehicle suspensions, railway tracks, human motion, ocean waves, and wind induced vibrations of buildings, which are the topic of this study.

As shown in Figure 1.1, tall buildings are of equal or greater height than wind turbines that are used today to generate electricity at rates ranging from 100 to 1,500 kW. This comparison illustrates the magnitude of wind forces acting on tall buildings. Under high winds, these forces can cause significant deformations which can result in occupant discomfort if the accelerations exceed levels perceptible to humans. Because of the high flexibility and natural periods of tall buildings, the design of lateral force resisting systems for these structures is often controlled by wind loading, as opposed to seismic loading which often controls for shorter buildings with lower natural periods.

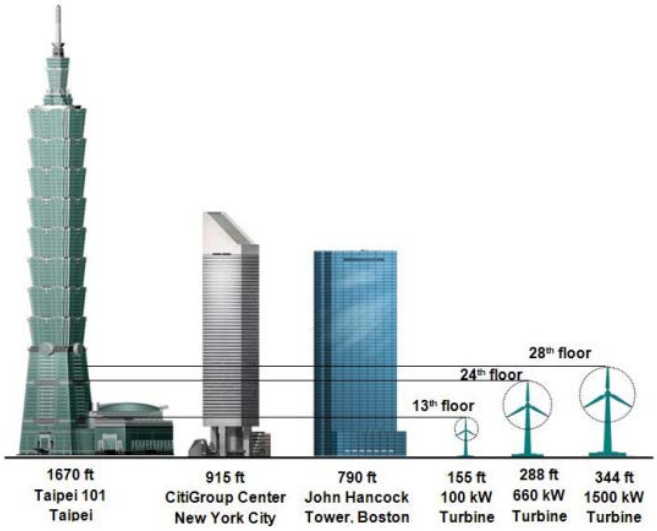

Figure 1.1 Comparison of civil structures with wind turbines (Ni, Zuo, & Kareem, 2011)

Considering the fact that the number of tall buildings throughout the world is rapidly increasing, the need for economic methods of mitigating these undesirable building motions is becoming increasingly important. One method that has been shown to effectively mitigate the effects of wind forces (as well as seismic forces) is the use of supplemental damping systems. Because tall buildings are large consumers of energy and this energy makes up a large portion of building operating costs, it would be of significant benefit to both the environment and building owners if these supplemental damping systems could convert, instead of dissipating, the input energy into electrical energy to be used by the building occupants, thus achieving the goals of both energy harvesting (EH) and vibration mitigation (VM).

1.2. Background

1.2.1. Energy Harvesting Devices

The energy associated with mechanical vibrations can be converted to electrical energy through the use of transducers, of which there are two popular types that have been the topic of numerous studies: *piezoelectric* and *electromagnetic* transducers. These two types of transducers

harvest energy in fundamentally different ways and are, thus, suitable for different applications. Piezoelectric transducers generate electricity from an applied force or stress and are suitable for situations of high force and small deformations/displacements (Zuo & Tang, 2013). Transducers of this type were installed in the floor of Tokyo Station to harvest the vibrational energy of passengers exiting the station as shown in Figure 1.2. Piezoelectric transducers have also been used to harvest the traffic induced vibration of bridges (Baldwin, Roswurm, Nolan, & Holliday, 2011; Peigney & Siegert, 2013). Both of these applications resulted in small scale electrical power output (less than 1 W), and, in the case of the Tokyo Station, the piezoelectric materials showed signs of degradation and reduced power output after just a few weeks of use, raising concerns regarding the durability and long-term performance of this type of transducer.

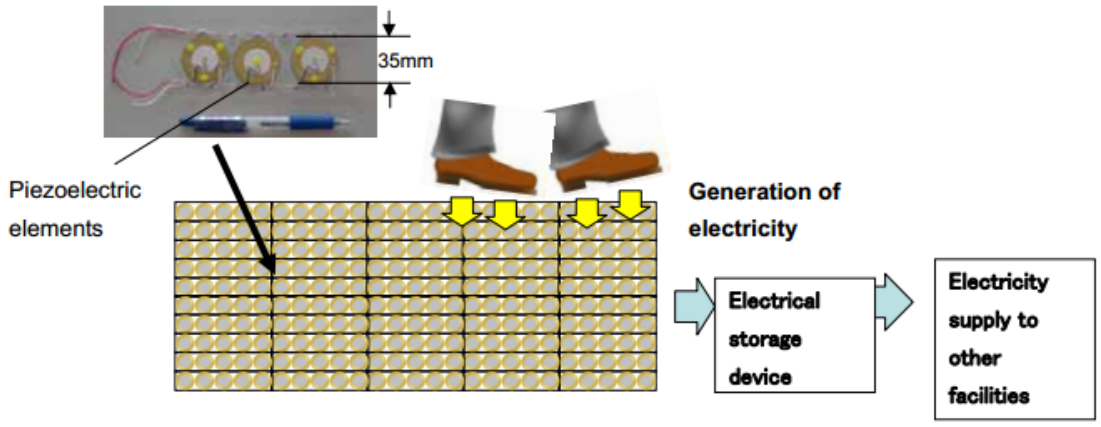

Figure 1.2 Piezoelectric energy harvesting stacks used in Tokyo Station (East Japan Railway Company, 2008)

Electromagnetic (EM) transducers are better suited for applications involving vibrations of large amplitude and show a greater potential for use in large scale energy harvesting (Zuo & Tang, 2013). Several types and configurations of EM transducers have been proposed, including linear moving magnet transducers, as shown in Figure 1.3 (Palomera-Arias, 2005; Zhu, Shen, & Xu, 2012), and transducers with linear-to-rotational motion conversion, where the motion

conversion is achieved through the use of a ballscrew mechanism (Cassidy, Scruggs, Behrens, & Gavin, 2011; Kawamoto, Suda, Inoue, & Kondo, 2008). For transducers that utilize linear-to-rotational motion conversion, the ballscrew can be mounted to the EM motor, either directly, as shown in Figure 1.4 and studied for use in vehicle suspension systems, or in tandem with the use of a timing belt, as shown in Figure 1.5.

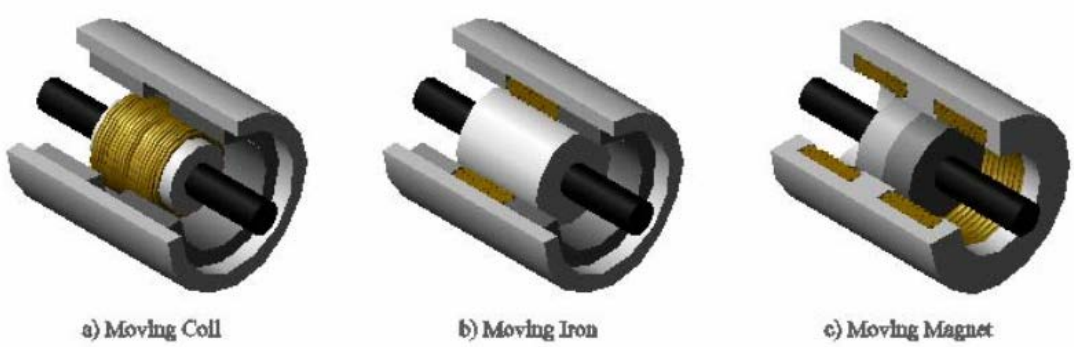

Figure 1.3 Linear moving magnet transducer configurations (Palomera-Arias, 2005)

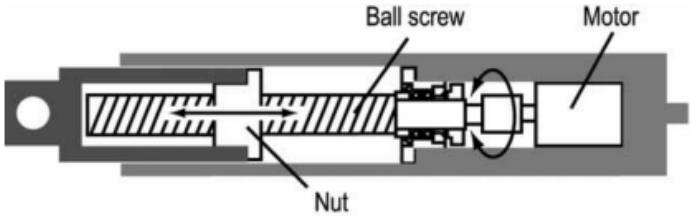

Figure 1.4 EM transducer with linear-to-rotational motion and directing interfacing with EM motor (Kawamoto et al. 2008)

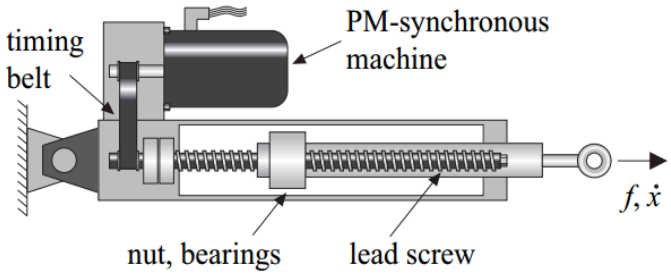

Figure 1.5 EM transducer with linear-to-rotational motion and tandem interfacing with EM motor (Cassidy et al. 2011)

1.2.2. Passive Supplemental Damping Devices

Passive supplemental damping as a method of mitigating wind and earthquake induced vibrations has been extensively studied in recent decades. Several types of damping devices have been investigated, including *viscous* (or velocity-sensitive) devices, such as viscous fluid dampers (Constantinou & Symans, 1992; McNamara & Taylor, 2003) and viscoelastic dampers (Mazza & Vulcano, 2010; Zhang & Soong, 1992), and *hysteretic* (or displacement-sensitive) devices, such as friction dampers (Ciampi, De Angelis, & Paolacci, 1995; Filiatrault & Cherry, 1987) and buckling-restrained braces (Black, Makris, & Aiken, 2004; Sabelli & Lopez, 2004). As an alternative to viscous or hysteretic damping devices, tuned mass dampers (TMDs) have been used as VM systems (Hrovat, Barak, & Rabins, 1983; Sladek & Klingner, 1983). TMDs are mass-spring-dashpot systems designed to divert energy from the structure to the TMD, where the energy is dissipated. TMDs are usually installed at the roof level of high-rise buildings and are calibrated to a specific modal frequency. These devices have proven to be effective in mitigating the wind induced vibrations of tall buildings (Christopoulos & Filiatrault, 2006). The analysis and design principles of viscous and hysteretic damping devices as well as TMDs are discussed in detail in Christopoulos and Filiatrault (2006).

1.2.3. Damping Systems for Energy Harvesting and Vibration Mitigation

Traditionally, the energy dissipated by passive damping devices is converted to heat energy. However, there has been a recent interest in combining the concepts of EH and VM by converting this dissipated energy into electricity. For example, Ni et all (2011) studied the use of TMDs as a way of generating electricity by replacing the dashpot within the TMD with an EH damper. This study concluded that the TMD was capable of dissipating energy at a rate of about 90 kW for reference winds speeds of 13.55 m/s at a reference height of 10 meters, which could

potentially be used to support building energy needs. However, TMDs are not an effective method of VM during seismic events mainly because they are tuned to a single mode of vibration, usually the first mode, which, for tall buildings, may not be a significant mode of vibration during an earthquake. Furthermore, if the building is damaged during a seismic event, the stiffness and natural period will be altered causing the TMD to become mistuned. Other disadvantages of TMDs are their large mass, large space required for installation, and the need to be mounted on smooth surfaces to minimize friction and facilitate free motion (Christopoulos & Filiatrault, 2006).

The EM transducers previously discussed are velocity-sensitive, and, thus, in addition to their use as energy harvesters, they respond as viscous damping elements and can be used as VM devices. One critical advantage of viscous and viscoelastic damping devices over TMDs is that they are capable of dissipating energy in several modes of vibration as opposed to just one. Palomera-Arias (2005) investigated the use of a tubular linear moving magnet EM transducer as a damping device. This study found that the technology, at the time, required a larger and more costly linear moving magnet EM damper as compared to a traditional fluid viscous damper for a given level of damping. However, this study did illustrate the flexibility of EM dampers in achieving a range of damping coefficients which could be used as part of a semi-active or active damping system. The use of the EM damper as an energy harvester was not investigated, which could make the use of this type of damper more attractive as the harvested energy could reduce building operating costs. Zhu et al. (2011) presented a method of modeling a linear moving magnet EM damper as an energy harvester; however, its use in large scale civil structures was not investigated.

Velocity-sensitive devices are usually installed between floors and motion magnification schemes, as shown in Figure 1.6 and Figure 1.7, can be used to enhance their energy dissipating characteristics. The geometry of the bracing systems shown in these figures magnifies the extension of the damper arm, which also magnifies the reaction force and energy dissipated by the damper. These advantages imply that EM devices can be used as damping elements in structures which can theoretically achieve the goals of both EH under moderate wind loading and VM under extreme loading such as strong winds or earthquakes.

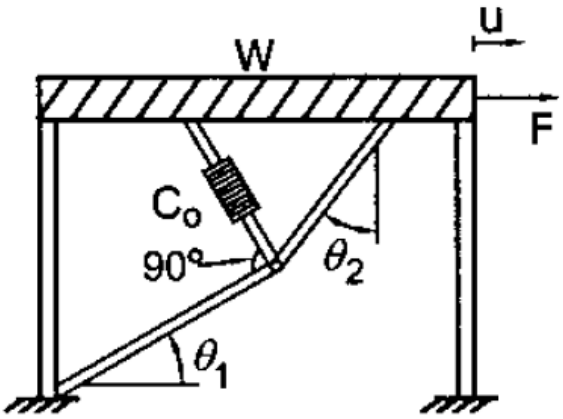

Figure 1.6 Upper toggle brace for motion magnification (Constantinou, Tsopelas, Hammel, & Sigaher, 2001)

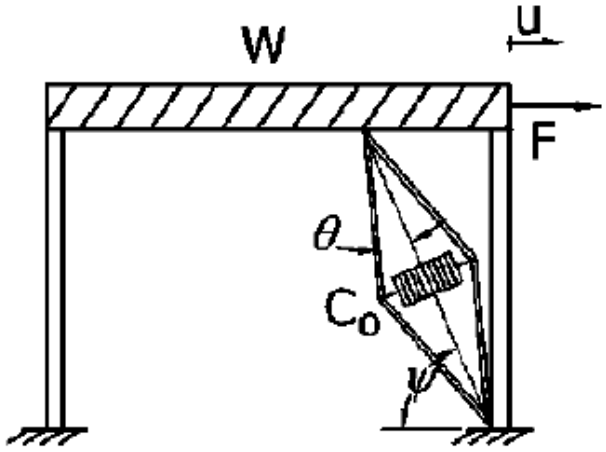

Figure 1.7 Scissor jack bracing for motion magnification (Sigaher & Constantinou, 2003)

1.3. Research Objectives

The topic of this thesis is to assess the feasibility of using EM transducers as EH dampers in tall buildings to achieve the goals of both EH under wind induced vibrations and VM under extreme winds and high seismic events. For the remainder of this study, these devices will be referred to as *EH dampers*. Included in this study will be an investigation on the damping ratio provided by the EH damper that optimizes both EH and if this damping ratio is suitable for VM. From an EH perspective, the goal is to maximize energy dissipated/harvested by the EH damper; however, considering that energy is the integral of force over the displacement path, increasing the damping provided by the EH damper does not necessarily increase the rate of the harvested/dissipated energy. This is because system displacements/velocities decrease with the increased damping. In other words, the supplemental damping (by the EH damper) selected to maximize the harvested energy may not be sufficiently large to mitigate the seismic response of the structure, preventing yielding or damage. Moreover, different supplemental damping ratios may maximize energy harvesting under different wind speeds, which tend to generate forces of different frequency content. Along with investigating the feasibility of this concept, another goal of this research is to determine the relationship between these two objectives for a given system and loading condition.

A general outline of this thesis is as follows. Following this first chapter, Chapter 2 investigates a single-degree-of-freedom (SDF) system equipped with an EH damper and derives an expression to predict the supplemental damping ratio provided by the EH damper that maximizes the rate of the harvested energy. The relationship of this optimal damping ratio and the damping ratio required for VM is also discussed. Chapter 3 describes the EH damper that will be used in this study and develops a numerical model to describe its response under applied

displacement time histories. Mathematical models for the wind loads acting on tall buildings are investigated in Chapter 4, and in Chapter 5, these wind loads are applied to a 76 story shear building. Chapter 5 further investigates the effectiveness of the EH dampers, calibrated to maximize EH, in controlling displacements and inter-story drifts during seismic events. The thesis is concluded with a discussion on the major findings of this study and recommendations for future research directions.

2. ENERGY HARVESTING OF A SINGLE DEGREE OF FREEDOM SYSTEM

2.1. Introduction and Objectives

Before the EH potential of large civil structures can be investigated, it us helpful to understand how the use EH dampers affect the behavior of simple systems. This chapter investigates the use of an electromagnetic (EM) EH damper in a single degree of freedom (SDF) system under harmonic loading. An analytical solution for the damping ratio provided by the EH damper that maximizes the rate of energy harvesting for a given system is developed. Validation of this analytical solution is done by comparison to numerical solutions. This chapter also discusses the relationship between the damping required to optimize EH and the damping required for VM.

2.2. Derivation of Optimal EM Damping Ratio and EM Power

Consider an SDF system equipped with an energy EH damper as shown below in Figure 2.1.

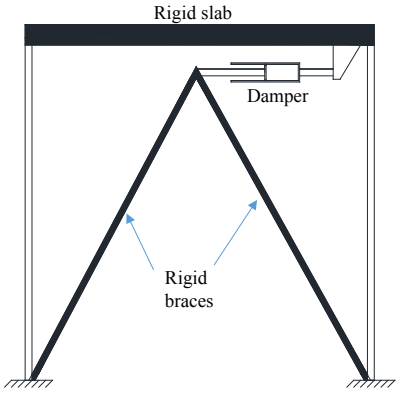

Figure 2.1 SDF system equipped with EH damper

The system is subject to harmonic loading, *p(t)*, defined as:

$$p(t) = p_0 \sin(\omega t) \tag{2-1}$$

where p_o is the magnitude of the force and ω is the forcing frequency. Assuming the EH damper can be idealized as a linear viscous damper, the equation of motion governing the response of the system is:

$$m\ddot{u}(t) + c_s\dot{u}(t) + c_{EM}\dot{u}(t) + ku(t) = p_0 \sin(\omega t) \tag{2-2}$$

where *u(t)* is the displacement of the system, *m* and *k* are the mass and stiffness of the system, and c_s and c_{EM} are the damping coefficients provided by the structure and the EH damper, respectively. The subscript "$_{EM}$" represents quantities associated with the electromagnetic (EM) force provided by the EH damper. The energy dissipated by the EH damper during the steady-state response is:

$$E_{d,EM} = \int c_{EM}\dot{u}(t)du = c_{EM}\int \dot{u}(t)^2 dt \tag{2-3}$$

where $E_{d,EM}$ is the energy dissipated/harvested by the EH damper in the form of EM energy. The duration of a single cycle of the steady-state response, is equal to the forcing period:

$$T = \frac{2\pi}{\omega} \tag{2-4}$$

and the energy dissipated by the EH damper during one cycle is

$$E_{d,EM} = c_{EM}\int_0^{2\pi/\omega} \dot{u}(t)^2 dt \tag{2-5}$$

The steady-state response of the system, *u(t)*, due to the harmonic loading is:

$$u(t) = u_0 \sin(\omega t - \phi) \tag{2-6}$$

and the corresponding steady-state velocity is given as:

$$\dot{u}(t) = u_0\omega \cos(\omega t - \phi) \tag{2-7}$$

where u_o is the amplitude of the steady response of the system and ϕ is the phase angle associated with the system and loading properties (Chopra, 2013). Thus, the energy dissipated by the EH damper in a single cycle is

$$E_{d,EM} = c_{EM}\int_0^{\frac{2\pi}{\omega}}\left[u_0\omega\cos(\omega t-\phi\right]^2 dt = c_{EM}\left(u_0\omega\right)^2\int_0^{\frac{2\pi}{\omega}}\cos^2(\omega t-\phi)dt \tag{2-8}$$

The integral in Eq. (2-8) can be proven to be equal to π/ω, which yields:

$$E_{d,EM} = \pi c_{EM}u_0^2\omega \tag{2-9}$$

Since we are assuming the damping of the EH damper can be modeled as linear viscous damping, the EM damping coefficient is equal to

$$c_{EM} = 2\zeta_{EM}m\omega_n \tag{2-10}$$

where ζ_{EM} is the equivalent EM damping ratio provided by EH damper and ω_n is the natural circular frequency equal to:

$$\omega_n = \sqrt{k/m} \tag{2-11}$$

Substituting Eqs. (2-10) and (2-11) into Eq. (2-9) gives:

$$E_{d,EM} = 2\pi\zeta_{EM}\frac{\omega}{\omega_n}ku_0^2 \tag{2-12}$$

Following a similar process, the energy dissipated by the structure in a single cycle of the steady-state response is

$$E_{d,s} = 2\pi\zeta_s\frac{\omega}{\omega_n}ku_0^2 \tag{2-13}$$

where ζ_s is the damping ratio provided by the structure. The total energy dissipated within the system is the sum of the two expressions above:

$$E_d = E_{d,s} + E_{d,EM} = 2\pi(\zeta_s + \zeta_{EM})\frac{\omega}{\omega_n}ku_0^2 = 2\pi\zeta_t\frac{\omega}{\omega_n}ku_0^2 \tag{2-14}$$

where ζ_t is the total damping ratio of the system equal to the sum of the structural and EM damping ratios. Eq. (2-14) is consistent with the expression for energy dissipated by a system that is not equipped with an EH damper, in which case $\zeta_{EM} = 0$ and $\zeta_t = \zeta_s$. It should also be noted that the Eq. (2-14) could have also been derived if the damping forces in the equation of motion were replaced by a single damping force, F_d equal to

$$F_d = F_{d,s} + F_{d,EM} = (c_s + c_{EM})\dot{u}(t) = c_t\dot{u}(t) \tag{2-15}$$

where $F_{d,s}$ and $F_{d,EM}$ are the structural and EM damping forces, respectively, and c_t is the total damping coefficient of the system equal to the sum of the structural and EM damping coefficients.

In Eqs. (2-12) and (2-13), the response of the system is accounted for by the amplitude of the steady-state response, u_o, given as:

$$u_0 = u_{st}R_d \tag{2-16}$$

where the equivalent static deformation, u_{st}, is defined as:

$$u_{st} = \frac{p_0}{k} \tag{2-17}$$

and the deformation response factor, R_d, which accounts for the dynamic response of the structure, is given as:

$$R_d \frac{1}{\sqrt{\left[1-\left(\frac{\omega}{\omega_n}\right)^2\right]^2 + \left[2\zeta\left(\frac{\omega}{\omega_n}\right)\right]^2}} \tag{2-18}$$

In the case of a system equipped with an EH damper, the response of the system is dependent on the total damping of the system. Therefore, the damping ratio, ζ, in Eq. (2-18) should be the sum of the damping ratios provided by the structure and the EH damper, ζ_t. Substituting Eqs. (2-17) and (2-18) into Eq. (2-16) and then substituting the resulting expression for u_o into Eq. (2-12) and Eq. (2-13), the following expressions are obtained for the energy dissipated per cycle, during the steady-state response, due to the EH damper and the inherent structural damping, respectively:

$$E_{d,EM} = 2\pi\zeta_{EM}\left(\frac{\omega}{\omega_n}\right)\frac{p_0^2}{k}\left(\left[1-\left(\frac{\omega}{\omega_n}\right)^2\right]^2+\left[2\zeta\left(\frac{\omega}{\omega_n}\right)\right]^2\right)^{-1} \tag{2-19}$$

and

$$E_{d,s} = 2\pi\zeta_{s}\left(\frac{\omega}{\omega_n}\right)\frac{p_0^2}{k}\left(\left[1-\left(\frac{\omega}{\omega_n}\right)^2\right]^2+\left[2\zeta\left(\frac{\omega}{\omega_n}\right)\right]^2\right)^{-1} \tag{2-20}$$

When investigating the feasibility of installing an EH damper in a structure, it is critical to estimate the rate at which energy is harvested, i.e. the power generated by the EH damper. In general the EM power, P_{EM}, is defined as:

$$P_{EM} = \frac{dE_{d,EM}}{dt} \tag{2-21}$$

For the EM power generated during one cycle of the steady-state response under harmonic loading, we can simplify this by dividing $E_{d,EM}$ by the duration of a single cycle to determine the average power during steady-state response:

$$P_{EM} = \frac{E_{d,EM}}{2\pi/\omega} = \zeta_{EM}\left(\frac{\omega^2}{\omega_n}\right)\frac{p_0^2}{k}\left(\left[1-\left(\frac{\omega}{\omega_n}\right)^2\right]^2 + \left[2\zeta_t\left(\frac{\omega}{\omega_n}\right)\right]^2\right)^{-1} \tag{2-22}$$

To find the damping ratio that maximizes P_{EM}, we first substitute $\zeta_t = \zeta_s + \zeta_{EM}$ into Eq. (2-22) and set its derivative with respect to the EM damping ratio, ζ_{EM}, to zero. This derivative is obtained as:

$$\frac{dP_{EM}}{d\zeta_{EM}} = \frac{\frac{\omega^2 p_0^2}{\omega_n k}}{\left[1-\left(\frac{\omega}{\omega_n}\right)^2\right]^2 + \left[2(\zeta_s+\zeta_{EM})\left(\frac{\omega}{\omega_n}\right)\right]^2} - \frac{8\zeta_{EM}(\zeta_s+\zeta_{EM})\frac{\omega^2 p_0^2}{\omega_n k}\left(\frac{\omega}{\omega_n}\right)^2}{\left(\left[1-\left(\frac{\omega}{\omega_n}\right)^2\right]^2 + \left[2(\zeta_s+\zeta_{EM})\left(\frac{\omega}{\omega_n}\right)\right]^2\right)^2} \tag{2-23}$$

Setting Eq. (2-23) equal to zero, an expression for the value of ζ_{EH} that maximizes P_{EM} is obtained. The corresponding calculations are presented below:

$$0 = 1 - \frac{8\zeta_{EM}(\zeta_s+\zeta_{EM})\left(\frac{\omega}{\omega_n}\right)^2}{\left(\left[1-\left(\frac{\omega}{\omega_n}\right)^2\right]^2 + \left[2(\zeta_s+\zeta_{EM})\left(\frac{\omega}{\omega_n}\right)\right]^2\right)} \tag{2-24}$$

Eq. (2-24) can then be rewritten in the form of a quadratic equation and solved using the quadratic formula.

$$0 = -4\left(\frac{\omega}{\omega_n}\right)^2\zeta_{EM}^2 + \left[1-\left(\frac{\omega}{\omega_n}\right)^2\right]^2 + 4\left(\frac{\omega}{\omega_n}\right)^2\zeta_s^2 \tag{2-25}$$

$$\zeta_{EM} = \pm\frac{4\left(\frac{\omega}{\omega_n}\right)\sqrt{\left[1-\left(\frac{\omega}{\omega_n}\right)^2\right]^2 + 4\left(\frac{\omega}{\omega_n}\right)^2\zeta_s^2}}{-8\left(\frac{\omega}{\omega_n}\right)^2} \tag{2-26}$$

Ignoring the negative values in the Eq. (2-26), the optimum damping ratio, ζ^*_{EM}, is

$$\zeta^*_{EM} = \frac{\sqrt{\left[1-\left(\frac{\omega}{\omega_n}\right)^2\right]^2 + 4\left(\frac{\omega}{\omega_n}\right)^2 \zeta_s^2}}{2\left(\frac{\omega}{\omega_n}\right)} \tag{2-27}$$

Validation of Eqs. (2-22) and (2-27) is included in the next section.

The optimum EM damping ratio versus the forcing frequency ratio (defined as the ratio of forcing frequency to natural frequency) is plotted in Figure 2.2 for several values of the structural damping ratio, ζ_s. Figure 2.3 and Figure 2.4 show EM Power (from Eq. (2-22)) vs ζ_{EM} for several forcing frequency ratios and structural damping ratios of 1% and 5%, respectively. The SDF system shown in these figures has a natural period, T_n, equal to 1 second and a mass of 250 kg. The magnitude of the harmonic loading, p_o, was 100 N. Table 2.1 summarizes the optimum damping ratios for Figure 2.3 and Figure 2.4 calculated from Eq. (2-27) and the associated EM powers from Eq. (2-22).

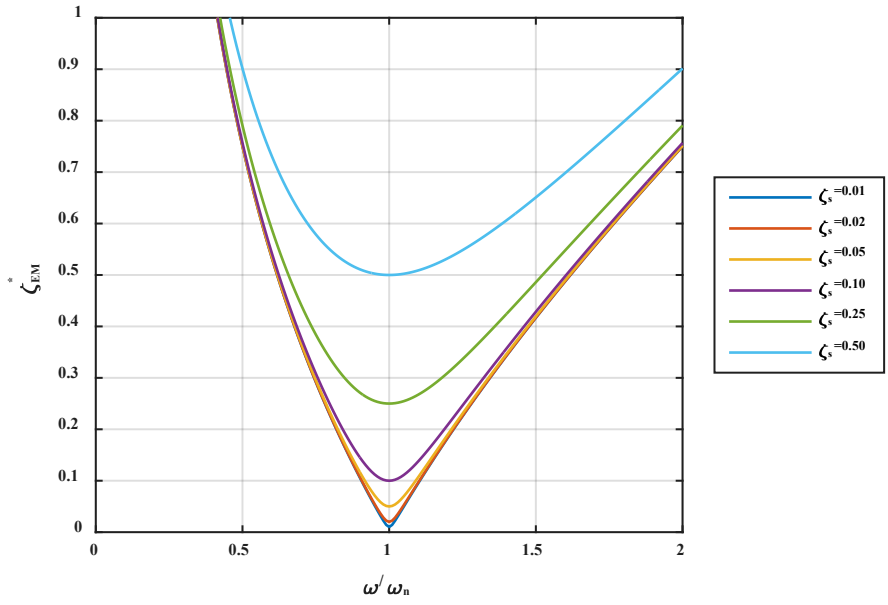

Figure 2.2 Optimum energy harvesting (EH) damping ratios

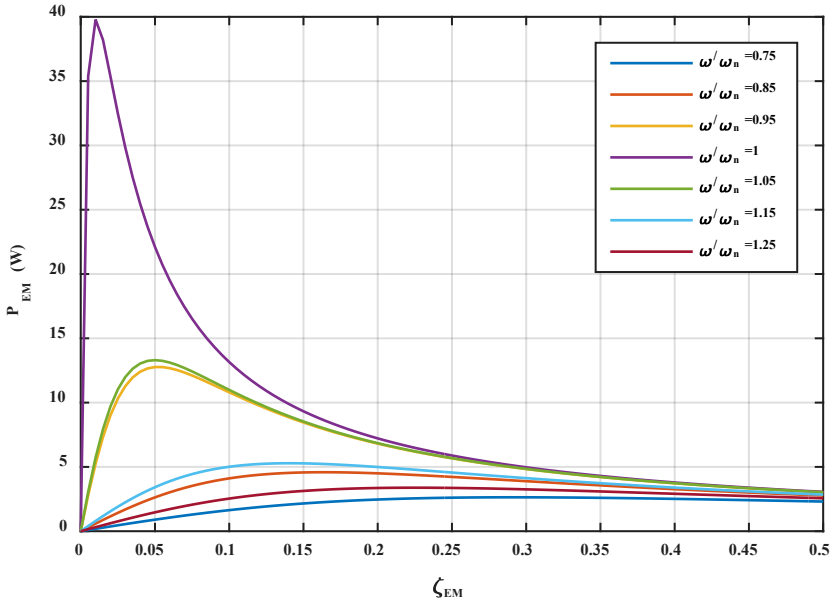

Figure 2.3 EM Power versus ζ_{EM} for various values of ω/ω_n and ζ_s = 1%

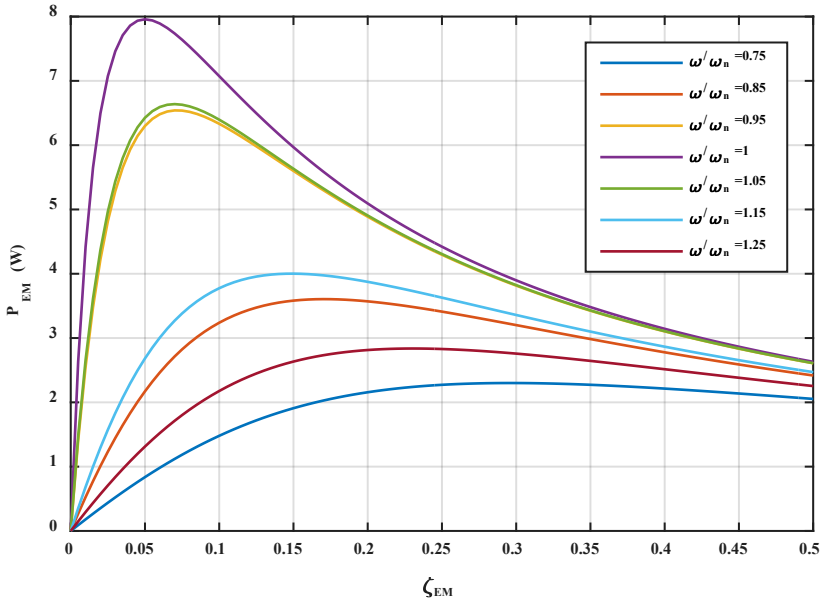

Figure 2.4 EM Power versus ζ_{EM} for various values of ω/ω_n and ζ_s = 5%

Table 2.1. Optimum EM damping ratios and EM power for example system

	ζ_s = 1%		ζ_s = 5%	
ω/ω_n	ζ^*_{EM}	P_{EM} (W)	ζ^*_{EM}	P_{EM} (W)
0.75	29.2%	2.64	29.6%	2.30
0.85	16.4%	4.59	17.1%	3.61
0.95	5.2%	12.78	7.2%	6.54
1.00	1.0%	39.79	5.0%	7.96
1.05	5.0%	13.30	7.0%	6.64
1.15	14.1%	5.29	14.9%	4.00
1.25	22.5%	3.38	23.1%	2.84

Figure 2.3, Figure 2.4, and Table 2.1 show that as the forcing frequency ratio approaches a value of 1, the EM damping ratio that maximizes EM power decreases, which is in agreement with Eq. (2-27) and Figure 2.2. In fact from Eq. (2-27) it can be proven that at resonance (ω/ω_n = 1) the EM damping ratio that maximizes EM power is equal to the damping of the structure, ζ_s. This is also shown in Figure 2.3, Figure 2.4, and Table 2.1. Conversely, as the forcing frequency ratio diverges from the resonant forcing frequency, the optimal damping ratio increases without bound. It is also interesting to note that for low EM damping ratios, the damping inherent in the structure has a significant impact on the maximum EM power that can be achieved, whereas for high EM damping ratios, the structural damping has little effect on the maximum EM power.

2.3. Validation of the Analytical Solution

To validate Eqs. (2-22) and (2-27), the equation of motion given in Eq. (2-2) was solved using numerical integration techniques by converting it to state-space form. The lengths of each of the analyses were chosen to ensure the steady-state response was reached. The EM power was then estimated by the slope of a linear line of best fit through last five cycles of the steady-state response of the EM energy time histories. Figure 2.5 and Figure 2.6 show the numerical estimation of the EM power compared with the analytical solution from Eq. (2-22) for structural damping ratios 1% and 5%, respectively, and for forcing frequency ratios of 0.75, 1.00, and 1.25.

The circles represent the numerical data points and the solid lines represent the analytical solution. The numerical and analytical solutions are in agreement and the EM damping ratios that maximize power for the numerical solution coincide with those for the analytical solution presented in the previous section.

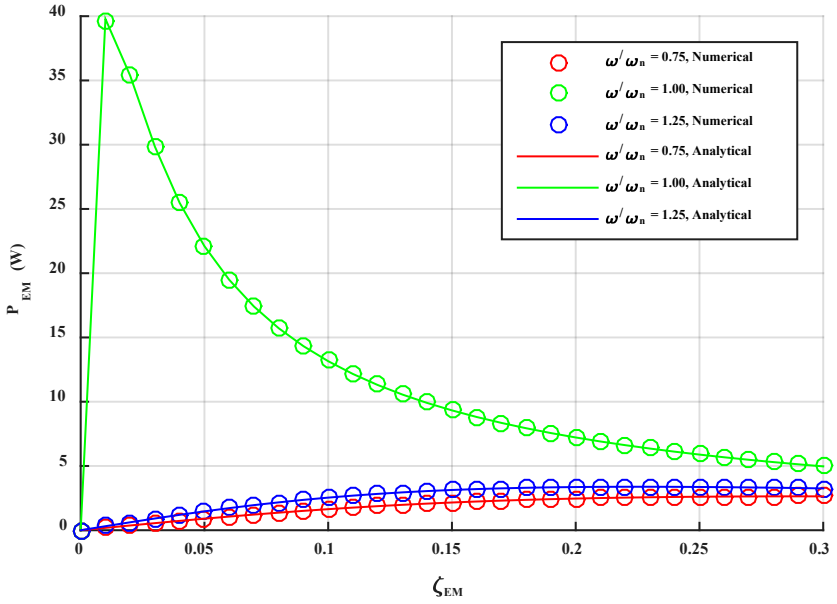

Figure 2.5 Validation of Eqs. (2-22) and (2-27) with ζ_s = 1%

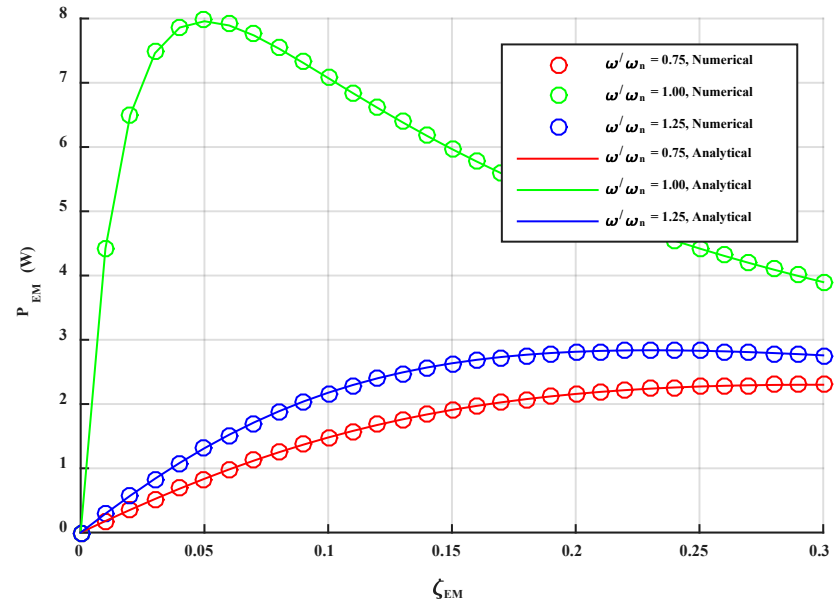

Figure 2.6 Validation of Eqs. (2-22) and (2-27) with ζ_s = 5%

2.4. Effect of EM Damping on Vibration Control

Because supplemental damping systems are traditionally used as a means of vibration control, the ability of the EH damper in reducing structural displacements is also of interest to this study. Figure 2.7 and Figure 2.8 shows the peak displacements during the steady response of harmonic loading given by Eq. (2-16) for the same system shown in Figure 2.3 and Figure 2.4. Low values of the EM damping ratio result in high displacements, especially when paired with low levels of structural damping. The peak displacements also increase as the forcing frequency ratio approaches unity (i.e. resonance).

However, a comparison Figure 2.3 and Figure 2.4 with Figure 2.7 and Figure 2.8 shows that the pairs of EM damping ratios and forcing frequency ratios that maximize EM power result in large displacements. That implies that large damping ratios would be required to reduce the peak displacements, which would also reduce the EM power. This illustrates the competing goals between EH and VM in terms of the selected damping ratio. In fact, for forcing frequencies close to the natural frequency of the structure, low EM damping is required to maximize EM power, however, high damping is required limit displacements and potential damage to the structure. By differentiating Eq. (2-6) twice, it can be shown that the peak acceleration during the steady response is equal to the peak displacement multiplied by the square of the forcing frequency as shown below:

$$\ddot{u}(t) = -u_0\omega^2 \sin(\omega t - \phi) \tag{2-28}$$

where u_0 is given from Eq. (2-16). In other words, the peak acceleration vs. EM damping ratio curves would look similar to Figure 2.7 and Figure 2.8, except scaled by ω^2. Therefore, because building accelerations are a measure of occupant discomfort, low damping paired with the resonant response may also lead to serviceability concerns. Since the primary objective in any

structural system is to serve its intended purpose while providing for the safety and comfort of its occupants, the EM damping ratio that maximizes EM power may not be a practical design solution.

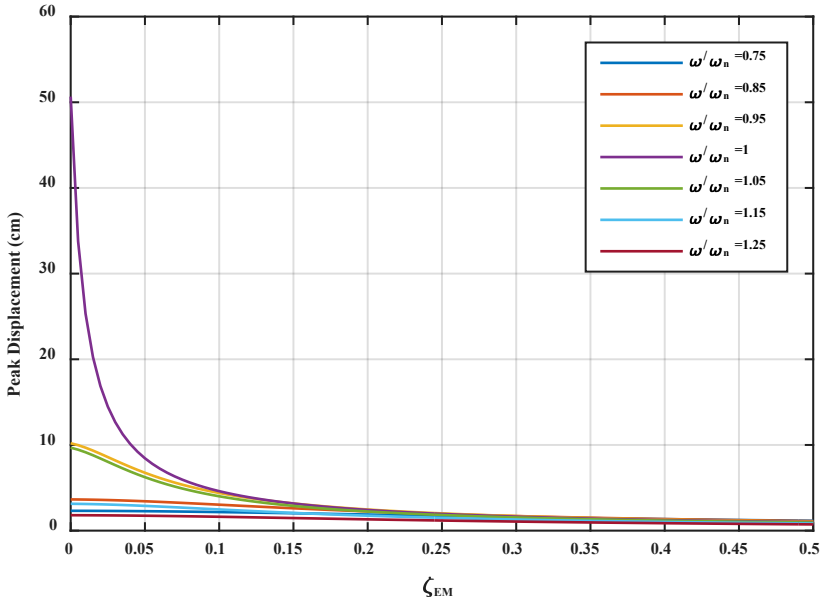

Figure 2.7 Peak displacement versus ζ_{EM} for various values of ω/ω_n and ζ_s = 1%

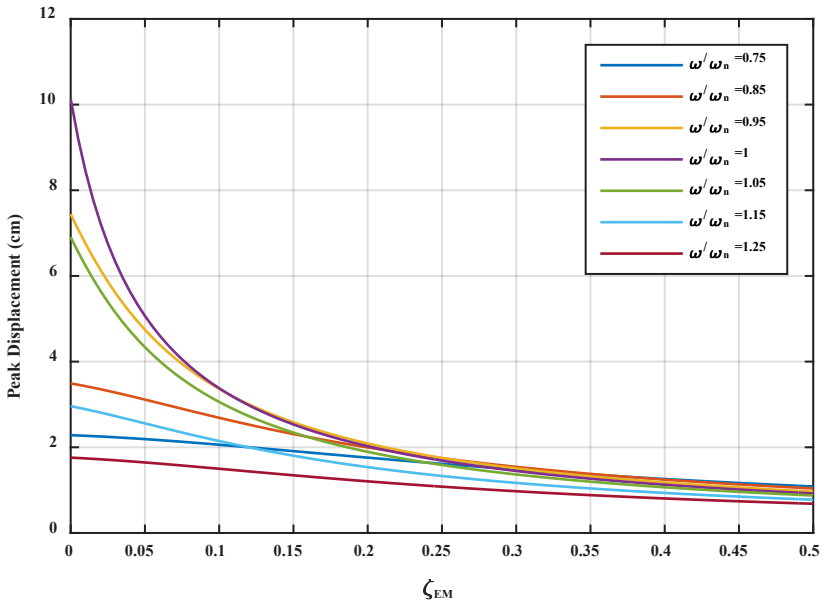

Figure 2.8 Peak displacement versus ζ_{EM} for various values of ω/ω_n and ζ_s = 5%

2.5. Summary and Major Findings

Based on the analytical and computational investigations of this chapter the following key findings may be identified:

- The optimum EM damping ratio, ζ_{EM}, is only dependent on the forcing frequency ratio (i.e. the ratio of the forcing frequency to natural frequency of the structure), ω/ω_n, and the inherent structural damping ratio, ζ_s.
- For slowly varying loading, i.e. ω/ω_n approaching zero, and rapidly varying loads, i.e. ω/ω_n equal to 1.25 or greater, the optimal EM damping ratio is very high and the obtained EM power is very small (< 5 W for the example structure considered here). Also, the damping provided by the structure has very little effect on the optimum EH damping ratio for these values of ω/ω_n.
- For all levels of structural damping, the optimum EM damping ratio is lowest for the resonant response, i.e. $\omega/\omega_n = 1$. In this case, the optimum EM damping ratio is equal to the damping ratio of the structure.
- The optimum damping ratio for EH may not be practical for VM. This is illustrated by comparing Figure 2.3 and Figure 2.4 with Figure 2.7 and Figure 2.8. The resonant response in these figures, paired with low EM damping ratios, were optimum for EH but also resulted in large peak displacements.

When investigating the EH potential of a multistory building, the system can be first modeled as a SDF system and Eq. (2-27) can be used to estimate the damping ratio of the EH dampers that will maximize EM power if the system is subjected to harmonic loading. In this study, the loading that will be investigated for energy harvesting will be wind loading in both the along-wind and across-wind directions (discussed more in Chapter 4). In reality, wind loads

produce forces that act in a range of frequencies as opposed to just a single frequency as considered here. However, from the fluctuating wind speed and across-wind force spectra (discussed in Chapter 4), we can determine which forcing frequencies will be dominant in the dynamic response of the structure, which can be used Eq. (2-27) to estimate the optimum damping ratio provided by the EH damper. It should be noted that the scenario described here assumes the damping provided the EH damper is purely viscous. As will be shown in Chapter 3, the EH damper used in this study has frictional components which result in a response of the EH damper that is not purely viscous making the estimation of the optimum damping ratio and response of the system more difficult.

Although the SDF system and loading scenario described here is a simplified description of a true structural system, this chapter does illustrate critical points regarding large scale energy harvesting of civil structures with EM EH dampers. First, the rate at which energy is harvested does not monotonically increase with the damping ratio provided by the EH damper. There is an optimum damping ratio that maximizes EM power, above which the amount energy entering the system decreases which results in a decrease in the amount of available energy to be harvested. Second, there are competing goals between EH and VM. Under extreme loading conditions, occupant safety and comfort is the goal of any supplemental damping system. In these cases, the damping ratio would need to be high in order to prevent structural damage and limit building accelerations to acceptable levels based on occupant comfort. This damping ratio may not be the optimum ratio for EH. Chapter 5 investigates the competing goals of EH and VM in more detail.

3. MODELING OF AN ENERGY HARVESTING DAMPER

3.1. Introduction and Objectives

The goal of this chapter is to develop and validate a mathematical model of an electromagnetic (EM) energy harvesting (EH) damper that can be used for numerical simulations of tall buildings subject to wind and seismic loading. The EM EH damper used in this research is the EH damper proposed by Cassidy et al. (2011). The mathematical model is calibrated and validated against experimental data by Cassidy et al. (2011).

3.2. Mathematical Model

In the EH damper shown below in Figure 3.1, linear motion, $x(t)$, is converted to rotational motion, $\theta_m(t)$, via a lead-screw, which is transferred to the shaft of an EM motor through a timing belt. The energy from the rotation of the motor shaft is converted to electricity, which can then be used by the structure or sent back to the power grid.

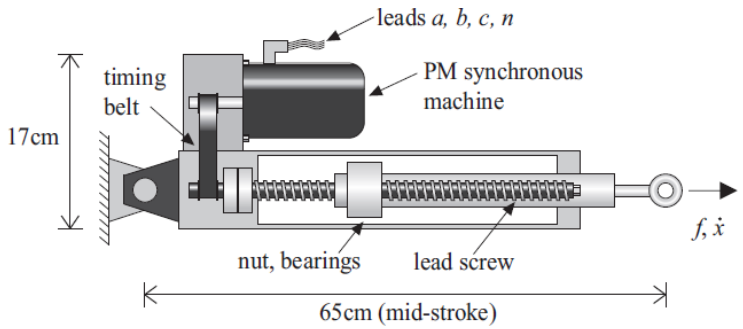

Figure 3.1 Electromagnetic energy harvesting damper (Cassidy et al., 2011)

An idealized mechanical model of this particular EH damper, as proposed by Cassidy et al. (2011), is shown in Figure 3.2. The mass element, m_d, represents the inertia that is present in the system. This model has two "displacement" degrees of freedom, where the first degree of freedom, $x(t)$, models the linear motion of the damper arm, while the second degree of freedom,

$y(t)$, equivalently models the rotation of the device. Losses due to the friction between the lead-screw and bearings are represented by $f_{bearings}$, while friction amongst other parts of the damper is holistically described with the term f_c. Cassidy et al. (2011) also accounted for potential slackness in the timing belt and tolerances between the timing belt and the connected shafts through a belt force, f_{belt}, which followed a nonlinear stiffening response, given as:

$$f_{belt} = k_{b1} y + k_{b3} y^3 \tag{3-1}$$

Based on electrical engineering principles and the characteristics of the EM motor chosen for the EH damper, the equivalent EM viscous damping constant, c_{EM}, was derived in Cassidy et al. (2011) to be:

$$c_{EM} = \frac{9K_e^2}{4l^2(R + R_L)} \tag{3-2}$$

where c_{EM} has units of linear force over linear velocity, while K_e and R are constants that depend on the motor, R_L is the resistive load provided by the motor which can be varied to achieve a desired level of damping, and l is the conversion factor that converts linear to rotational motion, as discussed below. Note that, Cassidy et al. (2011) refers to the damping constant given in Eq. (3-2) as "c_e" as shown in Figure 3.2; it was decided for this study to refer to this term as "c_{EM}" to maintain consistency throughout this thesis. While the response of the idealized mechanical model proposed in Cassidy et al. (2011) was shown to match the experimental response of the EH damper, it does not explicitly model the load path and motion transfer amongst the different components of the damper. Moreover, it includes an inertial term, which makes the prediction of the response of the damper computationally expensive.

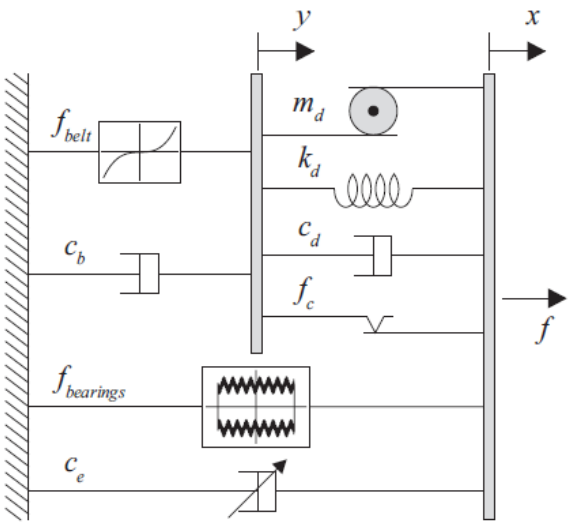

Figure 3.2 Mechanical model of EH damper proposed by Cassidy et al. (2011)

Before proposing a model that accurately accounts for the actual load path and motion transfer between the mechanical components of the EH damper, the motion transfer should be understood. Via inspection of the actual device, it is observed that *linear motion*, $x(t)$, is converted to *rotation at the bearing*, $\theta_b(t)$, which is then transferred at the end of the lead-screw as *lead-screw rotation*, $\theta_s(t)$, and, subsequently, transferred to the motor as *motor shaft rotation*, $\theta_m(t)$, via the timing belt. This observation results in the following mathematical association:

$$\begin{cases} x(t) \rightarrow \theta_b(t) \rightarrow \theta_s(t) \rightarrow \theta_m(t) \\ \text{with } \; x(t) = l\theta_b(t) \end{cases} \tag{3-3}$$

where l is the conversion factor that converts linear to rotational motion at the bearing (see Figure 3.1).

On the basis of this observation, the model of Figure 3.3 is proposed. This model includes three degrees of freedom, $x(t)$, $y(t)$ and $z(t)$. It is noted that $y(t)$ and $z(t)$ are "equivalent" displacements representing the lead-screw rotation, $\theta_s(t)$, and motor shaft rotation, $\theta_m(t)$, respectively. On the basis of Eq. (3-3), these "equivalent" displacements are related to the aforementioned physical rotations, as:

$$\begin{cases} y(t) = l\theta_s(t) \\ z(t) = l\theta_m(t) \end{cases} \tag{3-4}$$

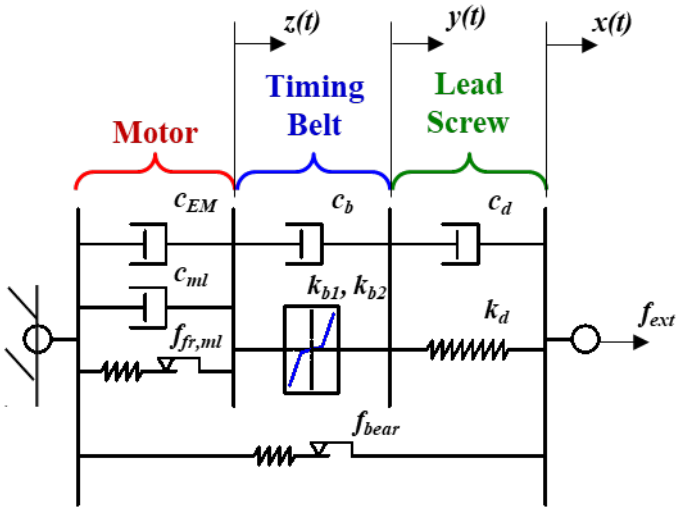

Figure 3.3 Mechanical model investigated in this research

In the proposed model (Figure 3.3), the motor is represented by two dashpots and a friction element, all in parallel to each other. The dashpots represent the harvested energy and the inherent system damping, while the friction element represents internal friction losses. The constitutive relation of the motor is given as:

$$f_{motor} = \underbrace{c_{EM}\,\dot{z}(t)}_{f_{EM}} + \underbrace{c_{ml}\,\dot{z}(t) + f_{fr,ml}}_{f_{loss}} \tag{3-5}$$

where the friction term is given by a uniaxial plasticity model as:

$$\begin{cases} \Delta f_{fr,ml} = k_{ml}\Delta z \\ \text{with } \left| f_{fr,ml} \right| \le f_{fr,ml,\max} \end{cases} \tag{3-6}$$

and c_{ml} is the damping constant for inherent damping losses within the EM motor, c_{EM} is the constant representing the harvested energy (i.e. "damping" converted to electricity), k_{ml} is the elastic stiffness of the friction element, and $f_{fr,ml,max}$ is the peak friction reaction.

For the timing belt, the total belt force, f_{belt}, is modeled as the combination of a bi-linear stiffening spring and a viscous damper, as:

$$f_{belt} = k_{b1}\left(y-z\right) + k_{b2}\left(\left|y-z\right|-u_c\right)\mathrm{sgn}\left(y-z\right)H\left(\left|y-z\right|-u_c\right) + c_b\left(\dot{y}-\dot{z}\right) \tag{3-7}$$

where the parameter u_c represents the displacement slack of the timing belt and marks the initiation of stiffening, while k_{b1} is the belt stiffness in the presence of slackness and k_{b2} is the stiffness that controls stiffening after the slack has been eliminated. The sum of k_{b1} and k_{b2} represents the total stiffness of the timing belt after elimination of the slackness. The Heaviside function is included to indicate that the stiffness represented by the term k_{b2} is not present until the slack is eliminated, i.e. when the absolute value of the y-z is greater than u_c. Also, the signum function is used to obtain the sign of the reaction force, f_{belt}.

The reaction of the lead-screw, f_d, is obtained as:

$$f_d = k_d\left(x-y\right) + c_d\left(\dot{x}-\dot{y}\right) \tag{3-8}$$

where k_d and c_d are the stiffness and damping constant of the lead screw. Because the lead screw is expected to be very stiff to efficiently transfer the linear motion to the timing belt, k_d is expected to be large. Also, the damping constant, c_d, which represents material damping is expected to be small.

Finally, the friction losses from bearing/sliding contact between the different components of the EH damper is holistically considered by the bearing friction spring of Figure 3.3 as:

$$\begin{cases} \Delta f_{bear} = k_{bear}\Delta x \\ \text{with } \left|f_{bear}\right| \le f_{bear,yld} \end{cases} \tag{3-9}$$

where k_{bear} is the stiffness of the friction spring, and, $f_{bear,yld}$, is the yield force, given as:

$$f_{bear,yld} = \gamma_0 + \gamma_1 \sin\left(\frac{x(t)}{l} + \phi_1\right) + \gamma_2 \sin\left(\frac{\pi x(t)}{d \sin\beta} + \phi_2\right) \geq 0 \quad (3\text{-}10)$$

where γ_0, γ_1, and γ_2 are parameters representing force. Force γ_0 is constant, while forces γ_1 and γ_2 vary in a sinusoidal manner with the applied displacement, $x(t)$, as shown in Eq. (3-10). Also, ϕ_1 and ϕ_2 are phase angles for the sinusoidal terms, d and β are the diameter of the bearings and helical angle of the ball screw, and l is the lead conversion, described previously. The yield bearing force of Eq. (3-10) is a modified expression of the bearing force given in Cassidy et al. (2011).

Overall, the total force reaction of the EH damper is given as:

$$f_{ext}(t) = f_d(t) + f_{bear}(t) = f_{belt}(t) + f_{bear}(t) = f_{motor}(t) + f_{bear}(t) \quad (3\text{-}11)$$

In terms of its physical interpretation, the proposed model (Figure 3.3) differs from the model by Cassidy et al. (2011) in the following aspects:

- It accounts for the actual load path and motion transfer amongst the mechanical components of the EH damper.
- It accounts for friction losses via uniaxial plasticity elements
- It avoids use of mass/inertial terms that increase the computational effort without adding to the accuracy of the model.

3.3. Solution and Computational Implementation

For given applied displacement, $x(t)$, solution of the aforementioned mathematical model will provide all force reactions, $f_{bear}(t)$, $f_d(t)$, $f_{belt}(t)$, $f_{motor}(t)$, and $f_{ext}(t)$, as well as the internal "equivalent" displacements, $y(t)$ and $z(t)$. Solution can be achieved by implementing equilibrium

between the different EH damper components, which results in the following equilibrium equations:

$$\begin{cases} f_{belt}(t) - f_{motor}(t) = 0 \\ f_d(t) - f_{belt}(t) = 0 \end{cases} \tag{3-12}$$

Because all forces in the above equation are functions of the displacements, for given $x(t)$, $y(t)$ and $z(t)$ should be sought, so that equilibrium is satisfied. This can be achieved via Newton-Raphson (N-R) Iterations.

To implement N-R iteration, the equilibrium function is set to be:

$$\vec{R}(\vec{r}) = \begin{Bmatrix} f_{belt}(t) - f_{motor}(t) \\ f_d(t) - f_{belt}(t) \end{Bmatrix}, \quad \text{with} \quad \vec{r} = \begin{Bmatrix} y(t) \\ z(t) \end{Bmatrix} \tag{3-13}$$

For the i-th time instant, t_i, the N-R iteration can be written as:

$$\vec{r}_{i,j} = \vec{r}_{i,j-1} - \left[\left. \frac{\partial \vec{R}(\vec{r}_i)}{\partial \vec{r}_i} \right|_{\vec{r}_i = \vec{r}_{i,j-1}} \right]^{-1} \vec{R}(\vec{r}_{i,j-1}) \tag{3-14}$$

with j denoting the N-R iterations. The velocities at the i-th time instant can be approximated as:

$$\dot{z}_i = \frac{z_i - z_{i-1}}{t_i - t_{i-1}} \quad \text{and} \quad \dot{y}_i = \frac{y_i - y_{i-1}}{t_i - t_{i-1}} \tag{3-15}$$

The Jacobian is given as:

$$\frac{\partial \vec{R}(\vec{r}_i)}{\partial \vec{r}_i} = \begin{Bmatrix} \left. \frac{\partial f_{belt}}{\partial y} \right|_{y=y_i} - \left. \frac{\partial f_{motor}}{\partial y} \right|_{y=y_i} & \left. \frac{\partial f_{belt}}{\partial z} \right|_{z=z_i} - \left. \frac{\partial f_{motor}}{\partial z} \right|_{z=z_i} \\ \left. \frac{\partial f_d}{\partial y} \right|_{y=y_i} - \left. \frac{\partial f_{belt}}{\partial y} \right|_{y=y_i} & \left. \frac{\partial f_d}{\partial z} \right|_{z=z_i} - \left. \frac{\partial f_{belt}}{\partial z} \right|_{z=z_i} \end{Bmatrix} \tag{3-16}$$

with

$$
\begin{cases}
\left.\dfrac{\partial f_{belt}}{\partial y}\right|_{y=y_i} = k_{b1} + k_{b2} H\left(\left|y_i - z_i\right| - u_c\right) + \dfrac{c_b}{t_i - t_{i-1}} \\
\left.\dfrac{\partial f_{belt}}{\partial z}\right|_{z=z_i} = -k_{b1} - k_{b2} H\left(\left|y_i - z_i\right| - u_c\right) - \dfrac{c_b}{t_i - t_{i-1}}
\end{cases}
$$

$$
\begin{cases}
\left.\dfrac{\partial f_{motor}}{\partial y}\right|_{y=y_i} = 0 \\
\left.\dfrac{\partial f_{motor}}{\partial z}\right|_{z=z_i} = \dfrac{c_{EM}}{t_i - t_{i-1}} + \dfrac{c_{ml}}{t_i - t_{i-1}} + \left.\dfrac{\partial f_{fr,ml}}{\partial z}\right|_{z=z_i}
\end{cases}
\tag{3-17}
$$

$$
\begin{cases}
\left.\dfrac{\partial f_d}{\partial y}\right|_{y=y_i} = -k_d - \dfrac{c_d}{t_i - t_{i-1}} \\
\left.\dfrac{\partial f_d}{\partial z}\right|_{z=z_i} = 0
\end{cases}
$$

The friction force of the EH damper is computed as:

$$
\begin{cases}
f_{fr,ml,i,j} = f_{fr,ml,i-1} + k_{ml}\left(z_{i,j} - z_{i-1}\right) \\
\text{with} \begin{cases}
f_{fr,ml,i,j} = f_{fr,ml,\max} \quad , if \quad f_{fr,ml,i-1} + k_{ml}\left(z_{i,j} - z_{i-1}\right) > f_{fr,ml,\max} \\
f_{fr,ml,i,j} = -f_{fr,ml,\max} \quad , if \quad f_{fr,ml,i-1} + k_{ml}\left(z_{i,j} - z_{i-1}\right) < -f_{fr,ml,\max}
\end{cases}
\end{cases}
\tag{3-18}
$$

Similarly, the friction force due to bearing/sliding contact between the different components of the EH damper is computed as:

$$
\begin{cases}
f_{bear,i} = f_{bear,i-1} + k_{bear}\left(x_i - x_{i-1}\right) \\
\text{with} \begin{cases}
f_{bear,i} = f_{bear,yld,i} \quad , if \quad f_{bear,i-1} + k_{bear}\left(x_i - x_{i-1}\right) > f_{bear,yld,i} \\
f_{bear,i} = -f_{bear,yld,i} \quad , if \quad f_{bear,i-1} + k_{bear}\left(x_i - x_{i-1}\right) < -f_{bear,yld,i}
\end{cases} \\
\text{and} \quad f_{bear,yld,i} = \gamma_0 + \gamma_1 \sin\left(\dfrac{x_i}{l} + \phi_1\right) + \gamma_2 \sin\left(\dfrac{\pi x_i}{d \sin\beta} + \phi_2\right) \geq 0
\end{cases}
\tag{3-19}
$$

Once convergence of the Newton-Raphson iterations has been achieved, i.e. when $\left\|\vec{R}\left(\vec{r}_{i,j-1}\right)\right\| < tolerance$, the total reaction force of the EH damper is given as:

$$f_{ext,i} = \underbrace{c_{EM}\,\dot{z}\left(t_i\right)}_{f_{EM,i}} + \underbrace{c_{ml}\,\dot{z}\left(t_i\right) + f_{fr,ml,i}}_{f_{loss,i}} + f_{bear,i} \tag{3-20}$$

The force associated with the harvested energy is obtained as

$$f_{EM,i} = c_{EM}\dot{z}_i \tag{3-21}$$

The corresponding harvested electrical energy can be determined by integration of the electromechanical force with respect to $z(t)$.

3.4. Model Calibration

Calibration of the model parameters was done using a similar method used by Cassidy et al. (2011) where a displacement history, $x(t)$, is applied to the device and the model parameters are determined by minimizing the quadratic norm of error between the predicted damper force, $f_{ext}(t)$, and the measured damper force, $f_{ext,measured}(t)$, from lab experiments. The displacement history used for calibration is a sine sweep displacement as shown in Figure 3.4. This displacement history was chosen by Cassidy et al. (2011) as it has contains a wide range of frequencies as well as varying displacement magnitudes. For the calibration, the terminals of the EM motor were left open resulting in no EM damping by the device ($c_{EM} = 0$). For the device used in this investigation, the values of l, d, and β from Eq. (3-10) are equal to 0.255 cm/rad, 0.29 cm, and 0.297 rad, respectively.

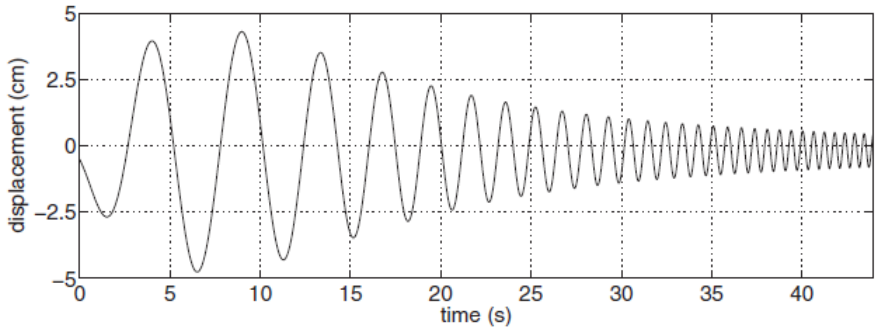

Figure 3.4 Sine sweep displacement time history used for calibration (Cassidy et al., 2011)

Using a plot digitizing software, the input data from Figure 3.4 as well as the measured force response were extracted from Cassidy et al. (2011) to be used in the calibration of the proposed model. The optimal model parameters were determined using the nonlinear least squares function in MATLAB. The final calibrated values are shown below in Table 3.1.

Table 3.1. Calibrated model parameters

Parameter	Value	Parameter	Value
k_d (N/cm)	1.00x10^6	k_{ml} (N/cm)	5.87x10^6
c_d (N-s/m)	0.223	γ_0 (N)	57.1
k_{b1} (N/cm)	154	γ_1 (N)	7.12
k_{b2} (N/cm)	7.09x10^3	γ_2 (N)	1.00
u_c (cm)	4.27x10^{-5}	ϕ_1 (rad)	2.2
c_b (N-s/cm)	0.154	ϕ_2 (rad)	-1.02
c_{ml} (N-s/cm)	3.82	k_{bear} (N/cm)	3.21x10^6
$f_{fr,ml,max}$ (N)	95.7		

In Table 3.1, k_{bear} and k_{ml} are the elastic stiffness parameters for the bearing and EM friction forces, respectively. Figure 3.5 shows the predicted response of the system as well as the measured response from experiments done by Cassidy et al. (2011). Figure 3.6 shows the force versus displacement and force versus velocity relationships for the model and Figure 3.7 shows this same data from Cassidy et al. (2011).

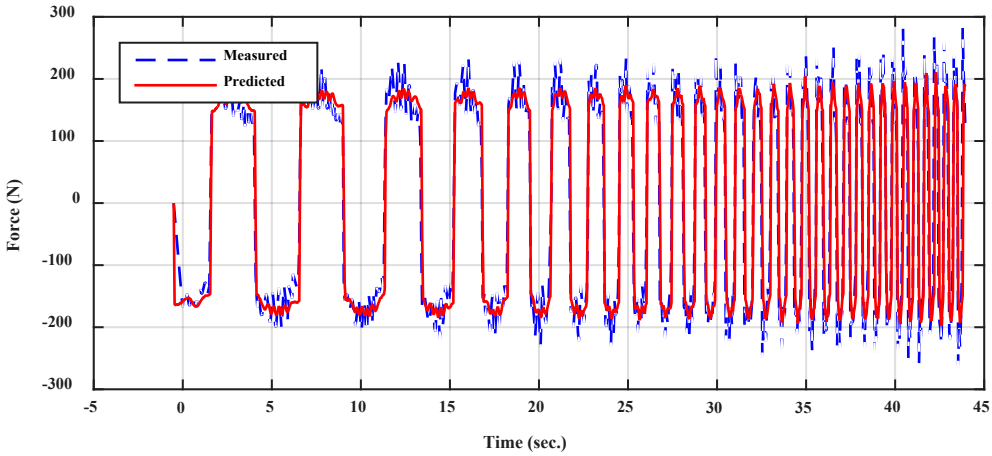

Figure 3.5 Predicted and measured response for sine sweep test

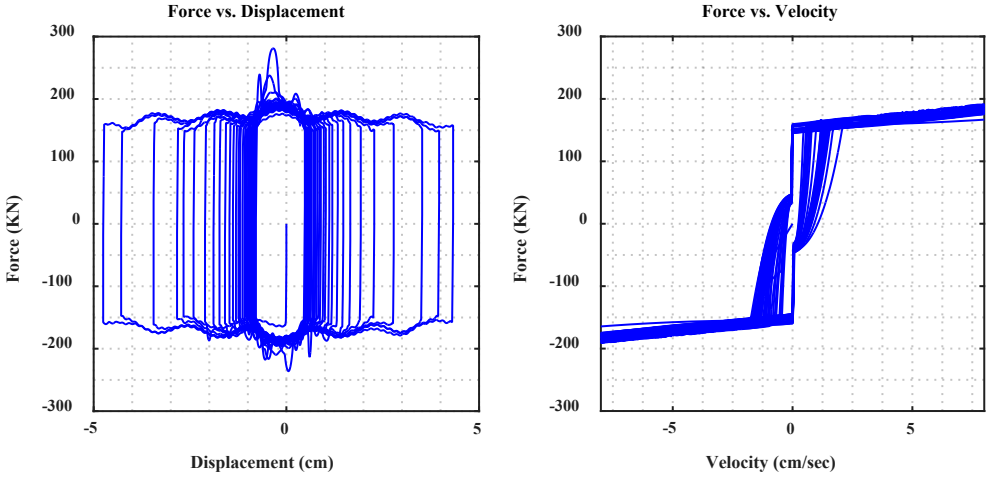

Figure 3.6 Force versus displacement and force versus velocity predicted by model for sine sweep test

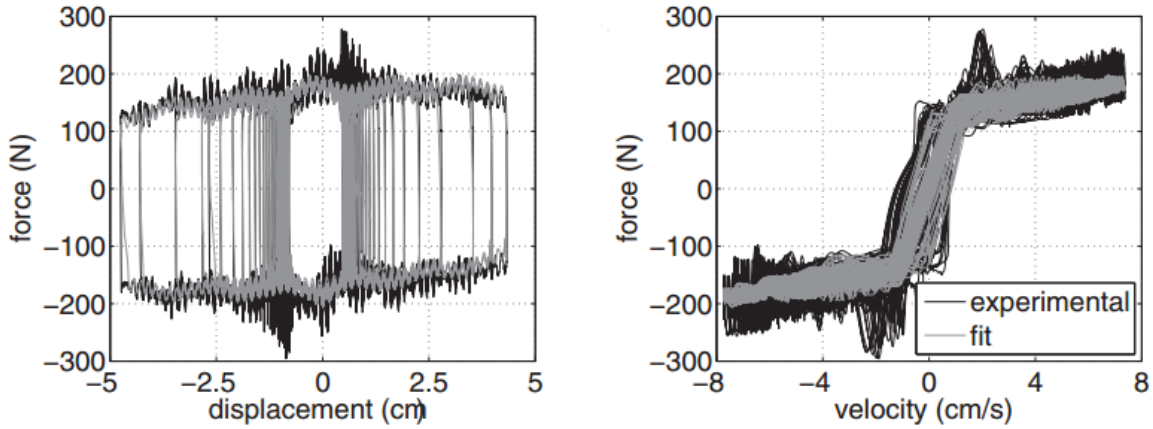

Figure 3.7 Force versus displacement and force versus velocity for sine sweep test from Cassidy et al. (2011)

The displacement and velocity histories for each degree of freedom are shown in Figure 3.8. Because the timing belt and lead-screw are selected to be stiff, so that they efficiently transfer the applied motion to the motor, the calibrated values of k_d and k_{b2} were large. Additionally, for this particular system, the slack was small ($u_c \approx 10^{-5}$ cm), resulting in the $x(t)$, $y(t)$ and $z(t)$ to be nearly identical at all times, as shown in Figure 3.8.

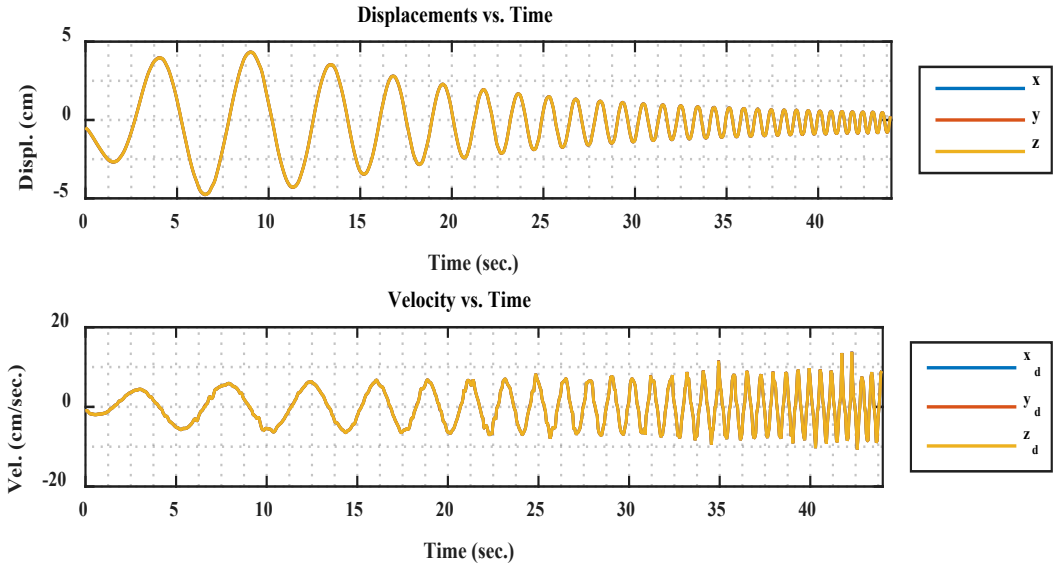

Figure 3.8 Displacement and velocity time histories predicted by model for sine sweep test

The developed model was subsequently used to predict the response due to a random displacement with the EM motor active (i.e. c_{EM} equal to a non-zero value). The random displacement used for this test is shown in Figure 3.9. Again, this response history and the measured response from Cassidy et al. (2011) were extracted using the plot digitizer software for use in MATLAB.

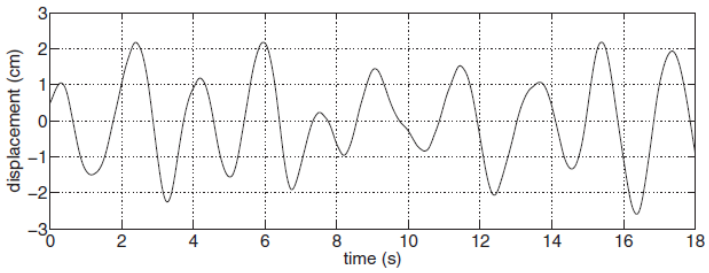

Figure 3.9 Random displacement time history (Cassidy et al., 2011)

The values of K_e and R from Eq. (3-2) are equal to 0.77 N-m/A and 2.41 Ω respectively for the EM motor considered here. For this test, the load resistance, R_L, applied by the motor was 16 Ω which gives a value of c_{EM} equal to 111.26 N-s/cm, per Eq. (3-2). The predicted and measured responses for this test are shown in Figure 3.10. Figure 3.11 shows the force versus displacement and force versus velocity for this test. Figure 3.12 shows the same data from Cassidy et al. (2011). Comparing Figure 3.10 through Figure 3.12 shows that the model proposed here is able to accurately predict the behavior of the device when the EM motor is activated.

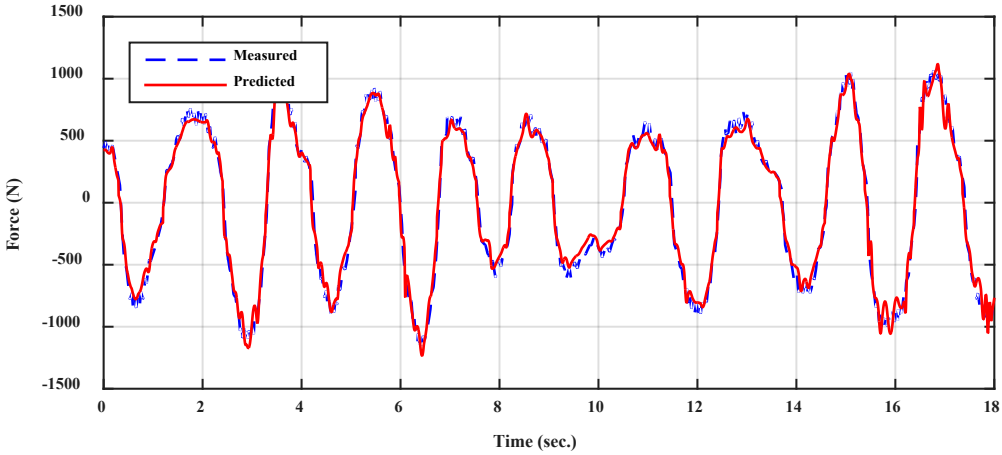

Figure 3.10 Predicted and measured response for random displacement test

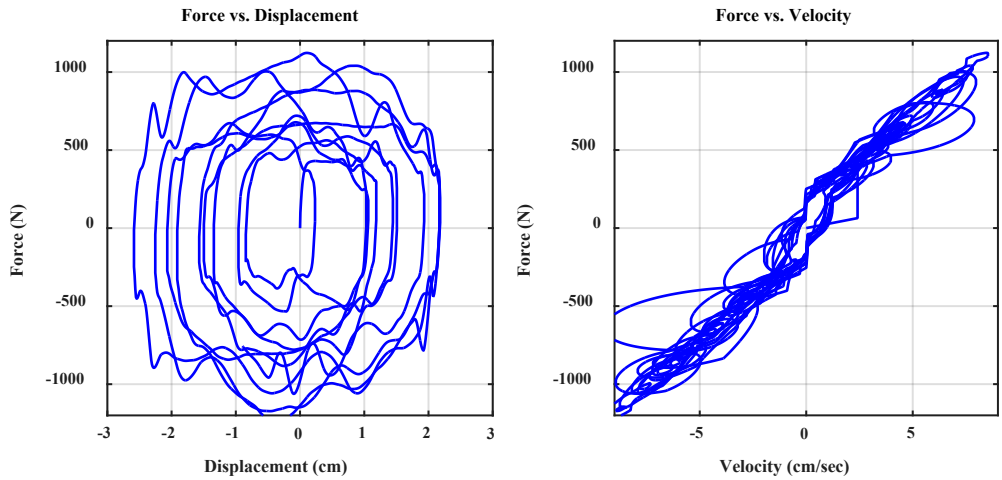

Figure 3.11 Force versus displacement and force versus velocity predicted by model for random displacement test

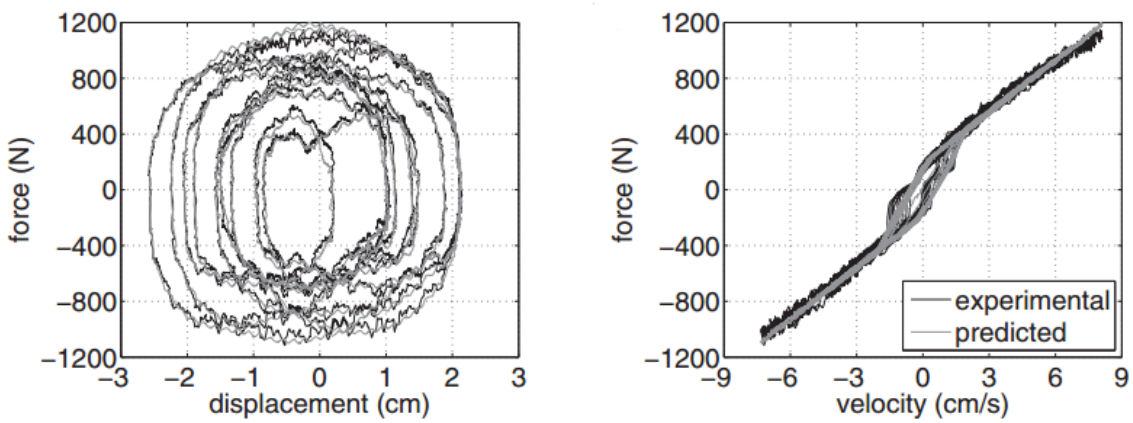

Figure 3.12 Force versus displacement and force versus velocity for random displacement test from Cassidy et al. (2011)

Figure 3.13 shows the displacement and velocity time histories for the random displacement test and Figure 3.14 shows the force time histories for all individual components. The term f_{loss} accounts for losses due the friction force, $f_{fr,ml}$, and the damping force within the EM motor associated with the damping constant c_{ml}. These forces are referred to as losses because they are forces that are dissipated by the EM motor, but not converted to useable EM energy.

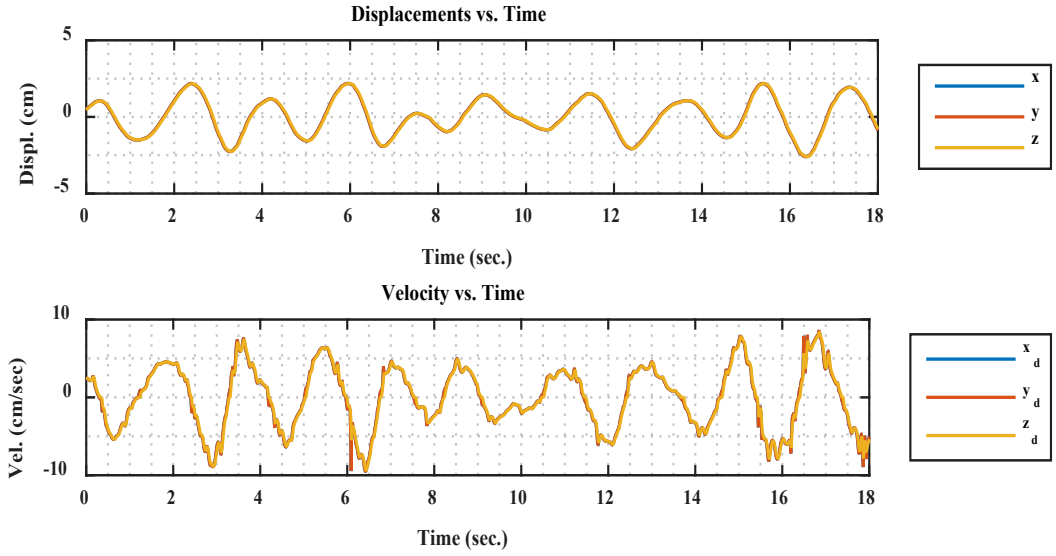

Figure 3.13 Displacement and velocity time histories predicted by the model for random response test

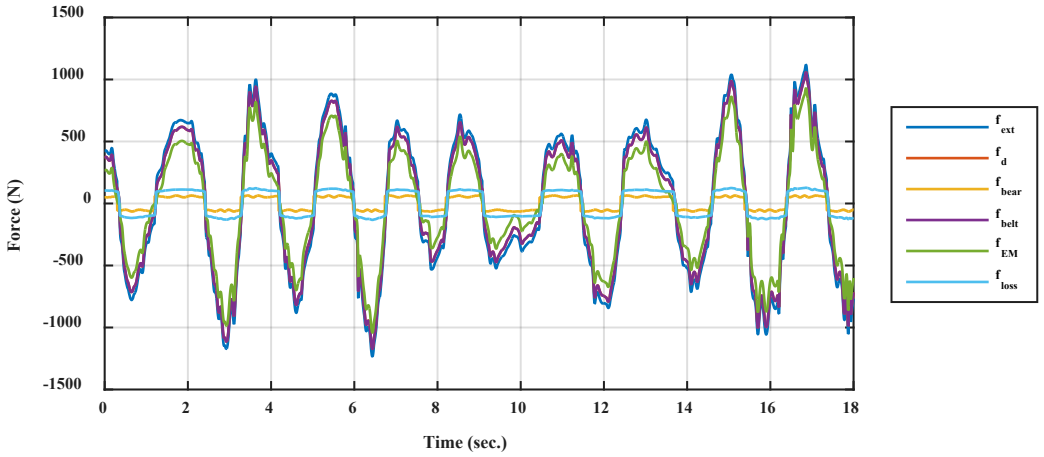

Figure 3.14 Force time histories for random displacement test

3.5. Model Simplification

Because the timing belt and lead-screw are selected to be stiff, so that they efficiently transfer the applied motion to the motor (k_d and k_{b2} are large) and as long as the slack of the timing belt remains small (e.g., $u_c \approx 10^{-5}$ cm), it is observed that $x(t) \approx y(t) \approx z(t)$. Taking advantage of this observation, the solution of the aforementioned mathematical model can be simplified, by setting $y(t) = x(t)$ and $z(t) = x(t)$. In this case, all forces – i.e. f_{bear} and f_{EM} – can be

computed at a single step and the N-R iterations are dropped. Forces f_d and f_{belt} equal f_{EM} ($f_d = f_{belt} = f_{EM}$) at all times. This simplification can result in significant analysis time savings, particularly for cases for which EH dampers are distributed throughout the height of multi-story buildings.

Figure 3.15 and Figure 3.16 show the force versus displacement and force versus velocity plots for the sine sweep and random displacement test, respectively, using this simplified model. The force versus response curves for the two proposed models are very similar for the sine sweep test (Figure 3.6 and Figure 3.15), however when comparing Figure 3.11 and Figure 3.16, it can be seen that the simplified model does not capture the hysteresis (in the force vs. velocity plot) that is present in the actual system as well as the proposed three degree of freedom model. Despite this drawback, the simplified version of the proposed model provides sufficient accuracy to perform a preliminary feasibility assessment of implementing these EH dampers into large civil structures.

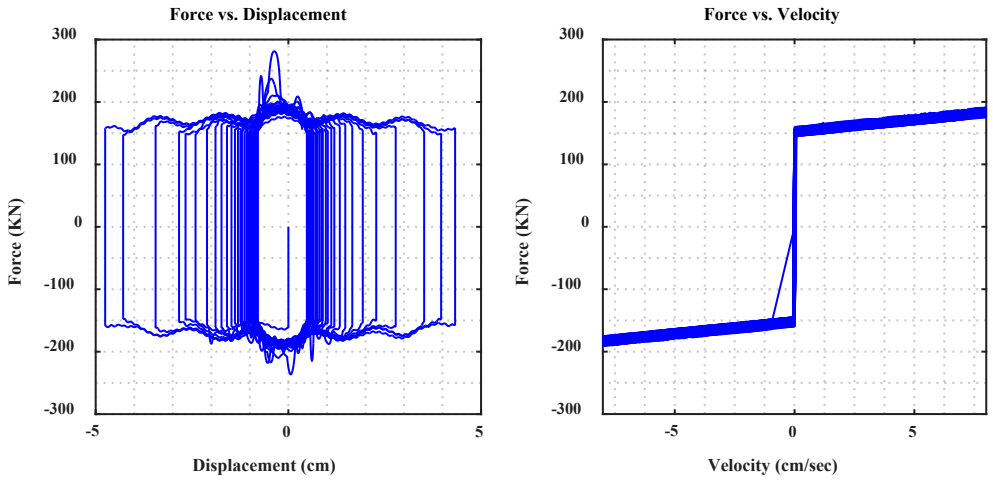

Figure 3.15 Force versus displacement and force versus velocity for simplified model and sine sweep test

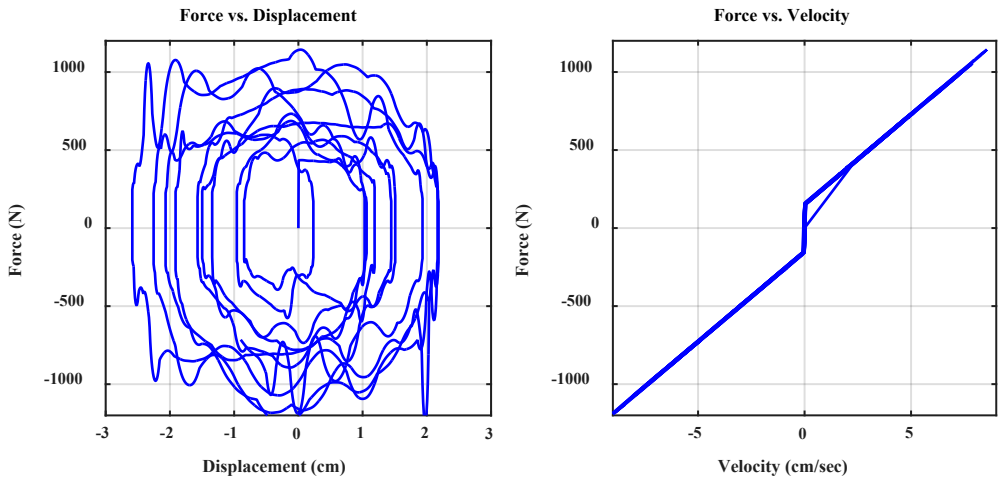

Figure 3.16 Force versus displacement and force versus velocity for simplified model and random displacement test

3.6. Summary and Conclusions

In this chapter, a mathematical model for an EM damper was developed based on the EH damper proposed by Cassidy et al. (2011). The parameters describing the mathematical model were calibrated to match experimental data from Cassidy et al. (2011). The calibrated parameters produced a model that more accurately described the internal load path of the damper components while giving a prediction of damper behavior that was in agreement with the results of the experiments from Cassidy et al. (2011). The model also allowed for simplifications which decreased computational time while maintaining sufficient accuracy.

When this type of EH damper is used in a structure, this model can then be used in the dynamic analysis to determine its effect on the structure response and estimate the harvested EM energy. The ability to vary R_L also provides the advantage of allowing for a control algorithm to be developed which varies the damping provided by the EH damper to optimize the response of the structure based on the design objective, (energy harvesting versus vibration mitigation). However, this control algorithm is beyond the scope of this study. In Chapter 5, the effectiveness

of the damper as an energy harvester under moderate wind loading, as well as its ability to mitigate the effects of earthquake ground motions and extreme winds, will also be investigated.

4. GENERATION OF WIND FORCES FOR ENERGY HARVESTING ANALYSIS

4.1. Introduction and Objectives

The objective of this chapter is to outline a method that generates along- and across-wind force time histories over the height of buildings for given reference mean wind speeds. Along-wind force time histories will be generated based wind speed time histories, which will in turn be generated from fluctuating wind speed power spectra, converting from the frequency domain to the time domain. Similarly, across-wind force time histories will be generated from across-wind force power spectra. The correlation of the wind speeds over the height of buildings at a given time instant is also discussed.

4.2. Generation of Wind Speed Time Histories

Wind speed time histories are typically assumed to include two components, namely, a *mean* wind speed, $V_m(z)$, which varies only spatially (over the height, z), and a *fluctuating* wind speed, $V_f(z,t)$, which varies spatially and temporally (over time, t). The total wind speed time history is given as:

$$V(z,t) = V_m(z) + V_f(z,t) \tag{4-1}$$

The variation of mean wind speed with height, also termed *mean wind speed profile*, is a function of several factors, including the atmospheric pressure gradient and the Coriolis Force. Additionally, within the atmospheric boundary layer, the friction between the ground surface and air mass slows the flow of air near the ground surface with rougher ground surfaces having a greater effect on the mean wind speed profile. The height of the atmospheric boundary layer, or

the height at which ground friction no longer affects the mean wind speed, is known as the gradient height. Detailed information on the nature of air flow and wind speed can be found in the literature (Holmes, 2015; Kaltschmitt, Streicher, & Wiese, 2007; Simiu, 2011; Simiu & Scanlan, 1996).

4.2.1. Mean Wind Speed Profile

Two methods are commonly used in wind engineering to estimate the mean wind speed profile, $V_m(z)$. The first method is referred to as the *Logarithmic Law* and gives the wind speed at a given height above ground, z, as:

$$V_m(z) = 2.5u_* \ln\left(\frac{z}{z_0}\right) \tag{4-2}$$

where z_0 is the surface roughness length, a measure of the roughness of the surrounding terrain and height of obstructions upwind of the structure, and u_* is the friction velocity, which is given as:

$$u_* = \sqrt{\tau_0 / \rho_a} \tag{4-3}$$

In Eq. (4-3), τ_0 is the shear stress exerted by the ground on the flow of air, known as the surface shear stress, and ρ_a is the air density.

The terrain type is indicated by the surface roughness length, z_o, a parameter commonly used to predict the turbulence of air flow at a given location. This parameter is a function of the average height and size of obstacles within the flow of air. Therefore, urban areas, typically characterized by many large buildings that impede the air flow, have higher surface roughness lengths, producing more turbulence and higher standard deviations of fluctuating wind speeds compared to open or rural areas. Based on several sources (Australia/New Zealand Standards,

2011; Holmes, 2015; Simiu & Scanlan, 1996), a reasonable estimate of the surface roughness length for urban areas is 2 m.

When computing the mean wind speed, the height, z, is given as:

$$z = z_g - z_d \tag{4-4}$$

where z_g is the height above the ground, and z_d is known as the zero plane displacement, which is the height at which the mean wind speed will be zero due to obstructions to the air flow in the upwind direction. In urban areas, the buildings upwind will block some of the wind from reaching the studied building, and the effective ground height or the origin of the mean wind speed profile will not be at the ground level. Thus, for urban areas, the zero plane displacement, z_d, is a function of the average building height in the upwind direction of the building under consideration. This formulation of z is mostly applicable for urban areas or built up suburbs, since rural areas generally have very few obstructions or obstructions that may be very small compared to the structure being analyzed. Thus, for rural areas, z_d can be assumed to be zero, and z becomes equal to the height above ground, z_g. Because the zero plane displacement, z_d, is a function of the average building height in the vicinity of the studied building, z_d is site specific and can vary depending on where the building is located within an urban area and with the direction of the wind. For simplicity, this proof of concept study will assume a zero plane displacement of zero.

Although the Logarithmic Law has a strong theoretical basis, its practicality is limited due to its form and range of applicability. This relationship is only applicable up to heights of 100 – 200 meters above the ground. (Holmes, 2015). In addition, the logarithmic term will be negative, for $z < z_0$, or undefined, for $z_g < z_d$. A simpler model for the mean wind speed profile is known as the *Power Law*. This model, despite not having a strong theoretical basis, has been

shown to give mean wind speed profiles similar to the Logarithmic Law (Holmes, 2015), yet avoiding its aforementioned weaknesses. The Power Law, which will be used for this study, is given as:

$$V_m(z) = V_r\left(\frac{z}{r}\right)^{\alpha} \tag{4-5}$$

where V_r is an assumed or known reference wind speed at height r and α is the Hellmann exponent, which varies with the terrain type and thermal stability.

The thermal stability is dependent on the temperature gradient which is the change in temperature with altitude. A decrease in absolute temperature with altitude of about 0.98K/100 m is considered an adiabatic temperature gradient and has no influence on the change in mean wind speed with height, thus is considered neutrally stratified. Temperature gradients less than the adiabatic temperature gradient are considered stably stratified and will result in a greater increase in mean wind speed, i.e. a higher Hellmann exponent. The opposite is the case for higher temperature gradients; these are considered unstably stratified and will result in a smaller increase in mean wind speed profile, i.e. a lower Hellmann exponent. High wind speeds create a mixing effect within the air and, as a result, the temperature gradient has little effect on the change in mean wind speed with height. In this case, which is the case of interest for most structural design applications, the air can be considered neutrally stratified. As suggested by Simiu and Scanlan (1996), mean wind speeds of about 12.5 m/s or greater will result in a negligible impact on the wind speed profile by the thermal stability. Figure 4.1 shows the mean wind speed profiles for the three thermal stability scenarios in an urban area. The reference wind speed, V_r, in Figure 4.1 is assumed to be 5 m/s at a reference height, r, of 10 m. The values assumed for the Hellmann constant, α, are from Table 2.3 of Kaltschmitt et al. (2007).

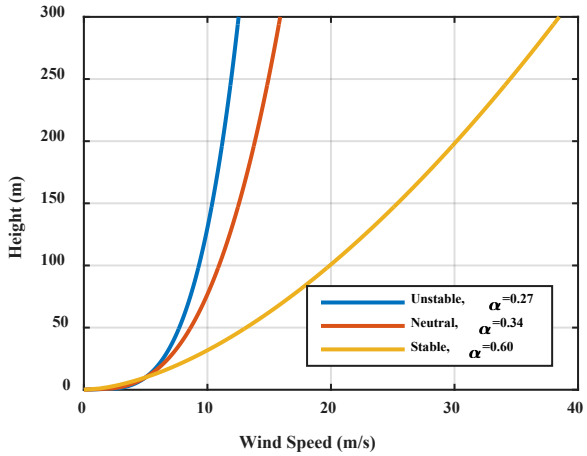

Figure 4.1 Mean wind speed profiles for unstably, neutrally, and stably stratified temperature gradients (Kaltschmitt et al. 2007, Table 2.3)

For simplicity, this study will assume neutral stratification regardless of the wind speed and temperature gradient. From an energy harvesting perspective, this is a conservative assumption, since, per Figure 4.1, for low wind speeds, an air mass with a stable stratification has significantly higher mean wind speeds, which could result in a larger dynamic response of the building, thus more potential energy to be harvested. For this study, the Hellmann exponent will be assumed to be 0.33 as suggested by Simiu and Scanlan (1996) for urban areas. This value for α is assumed to be valid within the entire atmospheric boundary layer, which, from Simiu and Scanlan, is equal to 457 m (about 1500 ft.), well within the range of building heights considered for this study.

4.2.2. Fluctuating Wind Speeds

The fluctuating wind speeds will be generated using a fluctuating wind speed power spectrum and converting it to the time domain with an inverse Fourier transform algorithm. Three models were considered for the wind spectrum. The first spectrum, referred to as *Spectrum 1*, is given in Holmes (2015) and has been adopted in *Recommendations for Loads on Buildings*

published by the Architectural Institute of Japan (Architectural Institute of Japan, 2004) (RLB-AIJ). *Spectrum 1* is given as:

$$S(f,z) = \sigma_v^{\,2} \frac{4L(z)}{V_m(z)\left(1+70.8\left(\frac{fL(z)}{V_m(z)}\right)^2\right)^{\frac{5}{6}}} \tag{4-6}$$

where $L(z)$ is the turbulence integral-length scale at height z, $V_m(z)$ is the mean wind speed at height z, and σ_v is the standard deviation of the wind speed time history, f is the frequency in Hz, and the resulting power spectrum, $S(f,z)$, is in units of m^2/sec. The turbulence integral-length scale, $L(z)$, is a measure of the average size of turbulent eddies of the flow (Simiu & Scanlan, 1996). Design codes generally present this term in the form of an empirical equation that fits measured data. The turbulence length scale given by RLB-AIJ is:

$$L(z) = 100\left(\frac{z}{30}\right)^{.5} \tag{4-7}$$

The standard deviation, σ_v, of fluctuating wind speed is a function of the friction velocity, u_*. However, when calculating u_* from Eq. (4-3), the surface shear stress, τ_0, is not easily calculated or measured. As an alternative, u_* can be back-calculated from Eq. (4-2), as long as $V_m(z)$ is known, as

$$u_* = \frac{V_m(z)}{2.5\ln\left(\frac{z}{z_0}\right)} \tag{4-8}$$

From Eq. (4-3), the friction velocity does not vary with the height, assuming the change in air density, ρ_a, is negligible over the height of the building. Therefore, the correct application of Eq. (4-8) is to compute the friction velocity at a single height and mean wind speed and assume that

value for all other heights. If a reference mean wind speed, V_r, at a reference height, r, is known or assumed the friction velocity can be calculated with $V_m(z) = V_r$ and $z = r$ (Simiu and Scanlan, 1996).

The friction velocity can be related to the standard deviation of fluctuating wind speeds by the term η which is the ratio of the standard deviation of fluctuating wind speed and friction velocity and is a function of the surface roughness length, z_0. If η is known and the friction velocity, u_*, is calculated as given above, the standard deviation of fluctuating wind speed is given as

$$\sigma_v = \eta(z_0)\, u_* \tag{4-9}$$

Simiu (2011) gives values of $\eta(z)$ for various surface roughness lengths, z_0. Fitting a logarithmic curve to this data, the following relation between $\eta(z)$ and z_0 is obtained:

$$\eta(z_0) = -0.066 \ln(z_0) + 2.211 \quad (z_0 \text{ in meters}) \tag{4-10}$$

In Eq. (4-9), the standard deviation of fluctuating wind speed is independent of the height, as suggested by Ni et. al (2011). In reality, the standard deviation will vary with the height only in a stochastic sense, i.e. the turbulence of the air flow will result in random variations of standard deviation with height.

The second spectrum considered herein, *Spectrum 2*, is the one adopted in ASCE 7-10, and is given as:

$$S(f,z) = \sigma_v{}^2 \frac{7.47 L(z)}{V_m(z)\left(1 + 10.3\left(\frac{f\, L(z)}{V_m(z)}\right)\right)^{\frac{5}{3}}} \tag{4-11}$$

where the integral turbulence-length scale is now given as (ASCE 7-10):

$$L(z) = l\left(\frac{z}{10}\right)^{\overline{\in}} \tag{4-12}$$

where l and $\overline{\in}$ are dependent on the terrain type and are equal to 97.54 m and 1/3, respectively, for urban areas.

The third spectrum, *Spectrum 3*, considered herein is given in Simiu (2011) and Simiu and Scanlan (1996), and is defined as:

$$S(f,z) = \frac{200u_*^2 z}{V_m(z)\left(1+50\left(\frac{f\,z}{V_m(z)}\right)\right)^{5/3}} \tag{4-13}$$

where the friction velocity, u_*, is calculated as discussed in Eq. (4-8). This spectrum is also used by the NatHaz Online Wind Simulator (Kwon & Kareem, 2006) to generate wind speed histories.

Assuming a reference mean wind speed, V_r, of 10 m/s at a reference height, r, of 10 m and a surface roughness length, z_0, of 2 meters, the friction of velocity, u_*, becomes 2.49 m/s, while the standard deviation, σ_v, of fluctuating wind speeds is computed to be 5.38 m/s. For these values, the fluctuating wind speed power spectra for the three aforementioned spectra models are shown in Figure 4.2. The three spectra all predict high wind speeds at low frequency fluctuations (less than about 0.01 Hz) and have a sharp decline in contribution to the fluctuating wind speed time history as the frequency increases to about 1 Hz. The power spectra levels off in the high frequency range (greater than about 1 Hz). When comparing the three spectra considered here, there are significant differences in the predicted contributions to the fluctuating wind speeds at low frequencies. However, for higher frequencies, the three spectra are very similar.

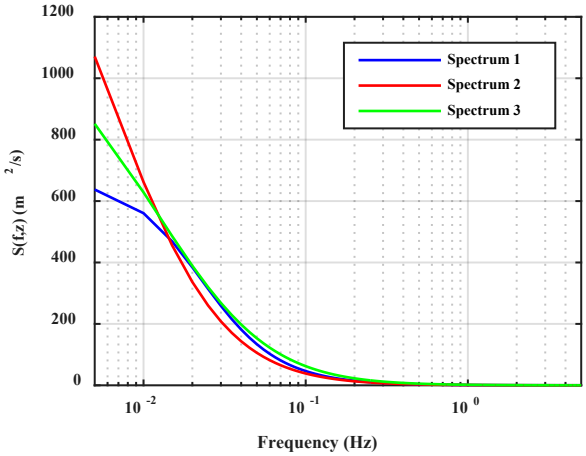

Figure 4.2 Comparison of wind spectra, at $z = r = 10$ m

To generate fluctuating wind speed time histories, the following inverse Fourier transform algorithm is used (Shinozuka & Deodatis, 1991):

$$V_f(z,t) = \sum_{n=1}^{N} \left(2\,S\left(f_n, z\right)\,\Delta f\right)^{0.5} \sin(2\pi f_n t - \phi_n) \tag{4-14}$$

where Δf is the frequency increment considered for analysis, f_n is the n^{th} frequency for which the spectrum is computed and is equal to $n \times \Delta f$, and ϕ_n is the phase angle for the n^{th} frequency. The phase angles are assumed to be randomly distributed between 0 and 2π. Because the fluctuating wind speeds, $V_f(z, t)$, will be fluctuating about the mean wind speed, $V_m(z)$, at each height, z, the mean of the fluctuating wind speeds should theoretically be zero. The mean value corresponds to the spectrum value for a frequency, f_n, equal to zero, however as seen in Figure 4.2, this is not true for the spectra considered. It has been recognized that the models assumed for the fluctuating wind speed spectra are not accurate for low frequencies (Simiu and Scanlan, 1996). To account for this inaccuracy and ensure mean values for the fluctuating wind speed time histories that are equal to zero, the summation in the formulation given above does *not* include the spectral value for $f_n = 0$ ($n = 0$).

Figure 4.3 shows the generated wind speed histories at $z = r = 10$ m for the three spectra of Figure 4.2. These time histories were generated for $\Delta f = 0.005$ Hz and $N = 1000$ resulting in a peak frequency $f_N = N \times \Delta f = 5$ Hz. In accordance with the Nyquist sampling theorems, in generating these time histories the following conditions were applied:

$$\Delta t \le \frac{1}{2N\Delta f} \quad \text{and} \quad T_{\max} \ge \frac{1}{\Delta f} \tag{4-15}$$

Thus, from the values of Δf and N chosen, $\Delta t = 0.10$ seconds and $T_{max} = 200$ seconds in Figure 4.3.

Figure 4.4 compares the analytical spectra with spectra back-calculated by the generated wind speed time histories. All of the generated wind speed histories have frequency content very similar to the spectra from which they are generated. For *Spectra 1* and *2*, the standard deviation of the generated wind speed history is within 5% of the standard deviation calculated as the input to the spectra.

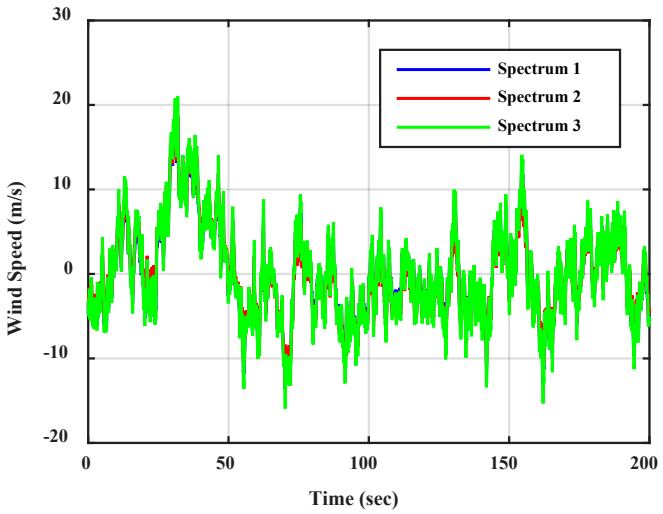

Figure 4.3 Generated fluctuating wind speed time histories, at $z = r = 10$ m

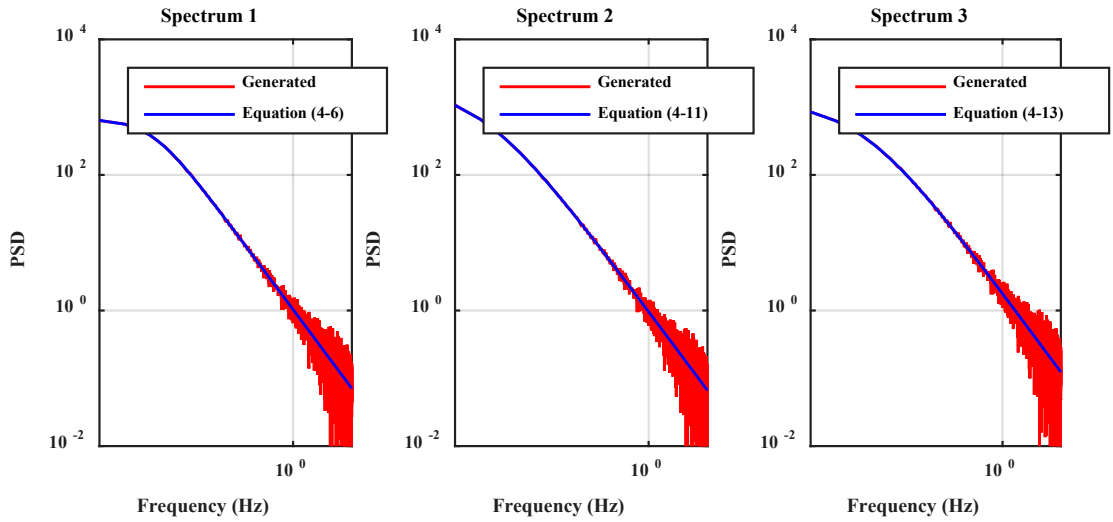

Figure 4.4 Comparison of analytical spectra vs. spectra back-calculated from the generated wind speed histories, at $z = r = 10$ m

These generated wind speed time histories were then compared to the wind speed time history generated using the NatHaz Online Wind Simulator (NOWS). NOWS generates wind speed histories based on a three-second gust wind speed and uses *Spectrum 3* to generate the wind speed histories. Using a gust wind speed which corresponds to a mean wind speed, V_r, of 10 m/s at $r = 10$ m as the input to the NatHaz simulator, a wind speed history is generated which has a standard deviation of 2.86 m/s. This is significantly less than the standard deviation calculated above (5.38 m/s). NOWS also asks for the ASCE 7-10 Exposure Category as an input which determines various parameter values which is used to calculate design wind speeds and loads. ASCE 7-10 assumes surface roughness lengths, z_o, that are significantly lower than values given in other sources. Specifically, for urban areas, ASCE 7-10 suggests a value of z_o of 0.30 meters, which would predict much lower standard deviations of fluctuating wind speeds.

Using the standard deviation, σ_v, computed from the NOWS wind speed time history as an input to the equations for *Spectra 1* and *2*, fluctuating wind speed time histories were generated and compared to the NOWS fluctuating wind speed time history in Figure 4.5. Additionally, *Spectrum 3* was also compared to the NOWS data by back calculating the surface

roughness length, z_o, based on the standard deviation of the NOWS data. A surface roughness length of 0.42 m was calculated which gives a friction velocity of 1.26 m/s and a standard deviation of 2.86 m/s (the computed standard deviation of the NatHaz fluctuating wind speed time history). *Spectrum 3* is also shown in Figure 4.5. A comparison between the wind speed power spectra back-calculated from the generated time histories are compared in Figure 4.6 with the spectrum of the NOWS fluctuating wind speed time history. This comparison shows that when using similar input, the method presented here generates similar fluctuating wind speed time histories as NOWS.

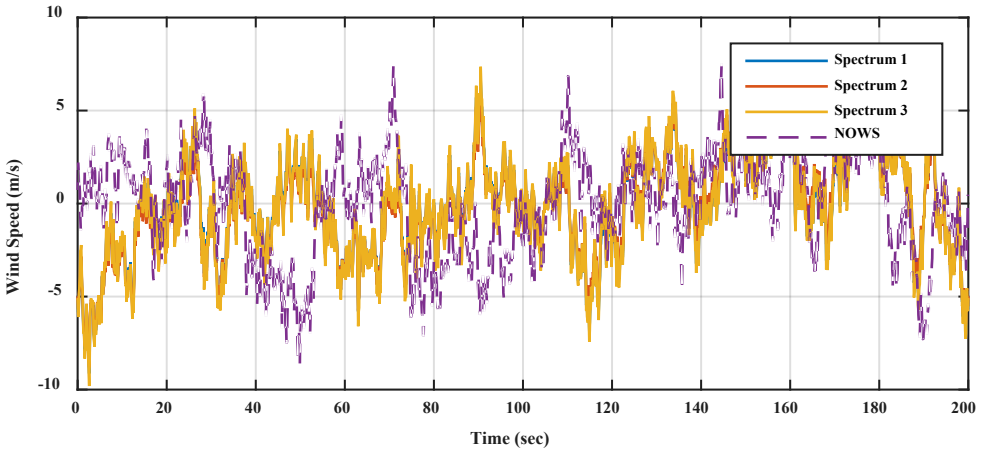

Figure 4.5 Comparison of generated fluctuating wind speed histories with NOWS data

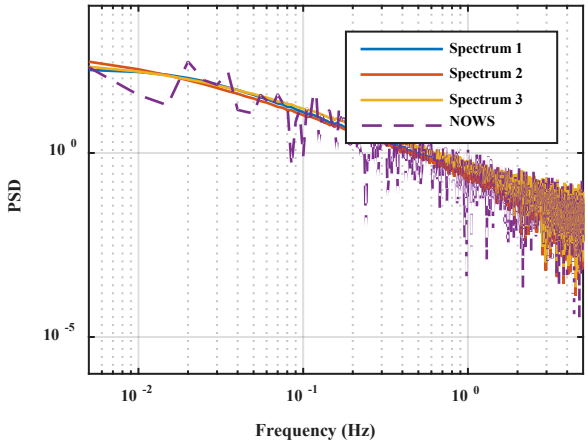

Figure 4.6 Comparison of spectra of generated fluctuating wind speed histories and NOWS data.

4.2.3. Spatial Correlation of Wind Speed Time Histories via Application to an Example Building

In this section, wind speed histories were generated along the entire height of a benchmark building. The example building used was similar to the one by Ni et al. (2011). This building is 42×42 m^2 in plan view, and has 76 stories, each of which is 4 m tall. Fluctuating wind speed time histories were generated using *Spectrum 3* and inverse Fourier transform algorithm described previously. *Spectrum 3* was chosen because of uncertainties regarding the applicability of the equations used to calculate the turbulence lengths scale, *L(z)*, used in *Spectra 1* and *2*. When Eq. (4-14) is used to convert the fluctuating wind speed power spectrum (at each height) to a fluctuating wind speed time history (at each height), different sets of phase angles are randomly generated at each height in order to generate *unique* fluctuating wind speed histories at each height. However, wind speeds are actually *spatially correlated*, since wind speeds at closely spaced locations are not expected to be significantly different.

Assuming a mean wind speed, V_r, of 10 m/s at a reference height, r, of 10 m and a surface roughness length, z_0, of 2 meters, the total wind speed histories at each height are shown in Figure 4.7. Figure 4.8 shows the wind speed time histories at stories 10 to 15, so that the relation between wind speeds at adjacent various heights is more evident.

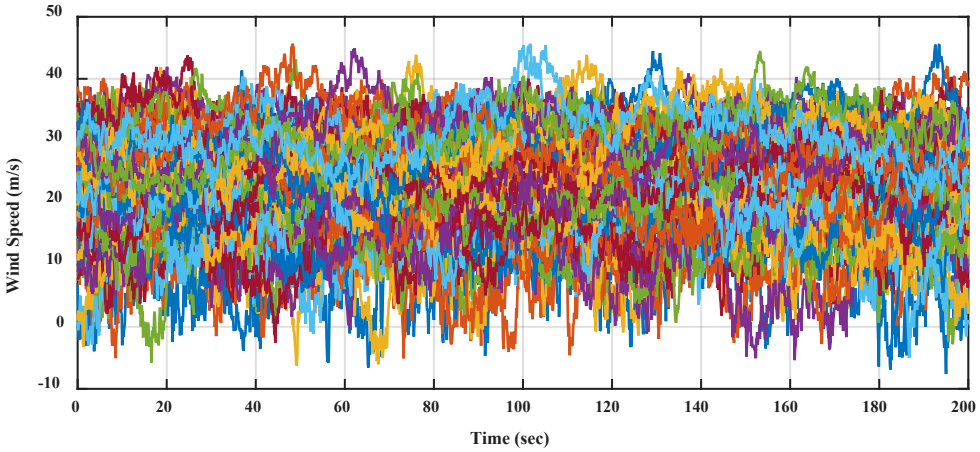

Figure 4.7 Wind Speed histories at each story of the example structure

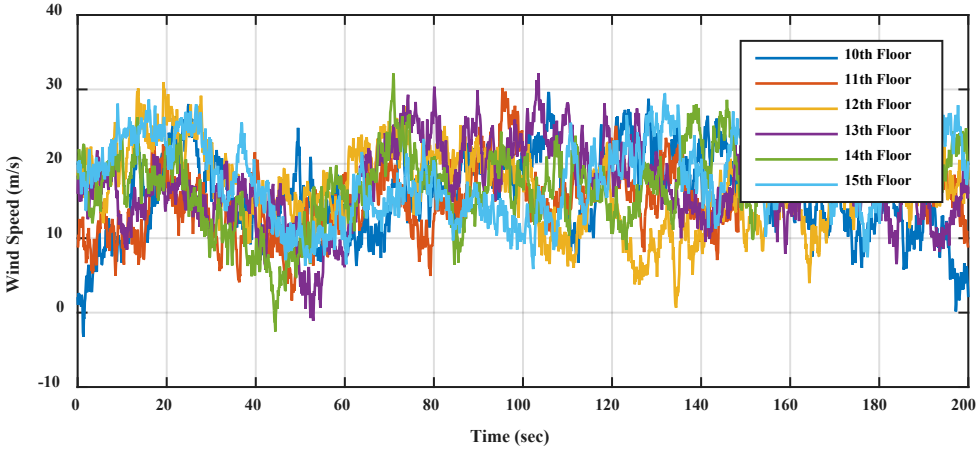

Figure 4.8 Wind Speed histories for stories 10 through 15 of the example structure

Near the 100 second of the time series shown in Figure 4.8, the wind speed at story 15 is about 20 m/s less than the wind speed at story 13 which is 8 meters below story 15. Similar discrepancies can be seen at other time instances in Figure 4.8. These discrepancies are a result of the randomly generated phase angles producing wind speed histories that are spatially uncorrelated.

To produce spatial correlation of the wind speed time histories over the height, a spatial moving average of the wind speeds over the height of the building is applied at each time instant. Moving average algorithms are often used in signal processing to eliminate noise in the recorded signal. In the present study, a *corrected* fluctuating wind speed (spatial) profile at each time

instant is determined using a moving average that moves spatially along the height of the building. The correction is only applied to the fluctuating component of the wind speeds. The corrected fluctuating wind speeds, $V_f^*(z,t)$, are determined from the following equation:

$$V_f^*(z_i,t) = \frac{\sum_{j=1}^{N_s} w_{ij} V_f(z_j,t)}{\sum_{j=1}^{N_s} w_{ij}} \tag{4-16}$$

where i represents the story for which the wind speeds are being corrected for and N_s is the number stories considered in the analysis. Two weight functions, w_{ij}, were considered. The first function was the exponential function from Liang et al. (2011) given below:

$$w_{ij} = \begin{Bmatrix} 0 \; for \; z_j < z_i - 0.5h_w \\ e^{-\left(\frac{|z_i - z_j|}{h_w \sigma_w}\right)^2} \; for \; z_i - 0.5h_w \le z_j \le z_i + 0.5h_w \\ 0 \; for \; z_j > z_i + 0.5h_w \end{Bmatrix} \tag{4-17}$$

where h_w is the height span over which the wind speeds are averaged, and σ_w is the weighting factor. The second weighting function, w_{ij}, considered was a rectangular function given as:

$$w_{ij} = \begin{cases} 0 \; , for \; z_j < z_i - 0.5h_w \\ 1 \; , for \; z_i - 0.5h_w \le z_j \le z_i + 0.5h_w \\ 0 \; , for \; z_j > z_i + 0.5h_w \end{cases} \tag{4-18}$$

When using the exponential weighting function, the value of σ_w can be as high as 5.56 (Liang et al, 2002). Assuming $\sigma_w = 5$ and $h_w = 42$ m (the width of the example building), the two weighting functions are shown below in Figure 4.9. As shown in this figure, for the selected value of σ_w, the two functions provide very similar weights. For this reason, the rectangular weighing function will only be used herein to maintain simplicity and eliminate the need to calibrate the weighting factor, σ_w.

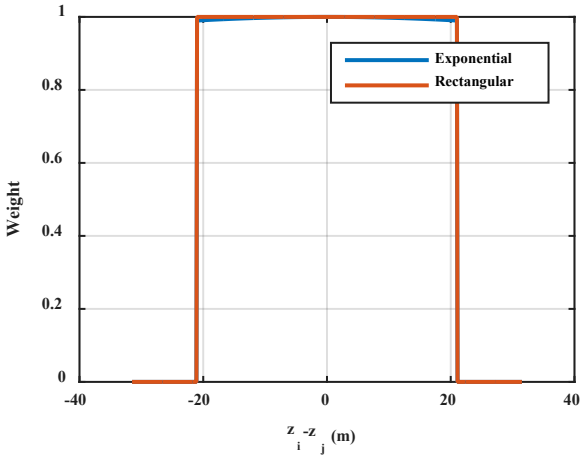

Figure 4.9 Weighting functions

The weighting functions given above are not valid for the entire height of the building. Near the bottom and top of the building under consideration, the span over which averaging can take place is less than h_w. One way to account for this is to simply use only the data points available when taking the average. This will generate distortions in the time histories near the bottom and top of the building. In some cases, such as correcting force time histories, this can be have a significant impact since corrected force histories near the bottom of the building will be higher than expected because of the increased influence of the wind force histories above it; similarly, the wind force histories near the top of the building will be lower than expected because of the increased influence of the wind force histories below it. Another method is to expand the range of data points at the bottom and top of the building, which eliminates the end distortions. For this study, a third method is used which corrects the fluctuating wind speeds and wind forces near the bottom and top of building by modifying the span over which the averaging takes place. This method is simpler to implement than expanding the span over which the averaging takes place, however it is potentially less robust. The span was modified to include an equal number of data points above and below the data point for which the average is computed based on the physical constraints of the building. For example, at story i=1, where i is the story

for which the average is being computed, only floor i is used for averaging. For i=2, stories i=1 through i=3 were used for averaging. Similarly, at story i=N, where N is the top story, only story N was used for averaging, and at story i=N-1, story i=N-2 through i=N were used for averaging. This modification was done until there were enough data points above and below story under consideration so that the averaging span is equal to h_w.

Upon first using this spatial moving average algorithm (at each time instant), it was observed that the temporal fluctuations in the wind speeds were getting filtered out; in other words, the temporal standard deviation of the corrected wind speed histories (at each selected height) were smaller than those of the originally generated wind speed time histories. A second step in the correction algorithm was then used to additionally "enforce" the correct standard deviation. This was done by a second correction to the fluctuating wind speed history at each height, z_i, obtained via the following expression:

$$V_f^{corr}(z_i,t) = V_f^*(z_i,t)\frac{\sigma_v(z_i)}{\sigma_v^*(z_i)}, \tag{4-19}$$

where σ_v and σ_v^* are the standard deviations of the original fluctuating wind speed time history, $V_f(z,t)$, and the fluctuating wind speed time history, $V_f^*(z,t)$, after the first correction, respectively, at height z_i.

Another observation of the weighting algorithm was that, as h_w increased, the spatial correlation between wind speeds of different heights increased. Also, when h_w approached the height of the building, the fluctuating wind speed histories became nearly identical. A value of h_w between B and $2B$, where B is the width of the building, gives reasonable correlation while maintaining some "randomness" in the fluctuating wind speed histories along the height of the building.

The final corrected wind speed history can then be obtained similarly to how the original wind speed history was obtained, i.e.

$$V(z,t) = V_m(z) + V_f^{corr}(z,t) \tag{4-20}$$

Using values of h_w = 42 m (the width of the building, B), the corrected wind speed histories at stories 10-15 are shown below in Figure 4.10. Figure 4.11 shows the frequency content of the corrected time series for story 15 compared to the spectrum predicted form the equation. These two plots show we have created correlation between wind speed histories at each floor and maintained the expected frequency content fairly well.

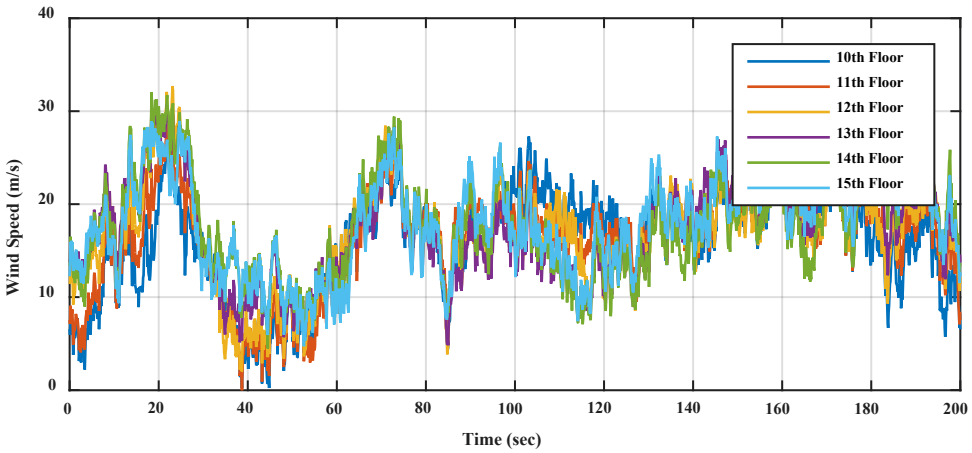

Figure 4.10 Corrected wind speed histories for stories 10-15 of the example structure

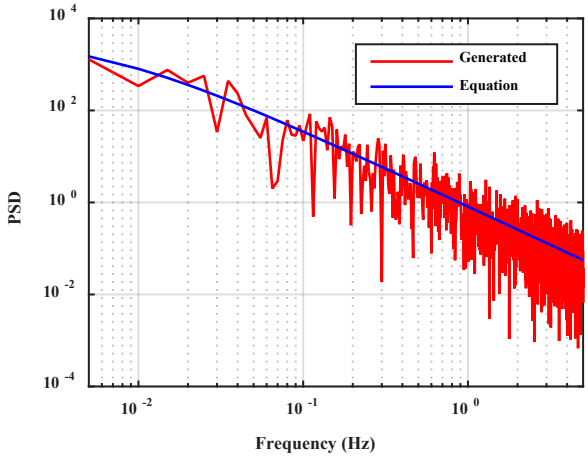

Figure 4.11 Comparison of corrected wind speed spectrum and the spectrum from equation

4.3. Along-wind Force Time Histories

Once the wind speed histories have been generated for each desired height, the along-wind force history at each height, $F_a(z,t)$, can be determined using the following equation (Holmes, 2015; Simiu, 2011; Simiu and Scanlan, 1996):

$$F_a(z,t) = 0.5\rho V(z,t)^2 C_d B H_f H_{hs}(V(z,t)) \tag{4-21}$$

where ρ is the air density, $V(z, t)$ is the total wind speed history after corrections, C_d is the drag coefficient, B is the width of the building, and H_f is the tributary height over which the wind force is acting. The Heaviside step function, $H_{hs}(V(z,t))$, is applied here to ensure that the force acting on the building will be set equal to zero if the wind speed at a particular time instant is negative, i.e. moving away from the building. Holmes (2015) gives estimates of C_d based on the side ratio, D/B, and aspect ratio, $H/\sqrt{(DB)}$ as shown below in Figure 4.12. For the example building considered here, the side ratio and aspect ratio are 1 and 7.2, respectively. From Figure 4.12, we can estimate that the drag coefficient for this building is about 1.6. Figure 4.13 and Figure 4.14 show sample force histories for the example building.

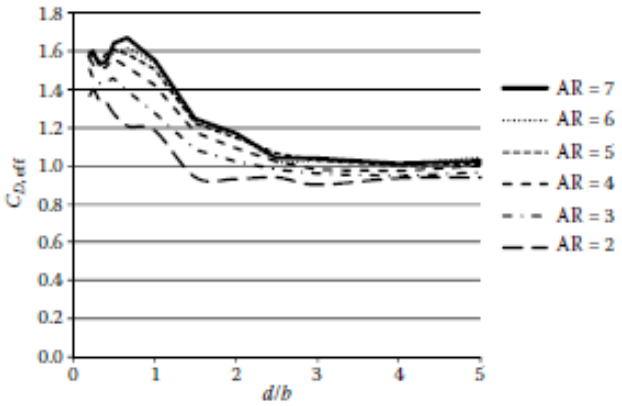

Figure 4.12 Effective drag coefficients, C_d, for rectangular buildings (Holmes, 2015)

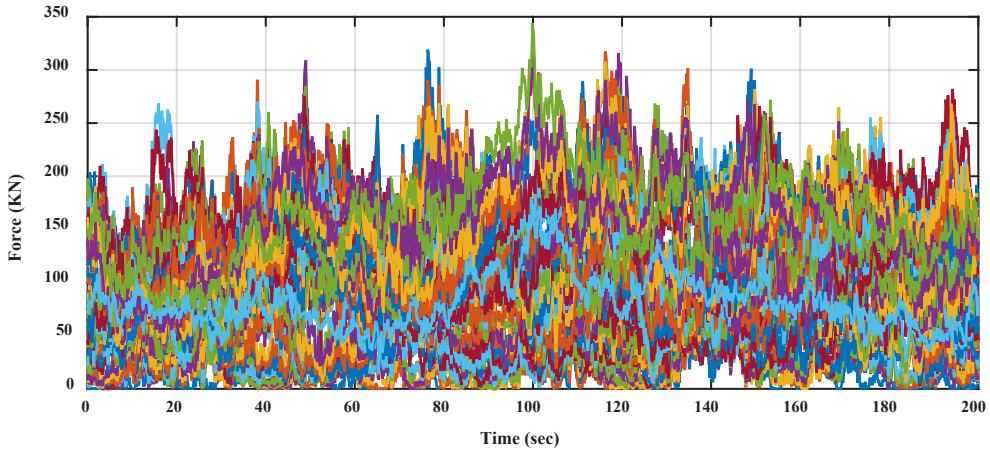

Figure 4.13 Along-wind force history for the example structure

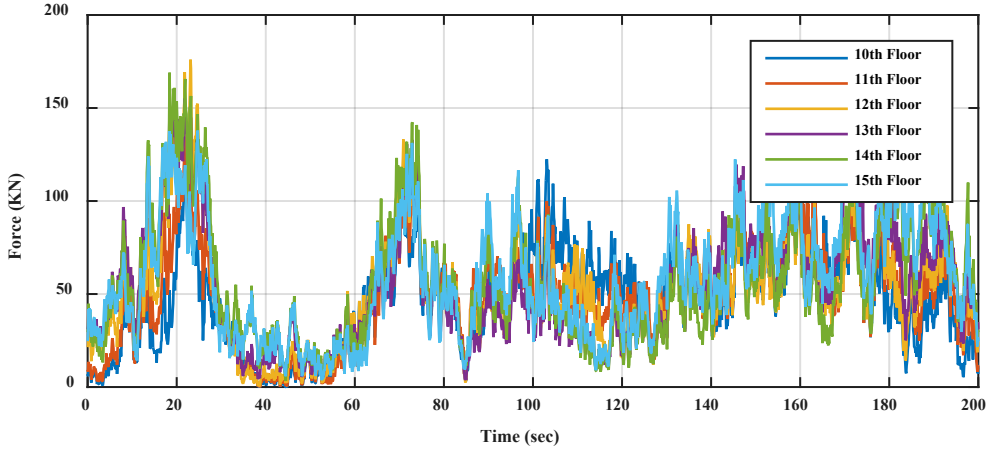

Figure 4.14 Along-wind force history for stories 10-15 of the example structure

4.4. Across-wind Force Time Histories

In addition to along-wind forces, the response of the building subject to across-wind forces will be investigated. Across-wind forces are forces that act perpendicular to the direction of the wind due to alternating vortices formed on either side of the building as the air moves around the structure. These forces act in a nearly sinusoidal fashion dominated by the vortex shedding frequency, f_s. The across-wind forces acting on the building will be calculated by converting the across-wind force power spectra proposed by Liang et al. (2002) to the time

domain using a similar approach described previously for the fluctuating wind speed power spectra.

The across-wind force spectra, $S_{fc}(f,z)$, at height z is given below:

$$S_{fc}(f,z)=\sigma_{fc}(z)^2\left[\begin{array}{c} A\dfrac{H(C_1)\dfrac{f}{f_s(z)^2}}{\left(1-\left(\dfrac{f}{f_s(z)}\right)^2\right)^2+C_1\left(\dfrac{f}{f_s(z)}\right)^2}+\ldots \\ \ldots+(1-A)\dfrac{C_2\dfrac{f^2}{f_s(z)^3}}{1.56\left[\left(1-\left(\dfrac{f}{f_s(z)}\right)^2\right)^2+C_2\left(\dfrac{f}{f_s(z)}\right)^2\right]} \end{array}\right] \tag{4-22}$$

where equations for $H(C_1)$, C_1, and C_2 are given as:

$$H(C_1)=0.179C_1+0.65\sqrt{C_1} \tag{4-23}$$

$$C_1=\left[0.47\left(D/B\right)^{2.8}-0.52\left(D/B\right)^{1.4}+0.24\right]\Big/\left(H/\sqrt{S}\right) \tag{4-24}$$

$$C_2=2 \tag{4-25}$$

In the three equations above, B is the width of the building perpendicular to the direction of the wind, D is the width of the building parallel to the direction of the wind, H is the height of the building, and $S = B \times D$. For $¼ \le D/B < ½$, A is given as:

$$A=\left(H/\sqrt{S}\right)\left[-0.6\left(D/B\right)^2+0.29\left(D/B\right)-.06\right]+\left[9.84\left(D/B\right)^2-5.86\left(D/B\right)+1.25\right] \tag{4-26}$$

For $½ \le D/B < 3$, A is given as:

$$A=\left(H/\sqrt{S}\right)\left[-0.118\left(D/B\right)^2+0.358\left(D/B\right)-.214\right]+\left[0.066\left(D/B\right)^2-0.26\left(D/B\right)+0.894\right] \tag{4-27}$$

The standard deviation of across-wind force at height z, $\sigma_{fc}(z)$ is given as:

$$\sigma_{fc}(z) = 0.5\rho V_m(z)^2 C_L B H_f \tag{4-28}$$

where $V_m(z)$, B, and H_f have been defined earlier, during the estimation of the along-wind forces. The RMS lift coefficient, C_L, is a given in Liang et al. (2002) and is an increasing function of the side ratio given below:

$$C_L = 0.045\left(D/B\right)^3 - 0.335\left(D/B\right)^2 + 0.868\left(D/B\right) - 0.174 \tag{4-29}$$

The vortex shedding frequency, f_s, is a function of the Strouhal number, S_t, as given as:

$$f_s(z) = \frac{S_t V_m(z)}{B} \tag{4-30}$$

The Strouhal number is dependent on the building shape and is given as 0.12 for square buildings in Holmes (2015). Alternatively, S_t can be calculated from the empirical equation given by Liang et al. (2002) as shown below:

$$S_t = \begin{cases} 0.094, & 1/4 \le D/B \le 1/2 \\ 0.002\left(\dfrac{D}{B}\right)^2 - 0.023\left(\dfrac{D}{B}\right) + 0.105, & 1/2 < D/B \le 4 \end{cases} \tag{4-31}$$

For the example building considered here, this empirical relation gives S_t to be 0.084.

Due to the oscillating (or sinusoidal) nature of across-wind forces, they have the potential to cause a larger dynamic response in buildings than along-wind forces. This is particularly true for tall slender buildings which have relatively low natural frequencies that could be near the vortex shedding frequency, f_s, depending on how fast the mean wind speed is and the natural frequency of the structure. Furthermore, Liang et al. (2002) found that across-wind forces are most intense for buildings with square plan dimensions.

Using the same example building and reference mean wind speed as the along-wind forces in the previous section, the across-wind force spectra were generated for each story and

are given in Figure 4.15 and Figure 4.16. Eq. (4-31) was used to calculate S_t. These figures illustrate the pronounced peak of the spectra at the vortex shedding frequency. For the reference wind speed and building width considered here, the vortex shedding frequency for story 15 is 0.036 Hz which corresponds to the location of the spectrum peak in Figure 4.16.

Figure 4.17 through Figure 4.19 show the generated across-wind force histories for this example building. The rectangular weighting function described previously was used to provide spatial correlation between the across-wind forces along the height of the building. In this case, the height of the moving average, h_w, was assumed to equal to 42 m (the width of the building). These figures show the sinusoidal nature of the across-wind forces. It is also interesting to note that the weighting function seems to have less impact on the generated across-wind force histories than it did for the fluctuating wind speed histories. Figure 4.20 shows the frequency content of the generated across-force time history for story 15 compared to the spectrum predicted by Eq. (4-22). This figure further validates the method used for converting from frequency domain to time domain.

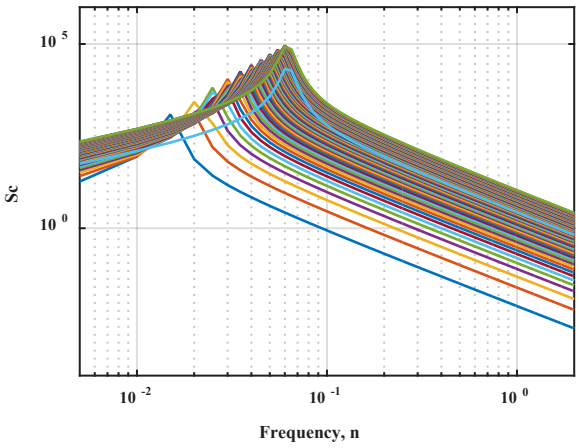

Figure 4.15 Across wind force spectra for example building

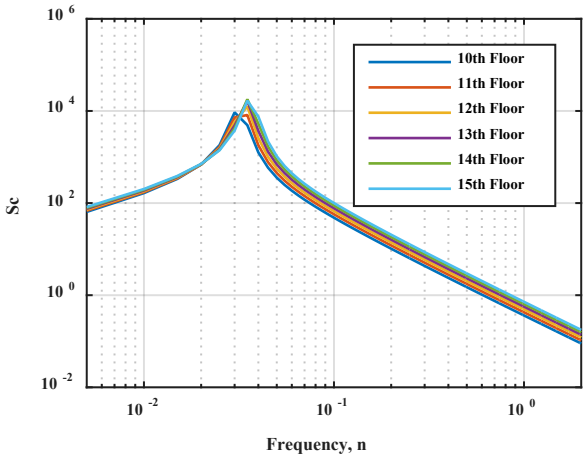

Figure 4.16 Across-force spectra for example building for stories 10-15

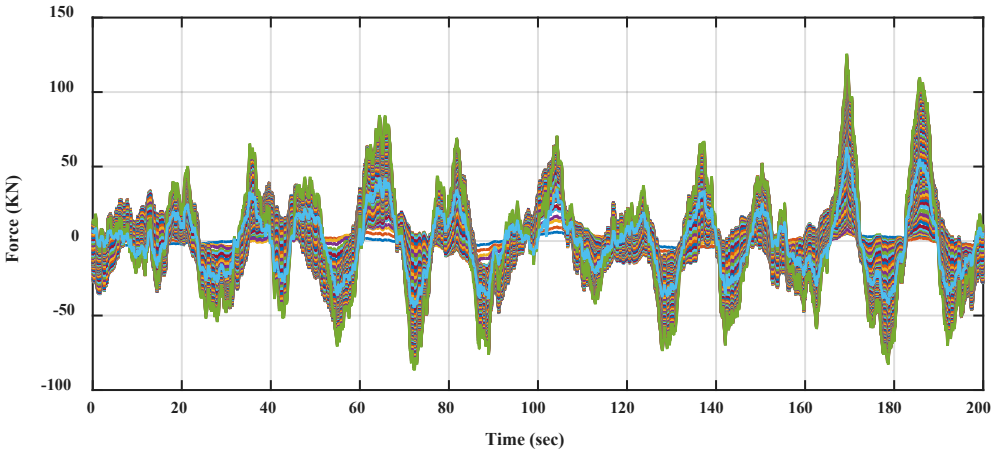

Figure 4.17 Across-wind forces for example building

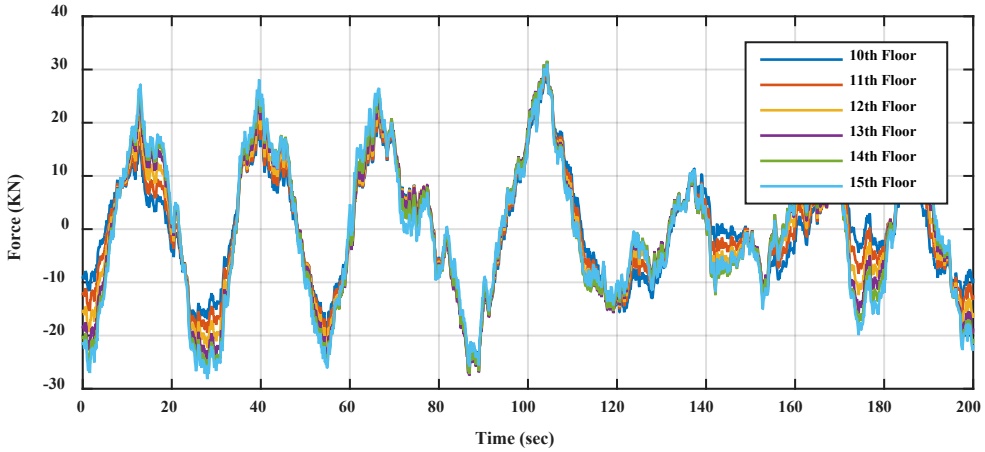

Figure 4.18 Original across-wind forces for stories 10-15 of example building

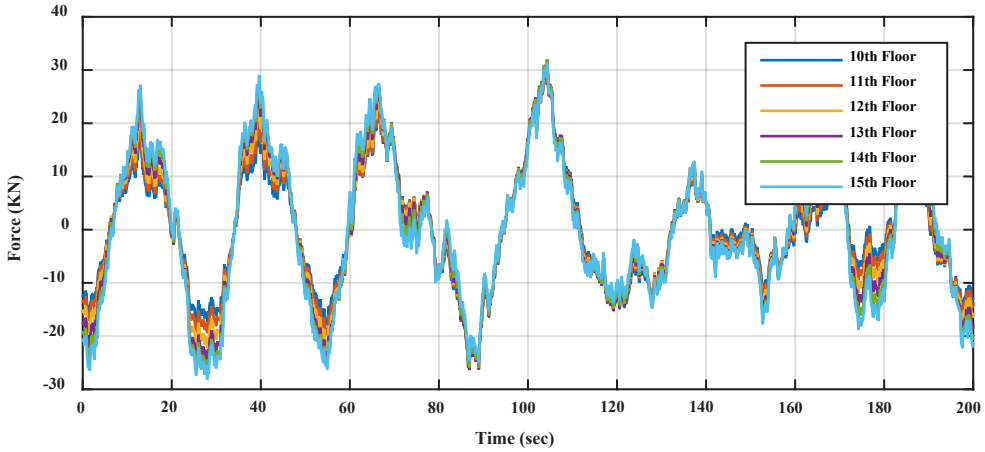

Figure 4.19 Corrected across-wind forces for stories 10-15 of example building

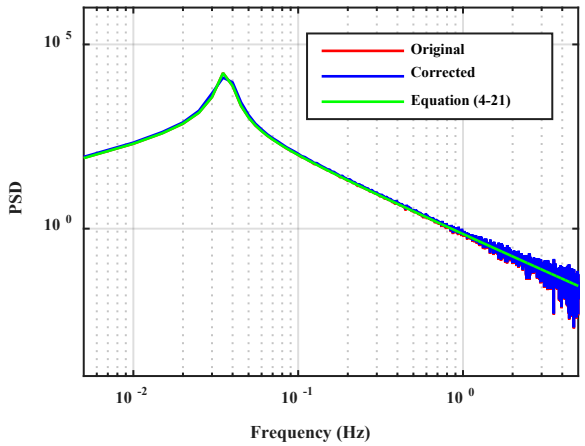

Figure 4.20 Comparison of original and corrected across-force spectrum and the spectrum from the Eq. (4-22)

4.5. Summary and Conclusions

This chapter presented a method of generating wind speed time histories along the entire height of a building. Along-wind forces were calculated from wind speed time histories considering mean and fluctuating components. The fluctuating component was first described in the frequency domain, and then was converted to a time history using an inverse Fourier transform algorithm. Similarly, the across-wind forces were first described by a spectral representation which was then converted to the time domain. In addition, a method of correlating the wind speeds and forces along the height of the building was developed which provided a

more realistic spatial distribution of wind forces. These wind force time histories will be used as the source of energy in the EH analyses discussed in the next chapter.

5. ENERGY HARVESTING AND SEISMIC ANALYSIS OF A MULTI DEGREE OF FREEDOM SYSTEM

5.1. Introduction and Objectives

To investigate the feasibility of implementing EH technology into the design of structures, the EH potential of tall buildings subjected to wind loading was analyzed and presented in this chapter. Several reference mean wind speeds and equivalent EM damping ratios are considered for the EH analysis and a comparison of the EH potential under along and across-wind forces is made. The damping ratio that maximizes harvested energy was also used for a seismic analysis of the building to determine if that damping ratio can also be used for VM. This chapter concludes with a discussion on the effectiveness of the EH dampers when used as energy harvesters and as VM devices.

5.2. Modeling of MDF System Equipped with EH Dampers

The example structure was a 76 story building with plan dimensions of 42 m by 42 m and story heights of 4 meters, giving a total building height of 304 m. For simplicity, the building was assumed to behave as a shear building with a total mass of 153,000 metric tons (1.53×10^8 kg) assumed to be distributed evenly among all degrees of freedom. The inter-story stiffness of each degree of freedom was chosen to give a first natural frequency of approximately 0.16 Hz (first natural period of 6.26 seconds) similar to the example structure used in Ni et al. (2011). The stiffness was assumed to be the same in both directions. To account for the potential nonlinear response of the building, an elastoplastic force displacement relationship was assumed with yielding occurring at inter-story drift ratios of 1% for each floor. For the damping inherent in the structure, Rayleigh damping was assumed with a damping ratio of 1% in the 1^{st} and $N^{th}/2$ modes

where N is the number of degrees of freedom considered in the analysis. To decrease computational time, the 76 story was analyzed as a 38 degree of freedom system with each degree of freedom representing two stories of the example building. *Thus, the terms "story" and "inter-story" for the text to follow will always refer to two adjacent stories*. Figure 5.1 shows the modal periods and damping ratios for this example structure.

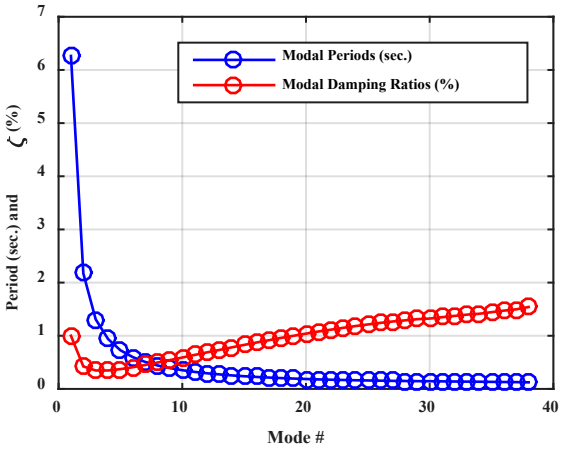

Figure 5.1 Modal periods and damping ratios for example structure

The simplified model for the EH damper proposed in Chapter 3 was used in the analysis of this MDF system. The EH damper from Chapter 3 is a prototype and needs to be scaled up for use in a structure. In this study, the scaling was determined based on an equivalent viscous damping coefficient required to achieve a desired damping ratio provided by the EH damper. An equivalent viscous damping ratio was assumed for the first mode and the damping was assumed to be proportional to the stiffness at each degree of freedom, i.e.

$$c_{eq,n} = a_1 k_n \tag{5-1}$$

where $c_{eq,n}$ and k_n are the equivalent viscous damping coefficient and lateral inter-story stiffness at the story between the n-th and (n-1)-th degree of freedom. From modal analysis, for the first mode:

$$a_1 = \frac{2\zeta_{eq}}{\omega_1} \tag{5-2}$$

where ζ_{eq} is the equivalent damping ratio provided to the first mode by the EH dampers distributed over the building height such that they satisfy Eq. (5-1), and ω_1 is the natural circular frequency of the first mode of vibration. The equivalent viscous damping ratio from Eq. (5-1) is the sum of the EM damping that generates electricity, c_{EM}, and the damping in the EM motor due to losses c_{ml}. The factor that is used to scale the model parameters at each story, $S_{EM,n}$, is then

$$S_{EM,n} = \frac{c_{eq,n}}{c^*_{EM} + c^*_{ml}} \tag{5-3}$$

where c_{ml}^* is the calibrated parameter value from Table 3.1 (382 N-s/m) and c^*_{EM} is computed from Eq. (3-2). It should be noted that the value of S_{EM} calculated using Eq. (5-3) for each story includes the total effect of all EH dampers at that story. In other words, the scale factor for an individual EH damper at a given story is computed by the taking $S_{EM,n}$ from Eq. (5-3) and dividing it by the number of EH dampers at that story.

Although a detailed cost-benefit analysis is outside of the scope of this feasibility study, S_{EM} can be viewed as a rough estimate of the relative cost of the EH dampers. With this in mind, it would be beneficial to minimize this value. In order to accomplish this, the highest value of c_{EM} predicted by Eq. (3-2) was used to determine S_{EM}. As explained by Cassidy et al. (2011), this maximum value of c_{EM} corresponds to a value of R_L equal to zero and c_{EM} in this case is given by

$$c_{EM} = \frac{9K_e^2}{4l^2R} \tag{5-4}$$

where K_e, l, and R are given in Chapter 3. It should be noted that the value of R_L in Eq. (3-2) can theoretically be varied to achieve a range of damping ratios provided by a single EH damper. Therefore, by assuming R_L is equal to zero, when scaling the model parameters, we are limiting

the range of damping ratios provided by the device. This would be a significant constraint in cases of semi-active damping systems where the damping is altered based on the loading conditions to optimize the damping objective for that loading condition, i.e. EH versus VM.

The calibrated model parameters were assumed to increase proportionally based on S_{EM} calculated from Eq. (5-3) for an assumed damping ratio. The lead screw and the EM motor are separate elements and are interchangeable. Therefore, it is assumed that the EH device can be designed to minimize the friction associated with the ball bearings. With this assumption, the force and stiffness parameters associated with the bearing friction were scaled by half of S_{EM} calculated from Eq. (5-3). The phase angles, ϕ_1 and ϕ_2, were not scaled because they are unitless and are assumed to be unaffected by the size of the EH damper.

For each wind load case and wind speed considered (described later), analyses were run for equivalent damping ratios of 5, 10, 15, 20, 25, 30, 35, and 40% provided by the EH damper. Table 5.1 shows the structure stiffness and EM damping properties for the analyses that follow.

Table 5.1. Inter-story Stiffness and EM Damping Properties of Example Building

		ζ_{eq} = 5%		ζ_{eq} = 10%		ζ_{eq} = 15%		ζ_{eq} = 20%	
Story	**Stiffness (KN/m)**	c_{eq} **(KN-s/m)**	S_{EM}	c_{eq} **(KN-s/m)**	S_{EM}	c_{eq} **(KN-s/m)**	S_{EM}	c_{eq} **(KN-s/m)**	S_{EM}
1-9	$2.64\text{x}10^6$	$2.63\text{x}10^5$	3,082	$5.26\text{x}10^5$	6,164	$7.89\text{x}10^5$	9,246	$1.05\text{x}10^6$	12,328
10-19	$2.40\text{x}10^6$	$2.39\text{x}10^5$	2,802	$4.78\text{x}10^5$	5,604	$7.18\text{x}10^5$	8,406	$9.57\text{x}10^5$	11,207
20-28	$2.16\text{x}10^6$	$2.15\text{x}10^5$	2,522	$4.31\text{x}10^5$	5,044	$6.46\text{x}10^5$	7,565	$8.61\text{x}10^5$	10,087
29-38	$1.92\text{x}10^6$	$1.91\text{x}10^5$	2,242	$3.83\text{x}10^5$	4,484	$5.74\text{x}10^5$	6,724	$7.65\text{x}10^5$	8,966

Table 5.1 Cont.

ζ_{eq} = 25%		ζ_{eq} = 30%		ζ_{eq} = 35%		ζ_{eq} = 40%	
c_{eq} (KN-s/m)	S_{EM}	c_{eq} (KN-s/m)	S_{EM}	c_{eq} (KN-s/m)	S_{EM}	c_{eq} (KN-s/m)	S_{EM}
1.32×10^6	15,410	1.58×10^6	18,492	1.84×10^6	21,574	2.11×10^6	24,656
1.20×10^6	14,009	1.43×10^6	16,811	1.67×10^6	19,613	1.91×10^6	22,415
1.08×10^6	12,608	1.29×10^6	15,130	1.51×10^6	17,652	1.72×10^6	20,173
9.57×10^5	11,207	1.15×10^6	13,449	1.34×10^6	15,690	1.53×10^6	17,932

5.3. Response to Along-Wind Forces

The wind force time histories in the along-wind direction were generated using the spectral approach described Chapter 4. Six reference wind speeds, V_r, were considered at a height, r, of 10 m above the ground: 2.5, 5, 10, 15, 20 and 25 m/s. The corresponding mean wind speed profiles, $V_m(z)$, are shown below in Figure 5.2. These mean wind speed profiles were generated using the power law from Eq. (4-5) with a Hellmann exponent of 0.33.

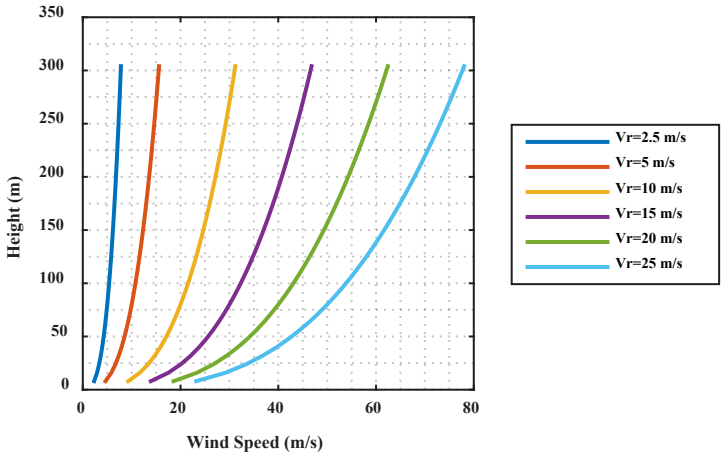

Figure 5.2 Mean wind speed profiles considered in the analysis

In the plots that follow, Figure 5.3, Figure 5.5, and Figure 5.7 show the along-wind force time histories at selected degrees of freedom for reference wind speeds of 2.5, 10, and 20 m/s, respectively. Figure 5.4, Figure 5.6, Figure 5.8 show the rate of energy harvesting generated

from the along-wind force histories shown in Figure 5.3, Figure 5.5, and Figure 5.7, respectively. The rate of energy harvesting, or EM power, P_{EM}, was estimated during steady state response by the slope of a linear line of best fit going through the final 250 seconds of the harvested energy time history. Table 5.2 summarizes the data for all wind speeds and equivalent damping ratios considered. The efficiency that is shown in Table 5.2 is the percentage of energy dissipated by the EH damper that was converted to electricity. The underlined values are the maximum EM power values for each reference wind speed.

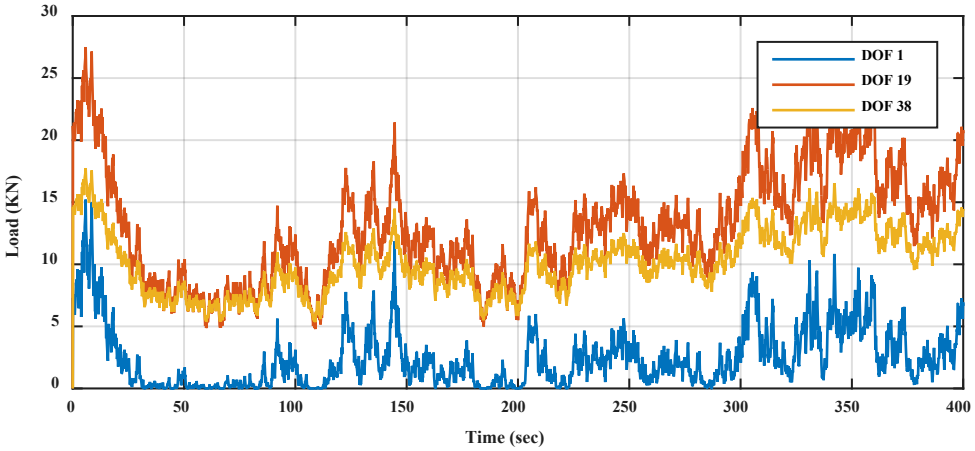

Figure 5.3 Along-wind force histories for V_r = 2.5 m/s

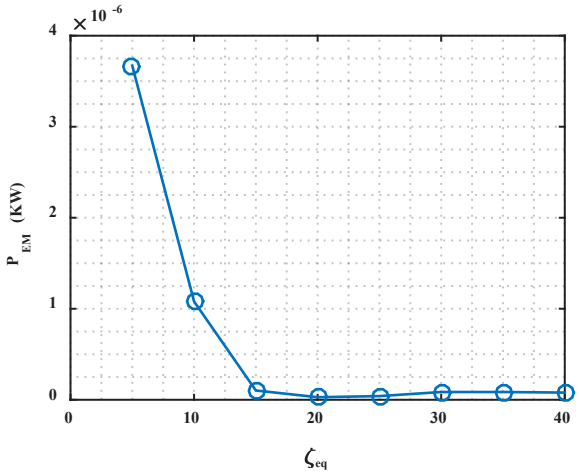

Figure 5.4 EM power for along-wind forces and V_r = 2.5 m/s

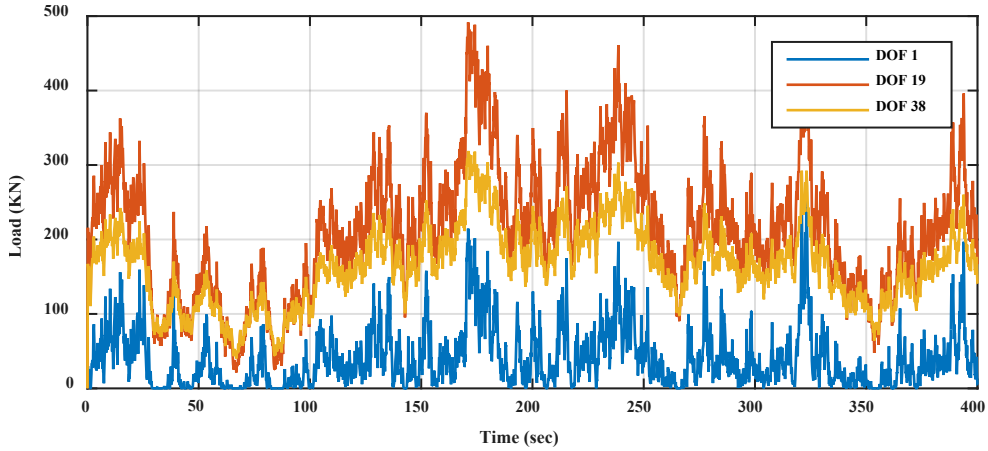

Figure 5.5 Along-wind force histories for V_r = 10 m/s

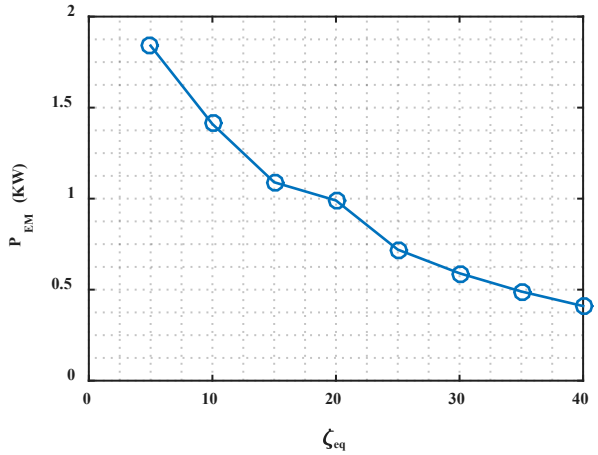

Figure 5.6 EM power for along-wind forces and V_r = 10 m/s

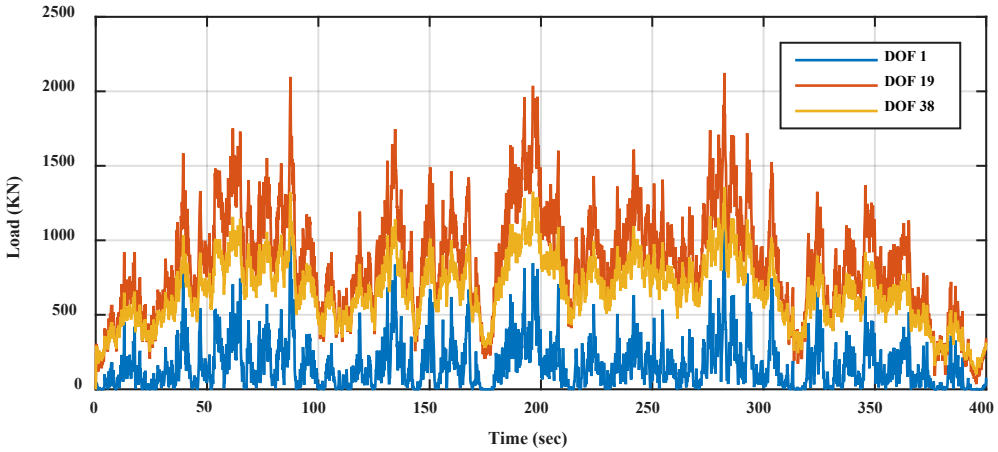

Figure 5.7 Along-wind force histories for V_r = 20 m/s

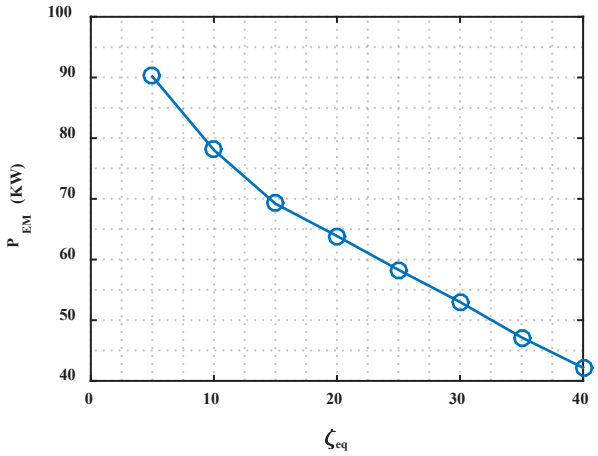

Figure 5.8 EM power for along-wind forces and V_r = 20 m/s

Table 5.2. Summary of Energy Harvesting from Along-Wind Response

	V_r = 2.5 m/s		V_r = 5 m/s		V_r = 10 m/s	
ζ_{eq}	P_{EM} (kW)	Eff. (%)	P_{EM} (kW)	Eff. (%)	P_{EM} (kW)	Eff. (%)
5%	$3.67\text{x}10^{-6}$	5.0%	$6.08\text{x}10^{-3}$	7.4%	1.84	31.3%
10%	$1.08\text{x}10^{-6}$	1.5%	$2.48\text{x}10^{-3}$	6.2%	1.41	25.6%
15%	$1.02\text{x}10^{-7}$	6.3%	$8.81\text{x}10^{-4}$	4.1%	1.09	23.7%
20%	$2.82\text{x}10^{-8}$	2.6%	$1.27\text{x}10^{-5}$	3.6%	0.88	22.8%
25%	$4.04\text{x}10^{-8}$	5.0%	$3.51\text{x}10^{-6}$	3.3%	0.72	22.0%
30%	$8.52\text{x}10^{-8}$	11.8%	$4.83\text{x}10^{-6}$	3.2%	0.59	21.1%
35%	$8.53\text{x}10^{-8}$	15.3%	$5.05\text{x}10^{-6}$	2.7%	0.49	20.1%
40%	$7.88\text{x}10^{-8}$	14.9%	$5.48\text{x}10^{-6}$	2.4%	0.41	19.1%

Table 5.2 Cont.

	V_r = 15 m/s		V_r = 20 m/s		V_r = 25 m/s	
ζ_{eq}	P_{EM} (kW)	Eff. (%)	P_{EM} (kW)	Eff. (%)	P_{EM} (kW)	Eff. (%)
5%	19.66	60.8%	90.17	76.0%	312.82	84.1%
10%	15.45	52.1%	78.05	78.0%	339.95	79.7%
15%	12.33	48.9%	69.20	64.1%	328.30	76.6%
20%	10.26	46.3%	63.88	60.6%	305.29	74.1%
25%	8.98	44.6%	58.30	57.5%	285.18	72.1%
30%	8.14	43.4%	53.00	54.7%	264.31	70.2%
35%	7.57	42.2%	47.17	52.1%	243.07	68.5%
40%	7.07	41.2%	42.65	49.6%	222.67	66.9%

For all wind speeds considered, except 25 m/s, the lowest damping ratio considered resulted in the highest EM power. For a reference wind speed of 25 m/s, a damping ratio of 10% resulted in the highest EM power. However, there was a difference in EM power of several orders of magnitude between reference wind speeds of 2.5 m/s and 25 m/s. With the exception of the lowest wind speed considered, the efficiency of the EH device increased with increasing wind speed and decreased with increasing equivalent damping ratio provided by the EH device. This implies that at smaller amplitudes, energy dissipation is dominated by friction losses in the EM dampers. As shown by Figure 5.4 and Table 5.2, there is very little energy generation for along-wind forces of low wind speeds. Reference wind speeds of 10 m/s and greater generated electricity at rates in the kilowatts and even in the hundreds of kilowatts for a reference wind speed of 25 m/s.

Table 5.3 summarizes the response of the building due the along-wind forces for each equivalent damping ratio and mean reference wind speed considered. This table illustrates the effectiveness of the EH dampers as a means of VM under wind loading. In Table 5.3, drift ratios equal to zero indicate that the inter-story drift for that reference wind speed and damping ratio were so small they can be considered negligible. The peak drift ratios are an indicator of the potential damage to the building under the wind loading. As expected for low wind speeds the inter-story drifts are very low and the drift ratios increased with increasing wind speed and decreased with increasing damping provided by the EH dampers. Considering the yield displacement was assumed to be 1%, Table 5.3 shows that no yielding occurred for any of the reference wind speeds considered.

The acceleration of the building is a measure of occupant discomfort, and because of this, building codes place limits on the acceleration due to service wind loads. Building accelerations

become *perceptible* to occupants between 0.5% and 1.5% of the acceleration of gravity, *g* (0.049 and 0.147 m/s^2), with accelerations greater than about 15% *g* (1.47 m/s^2) being considered *intolerable* by building occupants (Griffis, 1993). Furthermore, Griffis (1993) recommends that for buildings with a fundamental natural period between 4 and 10 seconds, as is the case for the example building, *acceptable* peak accelerations during a 10 year wind event are between 1.5% and 2.7% *g* (0.147 and 0.265 m/s^2). None of the combinations of wind speeds and damping ratios considered resulted in peak accelerations that would be considered intolerable, but reference wind speeds of 10 m/s and greater did result in perceptible peak accelerations and reference wind speeds of 20 and 25 m/s resulted in peak accelerations that exceed the acceptable recommended ranges presented by Griffis (1993). Similar to the peak inter-story drifts, the peak accelerations generally decreased, with increasing damping for all wind speeds. However for a reference wind speed of 25 m/s, the peak acceleration exceeded the limits recommended by Griffis (1993) for all damping ratios considered. These observations demonstrate the conflict between EH and VM requirements.

Table 5.3. Structure Response due to Along-Wind Forces

	V_r = 2.5 m/s		V_r = 5 m/s		V_r = 10 m/s	
ζ_{eq}	**Peak Drift Ratio**	**Peak acc. (m/s^2)**	**Peak Drift Ratio**	**Peak acc. (m/s^2)**	**Peak Drift Ratio**	**Peak acc. (m/s^2)**
5%	0.0303%	0.0062	0.0161%	0.0284	0.0899%	0.0894
10%	0.0009%	0.0029	0.0140%	0.0095	0.0861%	0.0884
15%	0.0000%	0.0013	0.0121%	0.0107	0.0825%	0.0759
20%	0.0000%	0.0011	0.0102%	0.0107	0.0799%	0.0586
25%	0.0000%	0.0010	0.0083%	0.0100	0.0766%	0.0618
30%	0.0000%	0.0011	0.0065%	0.0095	0.0734%	0.0523
35%	0.0000%	0.0013	0.0046%	0.0076	0.0705%	0.0500
40%	0.0000%	0.0014	0.0027%	0.0068	0.0676%	0.0374

Table 5.3 Cont.:

	V_r = 15 m/s		V_r = 20 m/s		V_r = 25 m/s	
ζ_{eq}	**Peak Drift Ratio**	**Peak acc. (m/s^2)**	**Peak Drift Ratio**	**Peak acc. (m/s^2)**	**Peak Drift Ratio**	**Peak acc. (m/s^2)**
5%	0.206%	0.265	0.360%	0.451	0.775%	0.744
10%	0.184%	0.257	0.329%	0.341	0.730%	0.525
15%	0.170%	0.253	0.320%	0.273	0.700%	0.449
20%	0.160%	0.247	0.314%	0.256	0.679%	0.400
25%	0.156%	0.240	0.309%	0.241	0.661%	0.399
30%	0.153%	0.236	0.305%	0.208	0.644%	0.395
35%	0.150%	0.231	0.301%	0.204	0.629%	0.389
40%	0.148%	0.224	0.298%	0.208	0.614%	0.383

5.4. Response to Across-Wind Forces

The same equivalent damping ratios and mean wind speed profiles as the along-wind forces were considered for the across-wind forces. Figure 5.9, Figure 5.11, Figure 5.13 show the across-wind force histories for select degrees of freedom for the across-wind forces resulting from reference wind speeds, V_r, of 2.5, 10, and 20 m/s, respectively. These figures show these forces have a stronger sinusoidal nature and are dominated by the vortex shedding frequency. Figure 5.10, Figure 5.12, and Figure 5.14 show the EM power for reference wind speeds of 2.5, 10, and 20 m/s, respectively. Table 5.4 summarizes the EH data for the across-wind forces for all reference wind speeds and damping ratios considered.

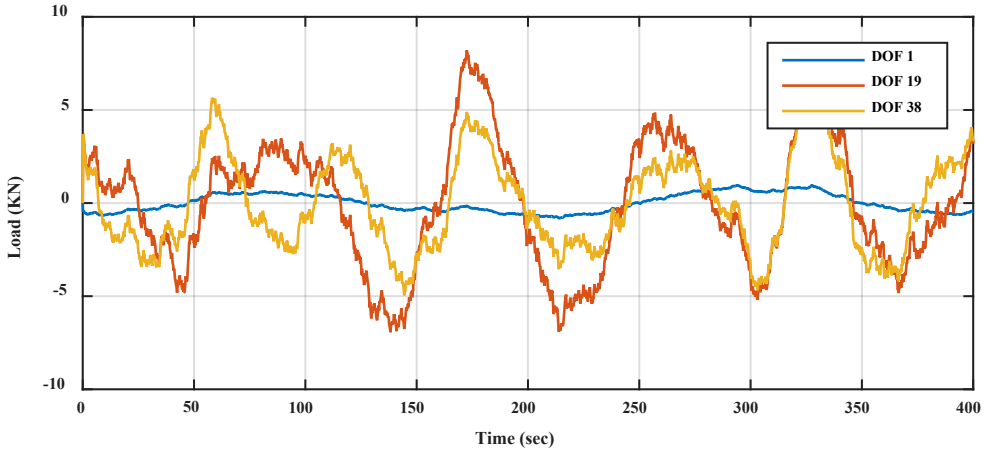

Figure 5.9 Across-wind force histories for V_r = 2.5 m/s

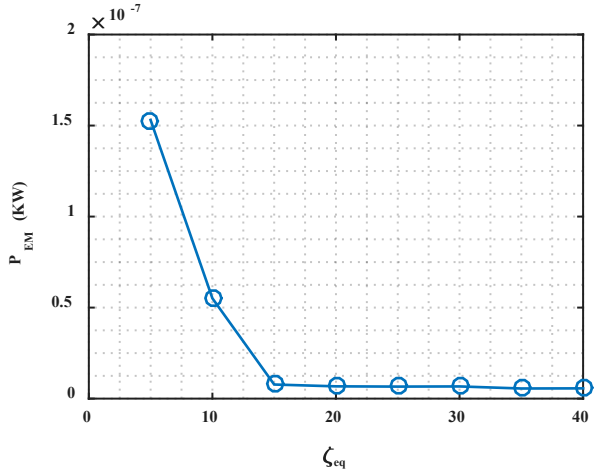

Figure 5.10 EM power for across-wind forces and V_r = 2.5 m/s

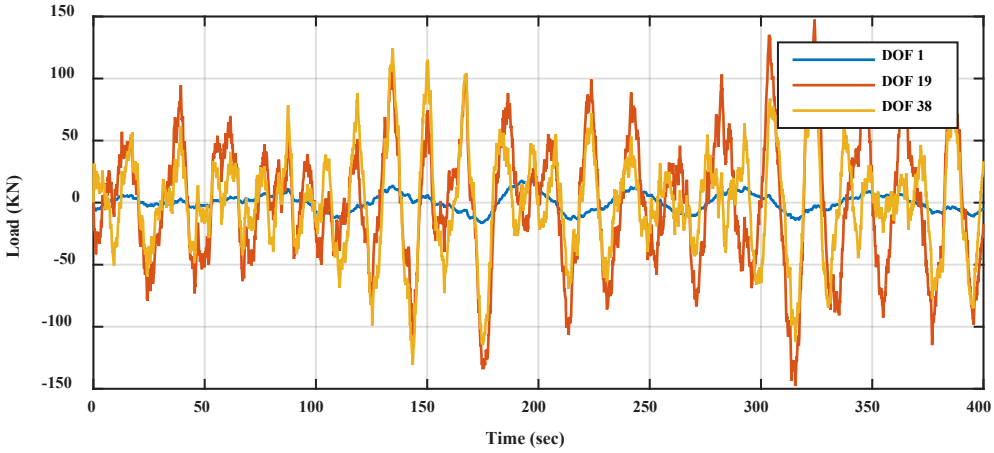

Figure 5.11 Across-wind force histories for V_r = 10 m/s

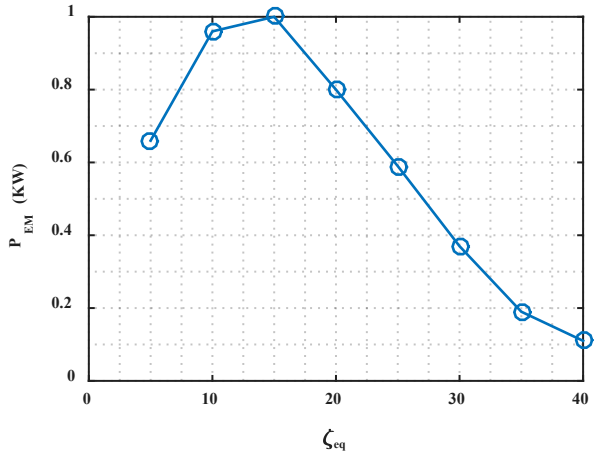

Figure 5.12 EM power for across-wind forces and V_r = 10 m/s

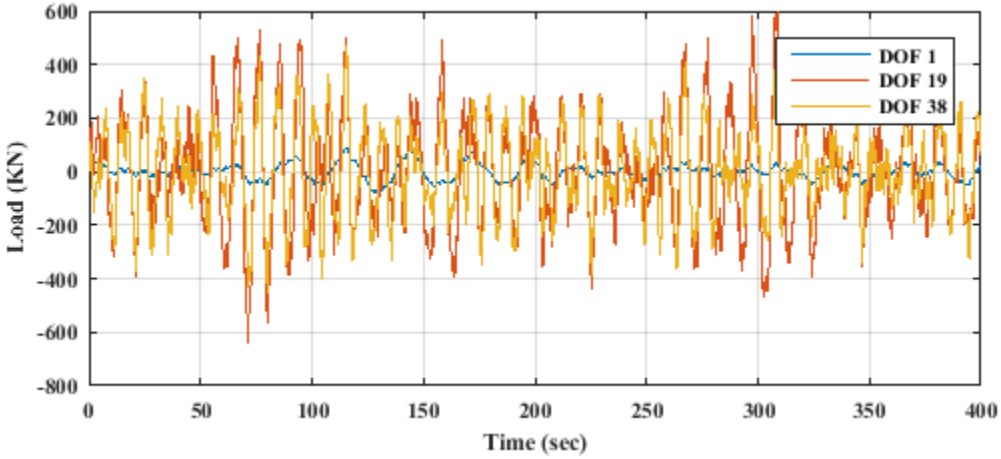

Figure 5.13 Across-wind force histories for V_r = 20 m/s

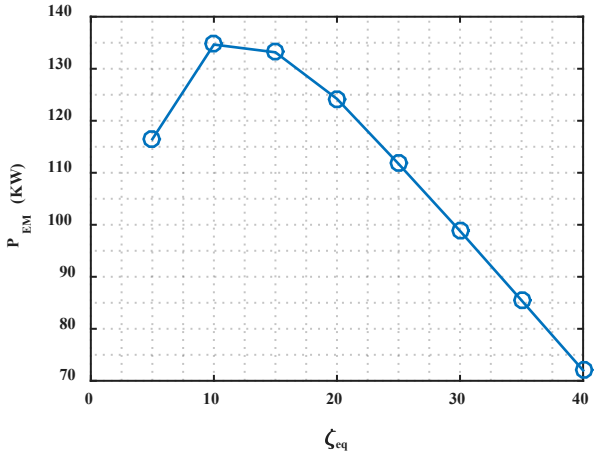

Figure 5.14 EM power for across-wind forces and V_r = 20 m/s

Table 5.4. Summary of Energy Harvesting from Across-Wind Response

	V_r = 2.5 m/s		V_r = 5 m/s		V_r = 10 m/s	
ζ_{eq}	P_{EM} (kW)	Eff. (%)	P_{EM} (kW)	Eff. (%)	P_{EM} (kW)	Eff. (%)
5%	$1.53\text{x}10^{-7}$	54.7%	$2.85\text{x}10^{-3}$	4.3%	0.66	22.8%
10%	$5.51\text{x}10^{-8}$	39.6%	$7.44\text{x}10^{-5}$	2.2%	0.96	22.5%
15%	$7.74\text{x}10^{-9}$	16.3%	$1.82\text{x}10^{-7}$	5.6%	1.00	22.0%
20%	$6.74\text{x}10^{-9}$	14.6%	$4.25\text{x}10^{-8}$	6.1%	0.80	20.3%
25%	$6.60\text{x}10^{-9}$	18.4%	$1.26\text{x}10^{-7}$	21.1%	0.59	18.5%
30%	$6.69\text{x}10^{-9}$	25.1%	$1.77\text{x}10^{-7}$	32.3%	0.37	16.7%
35%	$5.56\text{x}10^{-9}$	20.6%	$1.70\text{x}10^{-7}$	30.9%	0.19	14.6%
40%	$5.63\text{x}10^{-9}$	23.4%	$1.22\text{x}10^{-7}$	30.2%	0.11	12.9%

Table 5.4 Cont.

	V_r = 15 m/s		V_r = 20 m/s		V_r = 25 m/s	
ζ_{eq}	P_{EM} (kW)	Eff. (%)	P_{EM} (kW)	Eff. (%)	P_{EM} (kW)	Eff. (%)
5%	13.40	55.8%	116.47	78.9%	1042.25	91.4%
10%	17.90	51.0%	134.65	74.0%	1028.19	88.1%
15%	20.20	47.9%	133.16	70.5%	884.47	85.0%
20%	20.90	45.5%	124.21	67.5%	743.12	82.0%
25%	19.90	43.2%	111.73	64.8%	620.54	79.2%
30%	17.60	41.0%	98.81	62.1%	524.56	76.6%
35%	14.60	38.9%	85.46	59.5%	445.12	74.0%
40%	11.60	36.7%	72.01	57.2%	377.66	71.5%

Similar to the along-wind forces, the EM power from the across-wind forces increased by several orders of magnitude between the lowest and highest reference wind speeds considered. For low wind speeds, the across-wind forces generated energy at negligible rates, however for high wind speeds the rate of EM energy generation was significant. For a reference wind speed of 25 m/s and low damping ratios, the EM power was about 1,000 kW. For low wind speeds, the data does not seem to show a clear pattern between equivalent damping ratio provided by the EH damper and EH efficiency. For higher winds speeds, i.e. reference wind speeds of 10 m/s and greater, there was a clear pattern; the EH efficiency increased with reference wind speed and decreased with equivalent damping ratio provided by the EH damper, similar to along-wind

forces. The equivalent damping ratio that maximized EM power varied for the wind speeds considered here, with values ranging from 5% to 20%.

Table 5.5, shown below summarizes the response of the building due to the across-wind forces. For low wind speeds the peak drift ratios and accelerations were very small but for high wind speeds these values became more significant. Based on the peak drift ratios, none of the analyses resulted in yielding of the structural members, however the peak accelerations were quite high for higher winds, which is a serviceability concern. For a reference wind speed of 25 m/s and a damping ratio of 5% provided by the EH damper, the peak acceleration was about 12% *g* which would be uncomfortable for building occupants. This level of acceleration is approaching the intolerable levels of acceleration and significantly exceeds the recommended peak acceleration proposed by Griffis (1993). Table 5.5 also shows that these EH devices were effective in reducing peak drift ratios and accelerations due to across-wind forces, except for the a reference wind speed of 25 m/s where the peak acceleration exceed that recommended by Griffis (1993) for all damping ratios considered. The next section provides a comparison of the effectiveness of the EH damper under along-wind and across-wind forces.

Table 5.5. Structure Response due to Across-Wind Forces

	V_r = 2.5 m/s		V_r = 5 m/s		V_r = 10 m/s	
ζ_{eq}	**Peak Drift Ratio**	**Peak acc. (m/s^2)**	**Peak Drift Ratio**	**Peak acc. (m/s^2)**	**Peak Drift Ratio**	**Peak acc. (m/s^2)**
5%	0.0000%	$9.40\text{x}10^{-4}$	0.0038%	$5.23\text{x}10^{-3}$	0.0305%	0.0361
10%	0.0000%	$4.97\text{x}10^{-4}$	0.0011%	$2.90\text{x}10^{-3}$	0.0286%	0.0484
15%	0.0000%	$3.25\text{x}10^{-4}$	0.0000%	$1.12\text{x}10^{-3}$	0.0258%	0.0416
20%	0.0000%	$3.14\text{x}10^{-4}$	0.0000%	$9.61\text{x}10^{-4}$	0.0234%	0.0383
25%	0.0000%	$3.03\text{x}10^{-4}$	0.0000%	$8.55\text{x}10^{-4}$	0.0208%	0.0296
30%	0.0000%	$3.24\text{x}10^{-4}$	0.0000%	$1.11\text{x}10^{-3}$	0.0175%	0.0231
35%	0.0000%	$2.83\text{x}10^{-4}$	0.0000%	$1.27\text{x}10^{-3}$	0.0143%	0.0204
40%	0.0000%	$3.65\text{x}10^{-4}$	0.0000%	$1.29\text{x}10^{-3}$	0.0110%	0.0168

Table 5.5 Cont.

	V_r = 15 m/s		V_r = 20 m/s		V_r = 25 m/s	
ζ_{eq}	**Peak Drift Ratio**	**Peak acc. (m/s^2)**	**Peak Drift Ratio**	**Peak acc. (m/s^2)**	**Peak Drift Ratio**	**Peak acc. (m/s^2)**
5%	0.109%	0.162	0.223%	0.400	0.590%	1.169
10%	0.089%	0.135	0.188%	0.320	0.404%	0.817
15%	0.080%	0.116	0.168%	0.293	0.308%	0.654
20%	0.073%	0.099	0.149%	0.262	0.249%	0.554
25%	0.066%	0.094	0.131%	0.221	0.209%	0.491
30%	0.059%	0.095	0.120%	0.188	0.181%	0.500
35%	0.053%	0.083	0.109%	0.199	0.159%	0.421
40%	0.047%	0.075	0.100%	0.186	0.143%	0.420

5.5. Comparison of EH from Along-Wind and Across-Wind Forces

Figure 5.15 and Table 5.6 compare the maximum EH power for each of the reference wind speeds considered (note the logarithmic scale for the y-axis on Figure 5.15). Table 5.6 also gives the damping ratios provided by the EH damper that produced these maximum EM powers. This data shows that for low wind speeds, (2.5 and 5 m/s) more energy is harvested under along-wind forces and for high wind speeds (20 and 25 m/s) more energy is harvested under across-wind forces. For intermediate wind speeds similar amounts of energy was harvested.

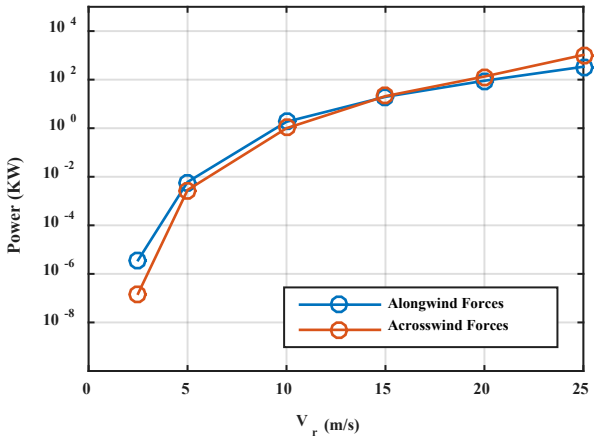

Figure 5.15 Maximum EM power generated for along-wind and across-wind forces

Table 5.6. Comparison of Energy Harvesting for Along-Wind and Across-Wind Forces

	Along-Wind Forces		Across-Wind Forces	
	Peak P_{EM} (kW)	**Optimal ζ_{eq}**	**Peak P_{EM} (kW)**	**Optimal ζ_{eq}**
V_r = 2.5 m/s	3.67×10^{-6}	5%	1.53×10^{-7}	5%
V_r = 5 m/s	6.08×10^{-3}	5%	2.85×10^{-3}	5%
V_r = 10 m/s	1.84	5%	1.00	15%
V_r = 15 m/s	19.66	5%	20.90	20%
V_r =20 m/s	90.17	5%	134.65	10%
V_r =25 m/s	339.95	10%	1042.25	5%

In Chapter 2, an equation to predict the optimal damping ratio provided by the EH damper based on the ratio of forcing frequency to natural frequency and the damping inherent in the structure was presented (Eq. (2-27)). As discussed in Chapter 4, the fluctuating wind speed spectrum contains significant contributions from a range of frequencies. This means the along wind force time history will also contain contributions from a range of frequencies and several modes of vibration may be active when the building is subject to along-wind forces. This makes it difficult to use Eq. (2-27) to predict the damping ratio that will maximize EM power without performing a modal analysis. The across-wind forces are dominated by the vortex shedding frequency, which varies over the height of the building. As a result, several modes contribute to

the achieved energy harvesting, which also makes use of Eq. (2-27) to determine the optimal damping ratio difficult. Additionally, energy is further dissipated in the EH damper due to friction amongst its mechanical parts, which is not considered in the derivation of Eq. (2-27). Despite these challenges, a preliminary estimation of the optimal viscous damping ratio using a single-mode approach was attempted. The first mode was considered, because it had a natural frequency close to the range of vortex shedding frequencies over the building height. Taking the wind speed at the top of the building as the representative wind speed, a single vortex shedding frequency, f_s, was be calculated from Eq. (4-30), and used to compute the theoretical optimum damping ratio for the across-wind forces. Using a damping ratio of 1% for the structure, Table 5.7 shows these calculations. When calculating the forcing frequency ratio, the vortex shedding frequency was converted to a circular frequency and the first natural frequency, $\omega_n = \omega_1$, was used.

Table 5.7. Theoretical Optimum Damping Ratio for Across-Wind Forces using a single mode approach

V_r (m/s)	V_H (m/s)	f_s (Hz.)	ω/ω_n	ζ^*_{EM}
2.5	7.80	0.02	0.10	508%
5	15.61	0.03	0.20	247%
10	31.21	0.06	0.39	109%
15	46.82	0.09	0.59	56%
20	62.41	0.12	0.78	25%
25	78.03	0.16	0.98	3%

When comparing Table 5.6 and Table 5.7, the theoretical optimum damping ratio predicted by Eq. (2-27) overestimated the optimum damping ratio for all reference wind speeds except for 25 m/s. In accordance with the previous discussion, this discrepancy resulted from the fact that several modes contribute to the response, as well as the friction losses not accounted for in the derivation of Eq. (2-27). Predictions are better in the case of higher velocities (e.g., $V_r = 25$

m/s), which result in higher forces, because the contribution of the frictional resistance to the total EH damper reaction force is smaller. This smaller contribution is also demonstrated by the higher efficiency achieved at higher wind speeds, as demonstrated in Table 5.2 and Table 5.4.

5.6. Seismic Analysis of Example Building Equipped with EH Dampers

Next, the example building was subjected to a suite of seismic ground motions to determine if the levels of damping provided by the EH dampers that are optimal for EH are suitable to limit damage to the structure under seismic attack. The suite of ground motions used for the seismic analysis was the FEMA P695 far field ground motions which contain 22 sets of ground motion recordings with each set consisting of the two horizontal and one vertical ground motion recording (FEMA, 2009). Only the horizontal ground motions were considered resulting in a suite of 44 ground motion time histories used for analysis.

The FEMA P695 ground motions are normalized and must be scaled to reflect the seismicity (or hazard level) of the site. In order the determine the scale factor to use for ground motions for the seismic analysis, the average response spectrum of the 44 horizontal far-field ground motions was compared to the design spectrum specified in ASCE 7-10. When determining the design spectrum, the building was assumed to be located in San Francisco, California which is approximately 14 km from the nearest active fault based on USGS fault maps. FEMA P695 defines far-field sites as being more than 10 km from the nearest fault which means this location would be considered a far-field site according to FEMA P695. Additionally, as recommended by ASCE 7-10, when detailed geotechnical information is not available, the soil conditions were assumed to be such that the site would be considered site class D. Figure 5.16 shows the average of the response spectra for the 44 FEMA P695 ground motions. Figure 5.17 shows the design spectrum for the assumed building site based on the specifications of ASCE 7-

10. ASCE 7-10 also specifies a maximum considered earthquake (MCE) which is represented by a spectrum that is 1.5 times the design earthquake spectrum.

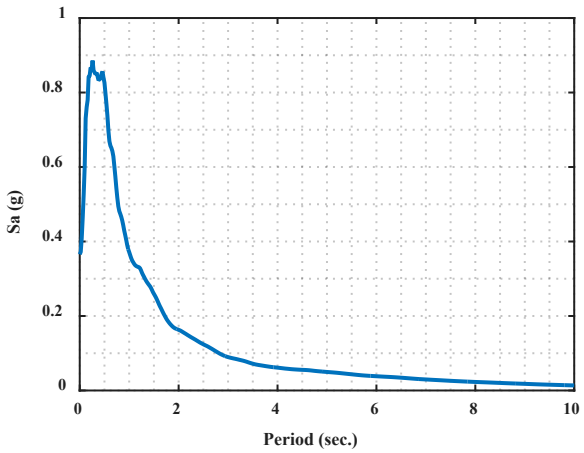

Figure 5.16 Average response spectrum of the FEMA P695 ground motions

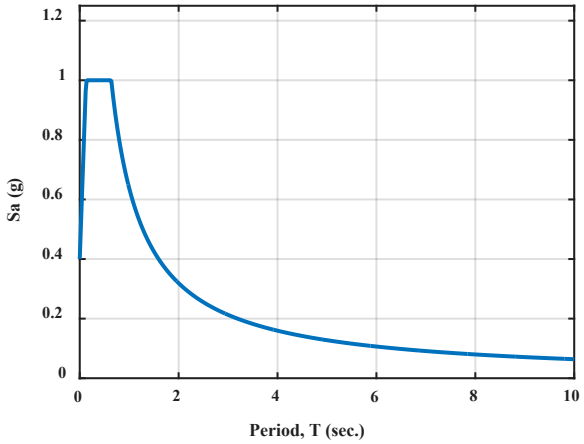

Figure 5.17 Design spectrum for San Francisco, CA and Site Class D

When using a suite of ground motions for a seismic response history analysis, ASCE 7-10 requires the ground motions to be scaled such that the average value of the 5 percent damped response spectra for the suite of motions is not less than the design response spectrum for the site for periods ranging from $0.2T$ to $1.5T$, where T is the natural period of the structure in the fundamental mode for the direction of the response being analyzed. The fundamental modal period for this example building (in both directions) is 6.26 seconds. Modes with periods this

high usually do not contribute significantly the response of the building under seismic ground motions so scaling the suite of ground motions based on the second mode, which has a period of 2.17 seconds, was also considered. Figure 5.18 and Figure 5.19 show the scaled average response spectrum from the FEMA P695 ground motions along with the design spectrum for the building site specified in ASCE 7-10; Figure 5.18 shows the scaling based on the first natural period and Figure 5.19 shows the scaling based on the second natural period. The green vertical lines represent 0.2 times and 1.5 times the natural period considered for scaling. When scaling based on the first natural period, the scale factor is equal to 4.25, while the scale factor when scaling based on the second natural period is only 2.5. When considering the MCE, the scale factors are 1.5 times the scale factors for the design earthquake, i.e. 6.375 and 3.75 when scaling based on the first and second natural periods respectively.

Figure 5.18 shows that when scaling based on the first mode, the response spectrum of the suite of ground motions for the lower periods is over estimated by about 3.5 times. As shown in Figure 5.20, the first three modes, which have modal periods of 6.26, 2.13, and 1.31 seconds, make up nearly 95% of the effective modal mass. This implies that higher modes most likely will not contribute much to the response of the structure. Additionally, the damping of the EH dampers was assumed to be stiffness proportional in the first mode. Considering the presumed minimal response of higher modes and the method for determine the damping provided by the EH dampers, the scale factor for the suite of ground motions representing the design earthquake was assumed to 4.25 since scaling based on the first mode of vibration controlled over scaling based on the second mode of vibration. The scale factor for the suite of ground motions representing the MCE was then assumed to be 6.375.

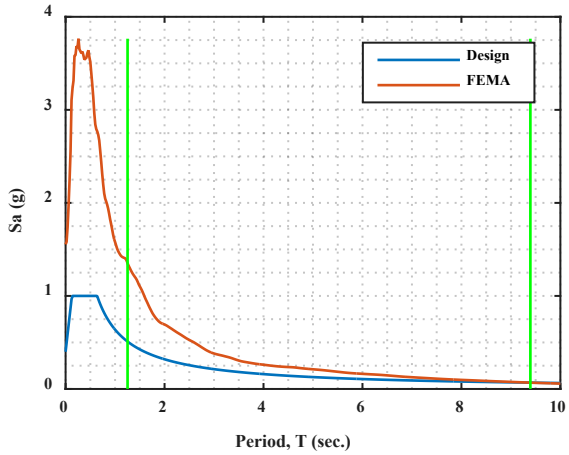

Figure 5.18 Scaling of Design Ground Motions based on T_1 = 6.26 seconds

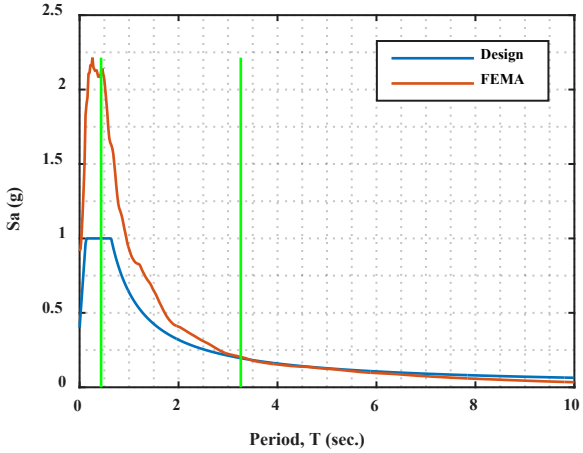

Figure 5.19 Scaling of Design Ground Motions based on T_2 = 2.17 seconds

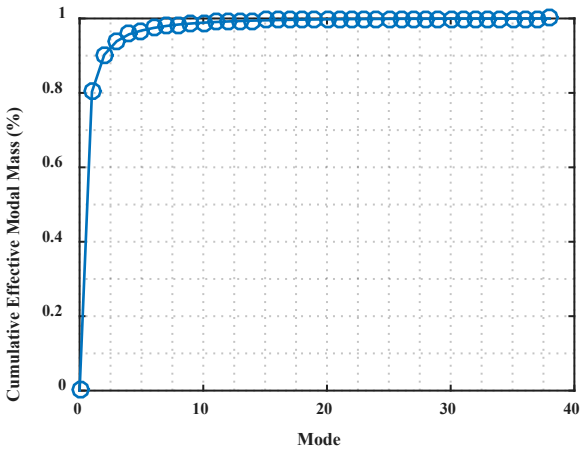

Figure 5.20 Cumulative effective modal mass for example building

When applying the earthquake ground motions to the example building, the damping ratio provided by the EH dampers was assumed based on the optimum EM power generated during the wind loading analyses. From Table 5.6, it can be seen that the optimum damping ratio varied based on the reference wind speed and whether the building was subject to along-wind or across-wind forces. For wind speeds of 2.5 and 5 m/s, the rate of energy harvesting was negligible and not considered when choosing the optimum damping ratio. For the along-wind forces, a damping ratio of 5% resulted in the highest EM power for all wind speeds except for the 25 m/s, for which 10% resulted in the highest EM power. For the across-wind forces, the optimum damping ratio ranged from 5% to 20%. In order to select a single EM damping ratio that represents the damping ratio that maximizes EM power, the EM power generated for the along-wind and across-wind forces were summed for each wind speed and damping ratio considered as shown below in Table 5.8. As noted above, reference wind speeds of 2.5 and 5 m/s were not considered. A damping ratio of 10% resulted in the highest EM power generated for all four wind speeds considered in Table 5.8 except for 10 m/s for which there was only a slight decrease in total EM power from the optimum damping ratio to a damping ratio of 10%. Considering the results of Table 5.8, an EM damping ratio of 10% was chosen for the seismic analysis of the example building.

Table 5.8. Total P_{EM} from Along-Wind and Across-Wind Force Analyses

	P_{EM} Total (kW)			
ζ_{eq}	V_r = 10 m/s	V_r = 15 m/s	V_r = 20 m/s	V_r = 25 m/s
5%	2.50	33.1	207	1355
10%	2.37	33.4	213	1368
15%	2.09	32.5	202	1213
20%	1.68	31.2	188	1048
25%	1.31	28.9	170	906
30%	0.96	25.7	152	789
35%	0.68	22.2	133	688
40%	0.52	18.7	115	600

When analyzing the seismic response of the building, the peak inter-story drift ratios were used to assess the effectiveness of the EH dampers in mitigating the effects of the ground motions. For each of the 44 ground motions considered, the peak inter-story drift at each degree of freedom was used to determine potential damage to the building for each ground motion. Once all of the ground motions were applied to the building, the average of the peak inter-story drifts for 44 ground motions was taken at each degree of freedom to determine the average response of the building. This process was carried out for both the design earthquake and the MCE. As for the analysis for the wind loading, yielding was assumed to occur at each degree of freedom at an inter-story drift ratio of 1%. Figure 5.21 and Figure 5.22 show the average of the peak drift ratios for each degree of freedom for the design earthquake and MCE respectively. In these figures, the vertical blue line represents the yield inter-story drift ratio. The jumps in the average inter-story drift ratios in these figures between degrees of freedom 9 and 10, 19 and 20, and 29 and 30 are a result of the change in inter-story stiffness at these degrees of freedom (see Table 5.1).

From Figure 5.21, it can be seen that a damping ratio of 10% was capable of limiting the peak inter-story drifts to below the yielding limit for the design earthquake, implying that the

building structure elements would not be damaged. However, for the MCE, the peak inter-story drifts for degrees of freedom 1-14 did exceed the yield limit which means there would be damage to the building as a result of the MCE.

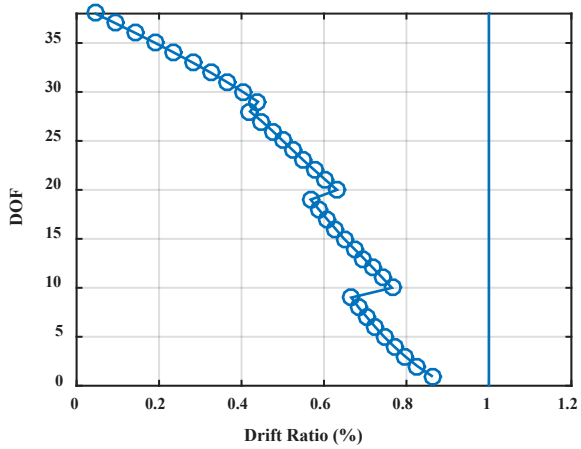

Figure 5.21 Average peak drift ratios for the suite of ground motions scaled to the design

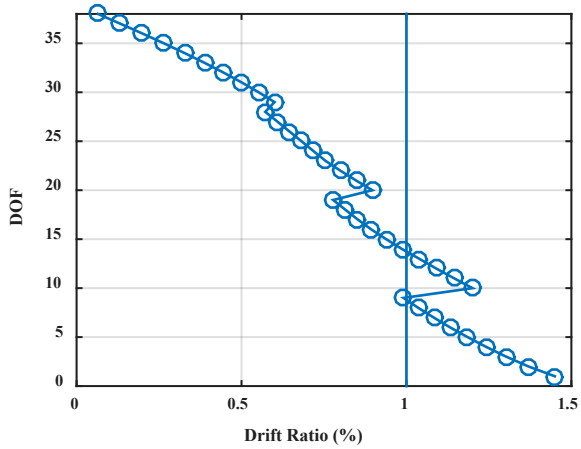

Figure 5.22 Average peak drift ratios for the suite of ground motions scaled to the MCE

5.7. Summary and Conclusions

The goal of this chapter was to assess the EH potential of tall buildings subject to wind loading and determine if the damping ratios that are best for EH are also compatible with the goals of VM. The results of this analysis showed that for low wind speeds, there is very little potential energy to be harvested. On the other hand, for high wind speeds there is a significant

amount of energy that can be harvested with reference wind speeds of 20 and 25 m/s generating energy at rates of over 100 kW. However, as the reference wind speed increases, the probability of occurrence and persistence times decreases, with wind events of mean wind speeds equal to 20 m/s or 25 m/s most likely occurring no more than a few times a year. Furthermore, for these high winds, the building accelerations exceed serviceability limits.

In addition to strong winds, two levels of seismic ground motions were considered to determine if the EH dampers are an effective means of VM: the design earthquake (DE) and the maximum considered earthquake (MCE). The damping ratios considered for the seismic analysis were those that were optimal for EH. When the building was subject to the DE, the building remained in the elastic range and there was no damage. However, under the MCE, there was yielding and building damage which shows that the levels of damping that are best for EH are not capable of preventing damage to the building under the MCE. This analysis illustrates the conflicting goals of EH and VM as well as the challenges for future research efforts on the topic of large scale EH from civil structures.

6. CONCLUSIONS AND FUTURE RESEARCH DIRECTION

6.1. Major Findings

This study investigated the feasibility of large scale energy harvesting in civil structures with the use of energy harvesting dampers. Chapter 1 presented the motivation and briefly discussed the goals of the study. Chapter 2 investigated the energy harvesting of a single degree of freedom system and showed the competing goals of EH and VM, i.e. the damping levels that are optimal for EH are not always sufficient to limit building displacements associated with extreme loading events, such as earthquakes and strong winds, which can result in structural damage and occupant discomfort. Chapter 3 presented the model of the EH damper used in the numerical analyses, and Chapter 4 discussed the estimation of the wind forces acting on the example building which were the source of energy in this study. The analysis of using a supplemental damping system to harvest the energy of wind induced vibrations of buildings and limit building displacements during extreme events was discussed in Chapter 5.

According to Energy Star, the median annual energy consumption for office buildings in the United States is equal to 184 kBtu/ft^2, which is approximately 580 kWh/m^2 (Energy Star, 2016). The example building considered here has a total floor area of 134,064 m^2 which means that, if it consumed energy at a rate typical of buildings in the United States, it would consume about 7.78x10^7 kWh per year. Averaged over an entire year, this building would consume energy at a rate of approximately 8,878 kW. For the peak reference wind speed of 25 m/s, considered in Chapter 5, the total rate of energy harvesting from the along- and across-wind forces was 1,382 kW, which would provide about 16% of the energy for this building. However, this wind speed of 25 m/s is less frequent and may have low persistence times. Furthermore, the building

accelerations associated with these energy harvesting levels exceeded limits specified for occupant comfort. From a structural design perspective, this means that the structure would need to be re-designed to incorporate additional damping or stiffness to meet serviceability requirements.

Table 6.1 shows the annual mean wind speed for several large cities in the United States. This data was obtained from the National Oceanic and Atmospheric Administration (NOAA) and are averages from 1984 through 2015. This table shows that the annual mean wind speed varies from city to city but is generally about 5 m/s or less. The total EM power for the along and across-wind forces for a reference wind speed of 5 m/s was only 0.00893 kW, which is a very small amount of power when compared to the required electrical power for a building of the size considered for this study. However, for less frequent wind speeds, such as 25 m/s, the total EM power was significantly higher (1382 kW). Thus, a detailed probabilistic life cycle analysis, accounting for wind speeds and persistence over the lifetime of structures located at various sites, is required to quantify the EH potential of buildings equipped with EH dampers. The need for a probabilistic life cycle analysis is further extenuated by the fact that the relation between mean reference wind speed, V_r, and EM power, P_{EM}, is not linear. For example, when the reference mean wind speed doubled from 5 m/s to 10 m/s, the peak EM power increased by factors of 302 and 350 for along and across-wind forces, respectively. Similarly, when the reference mean wind speed doubled from 10 m/s to 20 m/s, the peak EM power increased by factors of 49 and 134 for along and across-wind forces, respectively.

Table 6.1. Annual Mean Wind Speed for US Cities (NOAA, 2015)

City	Annual Mean Wind Speed (m/s)
Atlanta, GA	3.71
Boston, MA	5.14
Chicago, IL	4.43
Columbus, OH	3.40
Dallas, TX	4.25
Denver, CO	3.58
Houston TX,	3.35
Las Vegas, NV	3.89
Los Angeles, CA	2.50
Miami, FL	3.76
Minneapolis, MN	4.34
New York, NY	4.38
Philadelphia, PA	4.16
Phoenix, AZ	2.73
San Diego, CA	2.86
San Francisco, CA	4.70
Seattle, WA	3.53
Washington, DC	4.02

6.2. Future Research

Future research on this topic may address the following:

- Investigate the energy harvesting capabilities of suites of buildings of various aspect ratios, $H/\sqrt{BD}$, and side ratios, D/B, where H is the height of the building, B is the width of the building perpendicular to the direction of the wind, and D is width of the building in direction of the wind. This would determine which buildings sizes and shapes are suitable to for large scale energy harvesting. More complex buildings, i.e. those with curved edges, should also be analyzed since the interaction between the wind and these buildings results in a different dynamic response than rectangular buildings.
- Site specific analyses would also be of benefit when assessing the merit of this technology. Wind speeds vary from site to site in terms of mean annual frequency and persistence times.

Quantification of those parameters will allow an accurate assessment of the energy harvesting potential of buildings over their lifetime. This information will allow a life-cycle cost-benefit analysis of this concept and will determine its economic feasibility.

- The effect of surrounding structures and obstructions on the harvested energy by a given building should be investigated. Surrounding structures influence the turbulence of the air flow affecting the wind speed and force fluctuations acting on the building of interest as well as the mean wind speed profile.
- More detailed analysis of the EH damper is also required. This includes experimental investigations on different size EH dampers in order to more accurately estimate how the model parameters vary as the size of the EH damper increases. It may also be beneficial to investigate if different EM dampers would provide better EH capabilities than the one used in this study such as linear moving magnet EM dampers (Palomera-Arias, 2005; Zhu et al., 2011).
- Methods of increasing the energy harvesting potential of given building can also be investigated. One such method can be the use of geometric magnification schemes as described in Chapter 1 and shown in Figure 1.6 and Figure 1.7. Geometric magnification could be used to either increase the energy harvesting of the building or enable the use of smaller EH dampers for the same level of EH, which would decrease the manufacturing and installation costs. Making the building more flexible would also allow for more energy to be harvested, however, this may not be a practical alternative due to serviceability concerns as discussed previously. However, instead of a building, the energy harvesting potential of structures where serviceability requirements are not a concern could be investigated. For

example, tall lattice towers, such as those used as transmission or radio towers, which may have larger natural periods than buildings, could be investigated.

Although this investigation predicted low amounts of harvested energy for low wind conditions, the EH potential under moderate and strong winds was found to be significant, warranting future research on the topic. Innovative sources of energy will be required to meet the global energy needs of the future if we are to continue to reduce our dependence on fossil fuels. This research investigated an existing technology in structural engineering, supplemental damping, and attempted to expand on it by investigating damping systems that could also be used as EH systems. If this technology can be proven to be economically viable, it can be used by structural engineers to create "smart" structural systems that generate their own electricity while providing safety for their occupants.

REFERENCES

American Society of Civil Engineers. (2010). *Minimum Design Loads for Buildings and Other Structures.* Reston, VA: ASCE 7-10.

Architectural Institute of Japan. (2004). *Recommendations for Loads on Buildings.* Tokyo, Japan: Architectural Institute of Japan.

Australia/New Zealand Standards. (2011). *Structural Design Actions: Part 2 - Wind Actions.* Sydney, NSW, Australia: AS/NZS 1170.2:2011.

Baldwin, J., Roswurm, S., Nolan, J., & Holliday, L. (2011). *Energy Harvesting on Highway Bridges.* Oklahoma City: Federal Highway Administration/Oklahoma Department of Transportation.

Black, C. J., Makris, N., & Aiken, I. D. (2004). Component Testing, Seismic Evaluation and Characterization of Buckling-Restrained Braces. *Journal of Structural Engineering*, 880-894.

Boggs, D., & Dragovich, J. (2006). The Nature of Wind Loads and Dynamic Response. *Special Publication*, 15-44.

Cassidy, I. L., Scruggs, J. T., Behrens, S., & Gavin, H. P. (2011). Design and experimental characterization of an electromagnetic transducer for larger-scale vibratory energy harvesting applications. *Journal of Intelligent Material Systems and Structures*, 2009-2024.

Chopra, A. K. (2013). *Dynamics of Structures: Theory and Applications to Earthquake Engineering.* New York: Pearson Education.

Christopoulos, C., & Filiatrault, A. (2006). *Principles of Passive Supplemental Damping and Seismic Isolation.* Pavia, Italy: IUSS Press.

Ciampi, V., De Angelis, M., & Paolacci, F. (1995). Design of yielding or friction-based dissipative bracings for seismic protection of buildings. *Engineering Structures, 17*(5), 381-391.

Constantinou, M. C., Tsopelas, P., Hammel, W., & Sigaher, A. N. (2001). Toggle-Brace-Damper Seismic Energy Dissipation Systems. *Journal of Structural Engineering*, 105-112.

Constantinou, M., & Symans, M. (1992). *Experimental and Analytical Investigation of Sesmic Response of Structures with Supplemental Fluid Viscous Dampers.* National Center for Earthquake Engineering Research.

East Japan Railway Company. (2008). *Demonstartion Experiment of the Power Generating Floor at Tokyo Station.* Retrieved from http://eastjapanrail.com/

Energy Star. (2016, 11 18). *Data Trends: Energy Use in Office Buildings.* Retrieved from Energy Star: https://www.energystar.gov/buildings/tools-and-resources/datatrends-energy-use-office-buildings

FEMA. (2009). *Quantification of Building Seismic Performance Factors.* Washington, DC: FEMA P695, Prepared by Applied Technology Council for the Federal Emergency Management Agency.

Filiatrault, A., & Cherry, S. (1987). Performance Evaluation of Friction Damped Braced Steel Frames Under Simulated Earthquake Loads. *Earthquake Spectra, 3*(1), 57-78.

Griffis, L. G. (1993). Serviceability Limit States Under Wind Load. *Engineering Journal/American Institute of Steel Construction*, 1-16.

Holmes, J. D. (2015). *Wind Loading of Structures* (3rd ed.). Boca Raton: CRC Press, Taylor & Francis Group, LLC.

Hrovat, D., Barak, P., & Rabins, M. (1983). Semi-Active versus Passive or Active Tuned Mass Dampers for Structural Control. *Journal of Engineering Mechanics, 109*(3), 691-705.

Kaltschmitt, M., Streicher, W., & Wiese, A. (2007). *Renewable Energy: Technology, Economics and Environment.* Berlin: Springer.

Kawamoto, Y., Suda, Y., Inoue, H., & Kondo, T. (2008). Electro-mechanical suspension system considering energy consumption and vehicle manoeuvre. *Vehicle System Dynamics, 46*, 1053-1063.

Kwon, D., & Kareem, A. (2006). *NatHaz on-line wind simulator (NOWS): simulation of Guassian multivariate wind fields.* Univ. of Notre Dame. NatHaz Modeling Laboratory Report. Retrieved from http://windsim.ce.nd.edu/

Liang, S., Liu, S., Li, Q., Zhang, L., & Gu, M. (2002). Mathematical model of acrosswind dynamic loads on rectangular tall buildings. *Journal of Wind Engineering and Industrial Aerodynamics*, 1757-1770.

Mazza, F., & Vulcano, A. (2010). Control of the earthquake and wind dynamic response of steel-framed buidlings by using additional braces and/or viscoelastic dampers. *Earthquake Engineering and Structural Dynamics, 40*, 155-174.

McNamara, R. J., & Taylor, D. P. (2003). Fluid Viscous Dampers for High-Rise Buildings. *Structral Desgin of Tall and Special Buildings, 12*, 145-154.

Ni, T., Zuo, L., & Kareem, A. (2011). Assessment of Energy Potential and Vibration Mitigation of Regenerative Tune Mass Dampers on Wind Excited Tall Buildings. *2011 International Design Engineering Technical Conferences & Computers and Information in Engineering Conference* (pp. 1-10). Washington, DC: ASME.

NOAA. (2015). *Comparative Climatic Data.* Retrieved from National Oceanic and Atmospheric Administration: https://www.ncdc.noaa.gov/ghcn/comparative-climatic-data

Palomera-Arias, R. (2005). *Passive Electromagnetic Damping Device for Motion Control of Building Structures.* Cambridge, MA: Massachusetts Insititute of Technology.

Peigney, M., & Siegert, D. (2013). Piezoelectric energy harvesting from traffic-induced bridge vibrations. *Smart Materials and Structures, 22*, 095019.

Sabelli, R., & Lopez, W. (2004). Design of Buckling-Restrained Braced Frames. *Modern Steel Construction*.

Shinozuka, M., & Deodatis, G. (1991). Simulation of stocashtic processes by spectral representation. *Appl Mech Rev, 44*(4), 191-204.

Sigaher, A. N., & Constantinou, M. C. (2003). Scissor-Jack-Damper Energy Dissipation System. *Earthquake Spectra, 19*(1), 133-158.

Simiu, E. (2011). *Design of Buildings for Wind: A Guide for ASCE 7-10 Standard Users and Designers of Special Structures* (2nd ed.). Hoboken: John Wiley & Sons, Inc.

Simiu, E., & Scanlan, R. H. (1996). *Wind Effects on Structures: Fundamentals and Applications to Design* (3rd ed.). New York: John Wiley & Sons, Inc.

Sladek, J. R., & Klingner, R. E. (1983). Effect of Tuned-Mass Dampers on Seismic Response. *Journal of Structural Engineering, 109*(8), 2004-2009.

USGS. (2017). *Interactive Fault Map*. Retrieved March 2017, from https://earthquake.usgs.gov/hazards/qfaults/map/#qfaults

USGS. (2017). *U.S. Seismic Design Maps*. Retrieved March 2017, from https://earthquake.usgs.gov/designmaps/us/application.php?

Zhang, R.-H., & Soong, T. (1992). Seismic Design of Viscoelastic Dampers for Structural Applications. *Journal of Structural Engineering, 118*(5), 1375-1392.

Zhu, S., Shen, W.-a., & Xu, Y.-l. (2012). Linear electromagnetic devices for vibration dampong and energy harvesting: Modeling and testing. *Engineerign Structures, 34*, 198-212.

Zuo, L., & Tang, X. (2013). Large-scale vibration energy harvesting. *Journal of Intelligent Material Systems and Structures, 24*(11), 1405-1430.